Multijet Cross Section Ratios in $p\bar{p}$ Collisions at $\sqrt{s} = 1.8$ TeV

by

Ki Suk Hahn

Submitted in Partial Fulfillment
of the
Requirements for the Degree
Doctor of Philosophy

Supervised by
Professor Frederick Lobkowicz
and
Professor Gerald Blazey
Department of Physics and Astronomy
The College
Arts and Sciences

University of Rochester
Rochester, New York
1998

To my parents.

Curriculum Vitae

The author was born in Manila, Philippines on January 19, 1968. He attended the California State Polytechnic University in Pomona from 1986 to 1988 and the University of California, Los Angeles from 1988 to 1990, and graduated with a Bachelor of Science degree in 1990. He came to the University of Rochester in the Fall of 1991 for graduate studies in Physics. He received the Master of Arts degree in 1993 and pursued his research in Particle Physics under the direction of the late Professor Frederick Lobkowicz and Professor Gerald Blazey.

Acknowledgments

I would like to thank the Rochester D0 group for their friendship and help: Kathy Fatyga, Eunil Won, Dylan Casey, Bob Hirosky, Stefan Grünendahl, Hui Zhu, Cathy Cretsinger, Marc Paterno, Jae Yu, and professors Tom Ferbel and the late Fred Lobkowicz.

For the analysis I thank Elizabeth Gallas and Jerry Blazey for their guidance, and Soon Yung Jun for his friendship and help. I also thank David Summers, Dieter Zeppenfeld, and Walter Giele for their comments and for patiently answering questions about JETRAD.

I thank my uncles and aunts in NYC for their hospitality while I took much-wanted breaks from schoolwork.

Additional thanks go to the staffs at Fermilab and collaborating institutions for their contributions to this work, and acknowledge support from the Department of Energy and National Science Foundation (U.S.A.), Commissariat à L'Energie Atomique (France), State Committee for Science and Technology and Ministry for Atomic Energy (Russia), CAPES and CNPq (Brazil), Departments of Atomic Energy and Science and Education (India), Colciencias (Colombia), CONACyT (Mexico), Ministry of Education and KOSEF (Korea), and CONICET and UBACyT (Argentina).

Abstract

We have measured the ratio of the three-jet to two-jet inclusive cross section as a function of the total transverse energy of jets ($H_T = \sum E_T^j$) in events in $p\overline{p}$ collisions at $\sqrt{s} = 1.8$ TeV. We find that for $\sum E_T > 200$ GeV there is a 70% probability of emitting an additional jet with $E_T > 20$ GeV. Using this measurement and the framework of the theory of Quantum Chromodynamics (QCD), we investigated the size of the renormalization scale used to model emission of "soft" (low-E_T) jets in multijet final states. The findings indicate that, to order α_S^3 in QCD the data favor a scale representative of the hard scattering rather than a softer scale of the order of the third jet's transverse momentum. The preferred scale is $\mu_R \approx \frac{1}{4} H_T$.

Contents

List of Tables

List of Figures

Foreword

The DØ collaboration consists of more than 400 physicists and students from 48 institutions from around the world. The University of Rochester has been active in the following areas of DØ: calorimeter design and calibration, data acquisition and detector-monitoring shifts during collider runs, liquid argon purity monitoring, offline data reconstruction, data analysis in the Top, QCD, W/Z, and New Phenomena physics groups, and scintillating-fiber-detector design and development for the detector upgrade, including characterization measurements of visible light photon counters.

I participated in the detector monitoring shifts, the calibration of the Level 1 calorimeter trigger, and the offline data reconstruction effort. For the latter I wrote and adapted scripts to process the data files and monitored the data flow through the reconstruction system. I also acted as an administrative liaison between the QCD physics group (end-users) and the Offline Computing Production Board (OCPB). My analysis project has been the study of cross-section ratios of multijet events.

Chapter 1

Introduction

When protons and antiprotons are made to collide head-on at high energies one sees sprays of hadrons (pions, protons, neutrons, etc.) emerging from the interaction point and clustering together in groups. These clusters are called *jets.* These jets frequently emerge perpendicular to the path of the colliding proton and antiproton, and the explanation of this behavior comes in the form of the quark model, where the proton (and antiproton) is postulated to be composed of point-like charged objects called quarks. Quantum Chromodynamics (QCD) is the theory of the interaction of quarks and gluons, the latter being the field particle exchanged in an interaction between quarks. The above interaction can then be described, for example, in terms of the annihilation of a quark in the proton and an antiquark in the antiproton into a gluon, which then "decays" to a quark-antiquark pair. The two outgoing quarks travel a short distance ($\lesssim 1$ fm) before undergoing a *hadronization* process, whereby the quarks combine with other quarks to form hadrons.

Sometimes, an outgoing (or incoming) quark (Figure 1.1) radiates a gluon at a large angle (with respect to the quark's direction) and this gluon also hadronizes to become a separate jet. This would yield a three-jet event.

It is possible to calculate the probability or *cross section* to produce two-jet final

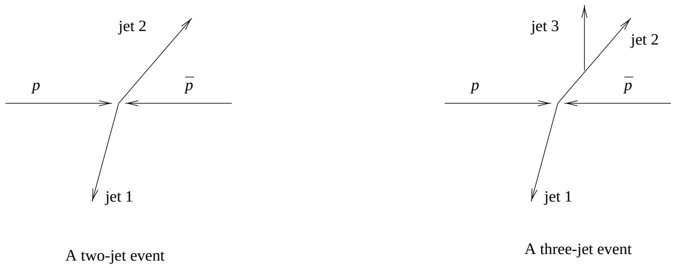

Figure 1.1: Two-jet and three-jet events.

states and three-jet final states using QCD and perturbation theory. The goal of our study is to measure the ratio of the inclusive-three-jet cross section to the inclusive-two-jet cross section

$$\frac{\sigma_{3+}}{\sigma_{2+}} = \frac{\sigma(\ p\overline{p}\ \rightarrow n \text{ jets} + X\ ;\ n \geq 3)}{\sigma(\ p\overline{p}\ \rightarrow m \text{ jets} + X\ ;\ m \geq 2)}$$

as a function of the total transverse energy* of all jets in an event. (X denotes other products of collision which we ignore.) We use the symbol H_T to denote the sum of the jet E_T s:

$$H_T = \sum_{\text{jets}} E_T$$

We compare the value of $\frac{\sigma_{3+}}{\sigma_{2+}}$ as a function of H_T for data and predictions from perturbative calculations up to order α_s^3 (Next-to-leading order).

One application of this study is in the design of a trigger for weak boson scattering at the Large Hadron Collider to search for the Higgs particle. The second motivation of this analysis is to determine a preferred renormalization scale for the measurement of the ratio of cross sections.

---

*Transverse energy, E_T, is defined as $E \sin\theta$ where θ is the angle between the jet's axis and the beamline.

1.1 Organization of thesis

I first outline the theory of Quantum Chromodynamics in Chapter 2. In Chapter 3 I describe the Tevatron accelerator and the DØ detector, and in Chapter 4 I describe data acquisition and event reconstruction. Chapters 5 and 6 comprise the analysis of the data, including the uncertainties in the measurement. In Chapter 7 I introduce the theoretical predictions from Monte Carlo calculations and describe the quantitative comparisons with data. In the last chapter I summarize the comparisons between data and theory.

Chapter 2

QCD

2.1 Introduction

In this chapter, I outline the nature of the strong interactions as formulated in the Standard Model. I then discuss the application of Quantum Chromodynamics to hadron-hadron collisions and jet production. Lastly, I describe the test of the renormalization scale to be performed in later chapters.

2.2 Beginnings of QCD

The theory of strong interactions started with the need to explain why protons in a nucleus did not repel each other and thereby make the nucleus fall apart. A force called the *strong force* was postulated to keep the protons together despite their electrical repulsion. The first field theory of strong interactions was due to Yukawa in 1934, in which the attractive force between protons at short distances was attributed to the exchange of a pion, discovered subsequently in 1947 [1].

Over the following two decades experiments at accelerators found many new particles. The classification of these particles came in 1961 with the Eightfold Way (Gell-Mann and Ne'eman). Further simplification came with the quark model of Gell-Mann and Zweig, in 1964. The quark model holds that all baryons (*e.g.,* proton) and mesons (*e.g.,* pion) are made up of quarks [2].

Other high-energy experiments were performed (1970s) with electron beams on proton targets, so-called *deep inelastic scattering* (DIS) experiments. These indicated that the proton had a sub-structure when probed with an electron, the way atoms were long ago found to have a nuclear sub-structure when probed with alpha particles. The name given to the constituents of protons was *partons.* The quarks of hadron spectroscopy were candidates for the partons found in DIS experiments. It appears that these constituents cannot exist as free particles, but are confined within hadrons. This phenomena is called *confinement.* Furthermore, high energy lepton-hadron scattering experiments showed that the interaction with partons is well-described by a model where the act as non-interacting point-like objects within hadrons (the parton model.) More data revealed that much of the nucleon mass had to be attributed to the presence of neutral partons (later called *gluons*). The drop in the strength of the interaction among partons with decreasing distance is called *asymptotic freedom*, and arises as a natural consequence of QCD. QCD in its current form was proposed around 1974 [3].

2.3 The Standard Model

The Standard Model is the currently accepted theory of the interactions between matter at the elementary particle level. It encompasses electricity, magnetism, strong, and weak interactions. It does not include gravity as yet. The Standard Model is based on the gauge group $SU(3)_{color} \times SU(2) \times U(1)_Y$, representing, respectively, strong interactions or QCD, Weak Interactions, and Quantum Electromagnetism (QED).

The elementary particles that interact according to the Standard Model are *quarks* and *leptons.* The mediators of the forces are the *gauge bosons*: photons (γ), W, Z, and gluons (g). Composite particles are made up of either a quark-antiquark pair (*mesons*) or a bound state of three quarks (or three antiquarks) called *baryons* (Table 2.1)

Table 2.1: Classification of matter. The composite particles are at the bottom of the table.

<table>
<tr><td colspan="4">Matter</td></tr>
<tr><td colspan="2">Fermions</td><td colspan="2">Bosons</td></tr>
<tr><td>Leptons</td><td>Quarks</td><td colspan="2">Mediators</td></tr>
<tr><td rowspan="4">ν_e ν_μ ν_τ
e μ τ</td><td>u c t
d s b</td><td colspan="2">γ W Z g</td></tr>
<tr><td colspan="2">Hadrons</td><td rowspan="3"></td></tr>
<tr><td>Baryons</td><td>Mesons</td></tr>
<tr><td>n p</td><td>π ρ</td></tr>
</table>

The first sector of the Standard Model that was fully developed is electromagnetism, or Quantum Electrodynamics. It describes the interaction of electrically charged particles via the exchange of photons. QED is based on the quantization of Maxwell's Equations, and describes processes such as the Coulomb interaction, pair-production, pair annihilation, and Compton scattering ($e^- + \gamma \rightarrow e^- + \gamma$).

All quarks and leptons participate in weak interactions, mediated by the charged W boson or the neutral Z boson. An example of a charged interaction is muon decay ($\mu^- \rightarrow e^- + \nu_\mu + \overline{\nu}_e$). Weak interactions also govern the process of neutron beta decay ($n \rightarrow p + e^- + \overline{\nu}_e$). The electromagnetic and weak interactions are now unified, and form the electroweak theory, in which the electromagnetic and weak interactions are simply different manifestations of a single *electroweak* interaction.

The gauge boson of the electromagnetic interaction, the photon, is massless, while the weak interaction bosons, the W^+, W^-, and the Z boson, are massive. (The QCD gauge boson, the gluon, is also massless.) One explanation for this unsymmetrical state is provided by the *Higgs mechanism* [4]. The Higgs mechanism is responsible for the masses of the $W^\pm$ and the Z^0, as well as the masses of the quarks and leptons. A Higgs particle (or two) is required for most formulations of the model, and has been the object of searches in modern particle colliders [4].

2.4 QCD

QCD describes the strong interactions between quarks as mediated by gluons. It is a gauge field theory based on the group $SU(3)$. $SU(3)$ or $SU(3)_{color}$ is the group of unitary transformations on color quark fields. Requiring local invariance under color transformations results in a law of conservation of "color charge," and also the presence of a field (gluon field in this case) and its associated quantum particles (gluons). Quarks carry color as well as electric charge. The three kinds of color "charge" are usually termed Red, Green, and Blue. Antiquarks carry "anticolor." Color is exchanged between quarks via eight gluons. The six known quarks are listed in Table 2.2 [5].

Table 2.2: List of Quarks.

Name	Symbol	Charge $[e]$	Mass
Down	d	$-\frac{1}{3}$	2-8 MeV$/c^2$
Up	u	$+\frac{2}{3}$	5-15 MeV$/c^2$
Strange	s	$-\frac{1}{3}$	100-300 MeV$/c^2$
Charm	c	$+\frac{2}{3}$	1.0-1.6 GeV$/c^2$
Bottom	b	$-\frac{1}{3}$	4.1-4.5 GeV$/c^2$
Top	t	$+\frac{2}{3}$	172.1$\pm$5.2 GeV$/c^2$

Mesons are formed from a combination of two "valence" quarks, $(q\overline{q})$ while baryons are formed from three valence quarks $(q_1q_2q_3)$. In each case, the colors combine to form a "colorless" object. Another way of saying this is that all free and isolated particles are color singlets. The binding of nuclei in atoms is ascribed to the nucleon-nucleon attraction that is due to the long-range interaction of bound quarks in one nucleon with bound quarks in the other.

The strength of the color force depends on the distance scale of the scattering process. At short distances and short time scales (high-energies), the QCD force is weak, which provides the basis for applying perturbation theory. However, at longer time scales and large distances (low energies), the strong force is indeed strong, where it accounts for the binding of quarks within hadrons [6]. An indication of this behavior comes from the form of the strong coupling (α_S) in the leading log approximation [3]:

$$\alpha_S(Q^2) = \frac{12\pi}{(33 - 2n_f)\ln(Q^2/\Lambda_{\mathrm{QCD}}{}^2)} \qquad \text{(lowest order)}$$

with n_f the number of quark flavors (types) appropriate for the process. The parameter Λ_{QCD} is not predicted by QCD, but can be obtained from experiment. We can think of Λ_{QCD} as the natural scale of QCD. Q^2 is the square of the momentum transfer in the interaction. When Q^2 is much larger than Λ_{QCD}, the effective coupling of quarks to gluons is small, and the approximation in which quarks are non-interacting is appropriate. For Q^2 of order Λ_{QCD}, quarks and gluons form strongly-bound states of hadrons, and this corresponds to the non-perturbative regime of QCD [7].

2.5 Perturbative QCD

Factorization theorem

A basis of perturbative QCD is the *factorization* theorem. Factorization refers to the separation of the long-distance (low momentum transfer) and short-distance (high momentum transfer) parts of the interaction. The factorization theorem can be expressed via the schematic of a quark-quark interaction in $p\overline{p}$ collisions in Figure 2.1 and the equation

$$\sigma = \sum_{\text{partons } ij} \int dx_1 dx_2\, f_{h\to i}(x_1,\mu_F^2) f_{h\to j}(x_2,\mu_F^2)\hat{\sigma}_{ij}\left(\alpha_S, Q^2/\mu_F^2\right)$$

$\hat{\sigma}$ is the partonic (qq,qg,gg) point cross section. The $f_{h\to i}$ are parton distribution functions (PDF) that characterize the momentum fractions x_i of the hadron h carried by the parton i. The μ_F is the factorization scale, which can be thought of as the point where one defines a separation between the short-distance and long-distance regimes. Parton distribution functions are defined for $0 < x < 1$, and give the probability of finding some

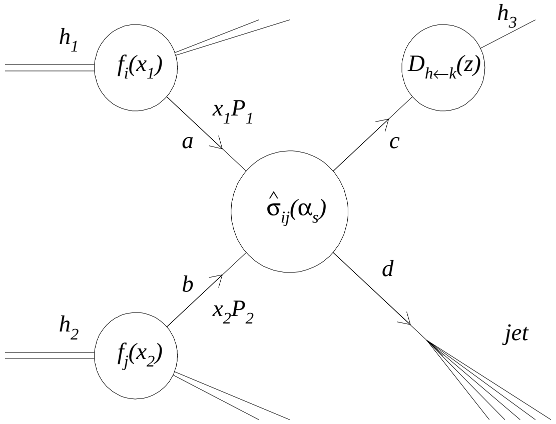

Figure 2.1: QCD description of a hard scattering process between hadrons h_1 and h_2 with four-momenta P_1 and P_2. The partons from h_1 and h_2 have momentum fraction x_1 and x_2 respectively. Partons a and b scatter to partons c and d. Parton c hadronizes to form hadron h_3 while parton d produces a jet.

parton a inside hadron h with a momentum fraction x. The parametrizations of f for different partons a and hadrons h are taken from collider and fixed-target experimental data [8]. As shown in Figure 2.1, partons of momentum fraction x_1 and x_2 undergo a point scatter into final state partons.

There are currently three main groups who perform "global fits" to experimental data to extract PDF's. These are:

- Martin, Roberts, and Stirling (MRS) [9]
- Gluck, Reya, and Vogt (GRV) [10]
- The CTEQ collaboration [11]

Parton distribution functions that are measured at some given interaction scale Q_0 can be used to determine the values at another scale Q via the Dokshitzer-Gribov-Lipatov-Altarelli-Parisi (DGLAP) evolution equations [12]. These are sets of coupled integral-differential equations that describe the Q^2-dependence of quark and gluon distribution functions [13].

$$\frac{d}{d\log Q^2} f_{h\to i}(x,Q^2) = \frac{\alpha_S}{2\pi}\int_x^1 \frac{dy}{y} f_{h\to i}(y,Q^2) P_{qq}\left(\frac{x}{y}\right)$$

This equation is for quarks only. Similar equations exist for $g \to q$, $q \to g$, and $g \to g$. The *splitting function* $P_{qq}(\frac{x}{y})$ is the probability of a quark to emit a gluon, and thereby becoming a quark with momentum reduced to x/y of its original value [14].

Hard scattering matrix elements

The partonic cross section $\hat{\sigma}$ is calculated using the Feynman rules for QCD. For two-to-two parton scattering in hadron-hadron collisions, the relevant diagrams are shown in Figure 2.2 [15]. The square of the invariant matrix element for two-body scattering of massless partons are listed in Table 2.3. Here $\hat{s} = (p_1 + p_2)^2$, $\hat{t} = (p_1 - p_3)^2$, and $\hat{u} = (p_2 - p_3)^2$ are the Mandelstam variables for the hard scattering subprocess [15]. (p_1 and p_2 are the momenta of the initial-state partons, while p_3 and p_4 are the final-state momenta.)

The matrix elements for quark-quark scattering have been calculated to $O(\alpha_S^3)$. Some of the diagrams that contribute at $O(\alpha_S^3)$ are shown in Figure 2.3. For the two-to-three parton scattering processes, we can divide these into four groups:

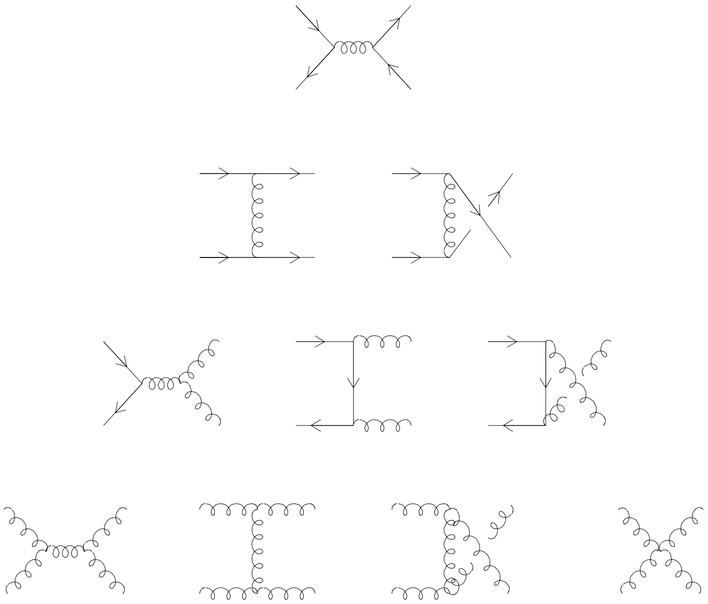

Figure 2.2: Leading Order (α_S^2) diagrams for two-body scattering. Lines represent quarks and curly symbols represent gluons.

$$
\begin{array}{lrcl}
(A) & q(p_1)+q'(p_2) & \rightarrow & q(p_3)+q'(p_4)+g(k) \\
(B) & q(p_1)+q(p_2) & \rightarrow & q(p_3)+q(p_4)+g(k) \\
(C) & q(p_1)+\overline{q}(p_2) & \rightarrow & g(p_3)+g(p_4)+g(p_5) \\
(D) & g(p_1)+g(p_2) & \rightarrow & g(p_3)+g(p_4)+g(p_5)
\end{array}
$$

In process A, the quarks q and q' are of different flavor, while the quarks in process B

Table 2.3: Invariant matrix elements for 2-to-2 scattering of massless partons.

Process	$\overline{\sum}\lvert\mathcal{M}\rvert^2/g^4$
$qq' \to qq'$	$\frac{4}{9}\frac{\hat{s}^2+\hat{u}^2}{\hat{t}^2}$
$q\overline{q}' \to q\overline{q}'$	$\frac{4}{9}\frac{\hat{s}^2+\hat{u}^2}{\hat{t}^2}$
$qq \to qq$	$\frac{4}{9}(\frac{\hat{s}^2+\hat{u}^2}{\hat{t}^2} + \frac{\hat{s}^2+\hat{t}^2}{\hat{u}^2}) - \frac{8}{27}\frac{\hat{s}^2}{\hat{u}\hat{t}}$
$q\overline{q} \to q'\overline{q}'$	$\frac{4}{9}\frac{\hat{t}^2+\hat{u}^2}{\hat{s}^2}$
$q\overline{q} \to q\overline{q}$	$\frac{4}{9}(\frac{\hat{s}^2+\hat{u}^2}{\hat{t}^2} + \frac{\hat{t}^2+\hat{u}^2}{\hat{s}^2}) - \frac{8}{27}\frac{\hat{u}^2}{\hat{s}\hat{t}}$
$q\overline{q} \to gg$	$\frac{32}{27}\frac{\hat{t}^2+\hat{u}^2}{\hat{t}\hat{u}} - \frac{8}{3}\frac{\hat{t}^2+\hat{u}^2}{\hat{s}^2}$
$gg \to q\overline{q}$	$\frac{1}{6}\frac{\hat{t}^2+\hat{u}^2}{\hat{t}\hat{u}} - \frac{3}{8}\frac{\hat{t}^2+\hat{u}^2}{\hat{s}^2}$
$gq \to gq$	$-\frac{4}{9}\frac{\hat{s}^2+\hat{u}^2}{\hat{s}\hat{u}} - \frac{\hat{u}^2+\hat{s}^2}{\hat{t}^2}$
$gg \to gg$	$\frac{9}{2}(3 - \frac{\hat{t}\hat{u}}{\hat{s}^2} - \frac{\hat{s}\hat{u}}{\hat{t}^2} - \frac{\hat{s}\hat{t}}{\hat{u}^2})$

are identical in flavor. The symbol $g(k)$ represents a gluon with momentum k. All other matrix elements for 2-to-3 parton scattering can be obtained by crossing ($a+b \to c+d$ is the same as $a+\overline{c} \to \overline{b}+d$). For process A above, the square of the matrix element is

$$\overline{\sum}\left|\mathcal{M}^{(A)}\right|^2 = \frac{4g^6}{9}\left(\frac{s^2+s'^2+u^2+u'^2}{2tt'}\right)\left(\frac{8}{3}\left([14]+[23]\right)+\frac{1}{3}[12;34]\right)$$

Here $g = \sqrt{4\pi\alpha_S}$ and

$$s = (p_1+p_2)^2, \quad t = (p_1-p_3)^2, \quad u = (p_1-p_4)^2$$

$$s' = (p_3+p_4)^2, \quad t' = (p_2-p_4)^2, \quad u' = (p_2-p_3)^2$$

and the eikonal factor $[ij]$ is

$$[ij] = \frac{p_i \cdot p_j}{p_i \cdot k \; k \cdot p_j}$$

and finally

$$[12;34] = 2[12] + 2[34] - [13] - [14] - [23] - [24]$$

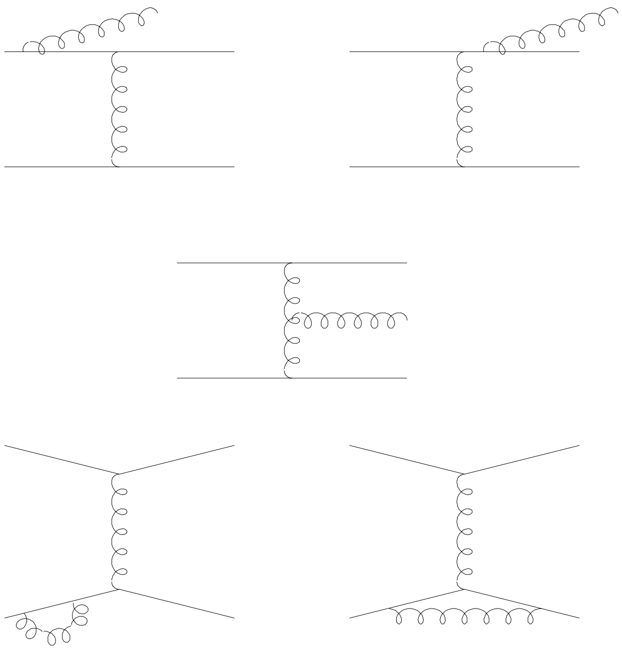

Figure 2.3: Diagrams for Next-to-leading order (α_S^3) two-body scattering. Lines represent quarks and curly symbols represent gluons.

The matrix elements in terms of s, t, u, etc., for processes B, C, and D are even more complicated and are given in Appendix A [16].

Parton Showering and Jet production

The development of a final-state parton to a jet is divided into two steps: First the *parton shower*, and then *hadronization.* The dividing line between the two steps is the value of the momentum-transfer scale, usually taken to be of order 1 GeV. In the parton shower, a quark or gluon can emit a gluon and decrease its momentum, or a gluon can split into a quark-antiquark pair. This continues until the partons have energies of 1 GeV or so. At this point hadronization occurs, which converts the partons into observed hadrons. The nearly collinear group of produced hadrons forms a macroscopic structure called a jet. The hypothesis of *local parton-hadron duality* equates the final energy and direction of a jet with that of the parton which gave rise to it [17].

The cross section for producing specific final-state hadrons can be studied to extract the *fragmentation function* $D_{h \leftarrow k}$, which is analogous to the parton distribution functions but gives the probability to produce a hadron h from parton k (see the upper-right leg in Figure 2.1).

Jet variables

The colliding proton and antiproton beams in our experiment have the same energy. However, the partons from each hadron do not carry the same momentum fraction, resulting in a partonic center of mass that is boosted relative to the hadronic center of mass. (The partons can also carry a small amount of "inherent" transverse momentum, but this is usually attributed to soft-gluon radiation, and often neglected.) It is therefore useful to work with quantities that transform simply with respect to boosts along the beam direction. The traditional variables used are rapidity (y), transverse momentum (p_T), and azimuthal angle (ϕ) of the jet. For a jet with energy E and momentum p, the rapidity (y) is defined as

$$y = \frac{1}{2} \ln \left(\frac{E + p_z}{E - p_z} \right)$$

the transverse momentum as

$$p_T = \sqrt{p_x^2 + p_y^2}$$

The transverse energy E_T is frequently used in place of p_T in cases where the mass of the object can be neglected or when the mass of the particle cannot be measured. In addition, the *pseudorapidity* η is usually defined in place of rapidity, again when the mass of the object is much smaller than its transverse momentum. The pseudorapidity (Figure 2.4) in terms of the polar angle θ (with respect to the beam direction) is

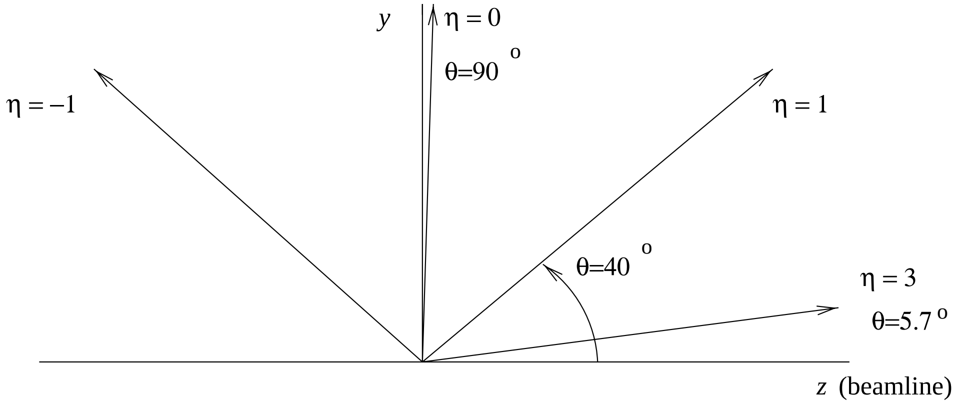

Figure 2.4: Pseudorapidity.

$$\eta = -\ln\tan(\theta/2)$$

and transverse energy can also be written as

$$E_T = E\sin\theta$$

Although the definition of a jet is somewhat arbitrary, the same definition should be used in experiment and in Monte Carlo in order to facilitate comparison with theoretical predictions. The jet algorithm used in DØ is known as the cone algorithm. Here, a jet is a concentration of transverse energy inside a "cone" of radius R, where

$$R = \sqrt{(\Delta\eta)^2 + (\Delta\phi)^2}$$

By using η instead of θ we ensure that the definition of a jet is invariant under longitudinal boosts [15].

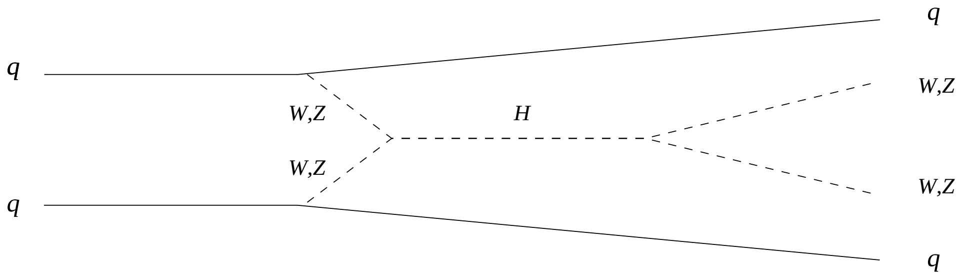

Figure 2.5: Higgs production via weak boson scattering.

2.6 Ratio of 3-jet and 2-jet cross sections

The goal of this measurement is to study the production rate of soft jets and to determine the scale for such soft-jet emissions. An application of this study is in weak boson scattering at LHC energies. In the process $qq' \to qq'H \to qq'WW$ (Figure 2.5) the event signature consists of jets in the forward and backward (large $|\eta|$) region and nothing in the central ($\eta \approx 0$) region. The major backgrounds to this process are $q\overline{q} \to t\overline{t} \to W^+bW^-\overline{b}$ and $q\overline{q} \to W^+W^-$. These backgrounds have a signature of jets in the central region. The ability to veto central jets in the trigger can enhance signal-to-background for the $qq' \to qq'WW$ process. Thus, an understanding of the production rate of soft jets in the central region can aid in designing a trigger to capture these events. The cross section ratio $\frac{\sigma_{3+}}{\sigma_{2+}}$ is a measure of the probability for the emission of a soft jet in dijet events [18] [19].

A measurement of $\frac{\sigma_{3+}}{\sigma_{2+}}$ gives us an estimate of the production rate for soft jets, while a comparison of $\frac{\sigma_{3+}}{\sigma_{2+}}$ using either a hard scale ($\mu_R = \sum E_T$) or a soft scale ($\mu_R = E_T^{(3)}$) in the Next-to-Leading Order calculation tells us whether the emission of soft jets is governed by the hard scattering scale or the soft scale [20].

Chapter 3

The Tevatron and the DØ Detector

3.1 Introduction

Our study of $p\overline{p}$ interactions was done at Fermilab (Batavia, Illinois). The creation, acceleration, and collision of protons and antiprotons was performed with the Tevatron accelerator at Fermilab. The detection of the products of collision was done using the DØ detector. This chapter will describe the Tevatron and the DØ detector.

3.2 The Tevatron

The Fermilab Tevatron is the largest of a series of accelerators working in sequence to produce and collide protons and antiprotons at a center-of-mass energy of 1.8 TeV. The main parts of the collider, in order of increasing beam energy, are: the Pre-Accelerator, the Linac, the Booster, the Main Ring, and the Tevatron. They are listed in Table 3.1. The layout of the accelerator is shown in Figure 3.1.

The first step in creating proton beams is the production of of H^- ions in the Pre-accelerator; it consists of a hydrogen ion source and an electrostatic accelerating column

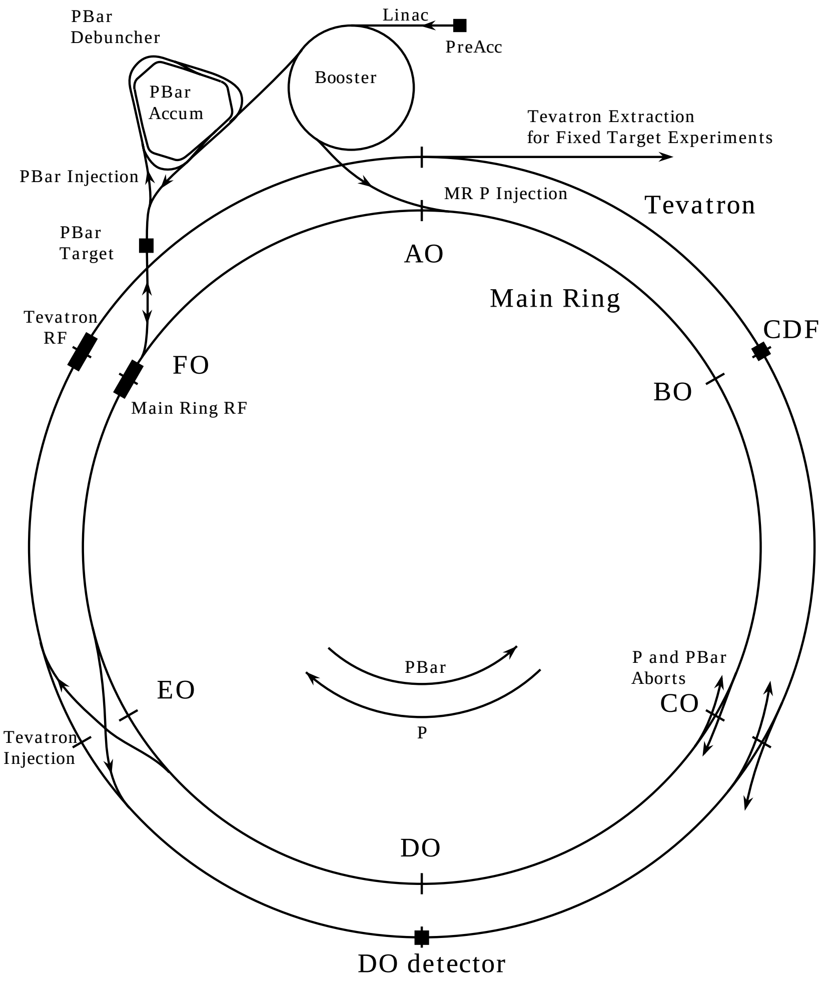

Figure 3.1: The Fermilab collider (not to scale)

powered by a Cockcroft-Walton generator. The H^- ions produced from a surface-plasma magnetron are accelerated through a 750 keV potential and then fed to the Linac.

The Linac consists of five steel "tanks" arranged end-to-end with a gap between the tube ends. An alternating electric field is applied inside the tanks. A charged particle is accelerated when it is in the gap between the drift tubes. Inside the tubes it is shielded from the field, and will simply drift. The frequency of the alternating electric field is such that an accelerating field is present when the particle is in the gap and a decelerating field is present when the particle is in the drift tube. As a particle travels down the

Table 3.1: Tevatron and associated accelerators

Name	Type	Start Energy	End Energy	Dimension
Pre-Accelerator	Linear	0 keV	750 keV	Height = 11 m
Linac	Linear	750 keV	400 MeV	Length = 146 m
Booster	Circular	400 MeV	8 GeV	Dia = 151 m
Main Ring	Circular	8 GeV	150 GeV	Dia = 2000 m
Tevatron	Circular	150 GeV	900 GeV	Dia = 2000 m

linac its energy increases and so the drift tubes become increasingly longer to maintain the same phase. In addition, the drift tubes contain alternate focussing and defocussing quadrupole magnets to contain the lateral spread of the ions due to space charge and RF effects. The ions have an energy of 400 MeV after leaving the Linac.

At the end of the Linac the H^- ions pass through a carbon foil to strip off the electrons, leaving only protons. The protons are fed to a synchrotron called the Booster. A synchrotron is a closed-orbit accelerator with magnets that bend the beam into roughly circular orbits, using cavity resonators to increase the energy of the beam. As the beam energy is increased the magnetic field strengths are correspondingly increased to keep the particles in the same path. The Booster then raises the energy of the protons from 400 MeV to 8 GeV. For extraction "kicker" magnets are used to transfer the entire beam in one turn.

The Main Ring is a 1000 m (radius) synchrotron that is capable of producing 400 GeV proton beams. As a feeder for the Tevatron is it used to raise the beam energy to 150 GeV. The Main Ring and Tevatron RF systems are phase-locked using common timing signals. The Main Ring RF system is then aligned with the Tevatron RF system and the proton bunch in injected into a Tevatron *bucket.*

The production of antiprotons begins with the Main Ring. The protons are accelerated to 120 GeV, extracted, and fired at a nickel target. Antiprotons with energies of 8 GeV are collected and stored in the Debuncher. Debunching is the process of reducing the momentum spread of the antiproton beam. The antiprotons are then injected into the Accumulator.

In collider mode, the antiprotons are extracted from the Accumulator and fed to the main ring. Proton bunches are also injected into the main ring, and travel in the opposite direction as the antiprotons. When the proton and antiproton bunches reach 150 GeV they are injected into the Tevatron where they continue to rotate in opposite directions. The Tevatron is similar in many ways to the main ring, sharing the same tunnel. The difference is in the use of superconducting magnets in the Tevatron. The proton and antiproton bunches are accelerated to 900 GeV and are made to collide at two points, where the CDF and DØ detectors are located. Additional information on the operation of the Tevatron can be found in Reference [21].

3.3 The DØ detector

The DØ (pronounced "D-zero") detector consists of three main parts that approximate layers surrounding the interaction point. From the center outward, these are the Central Detector, the Calorimeter, and the Muon Detector. A drawing of the detector showing all three systems is in Figure 3.2.

3.3.1 The DØ coordinate system

The coordinate system is defined such that the beams travel along the z axis, with protons moving in the $+z$ direction (south). The positive y direction is upward from the center of the detector. Lastly the positive x is defined so the overall coordinate system is right-handed (east). The polar angle θ is defined from the $+z$ axis. Another measure of polar angle is the pseudorapidity η, defined as

$$\eta = -\ln(\tan(\theta/2))$$

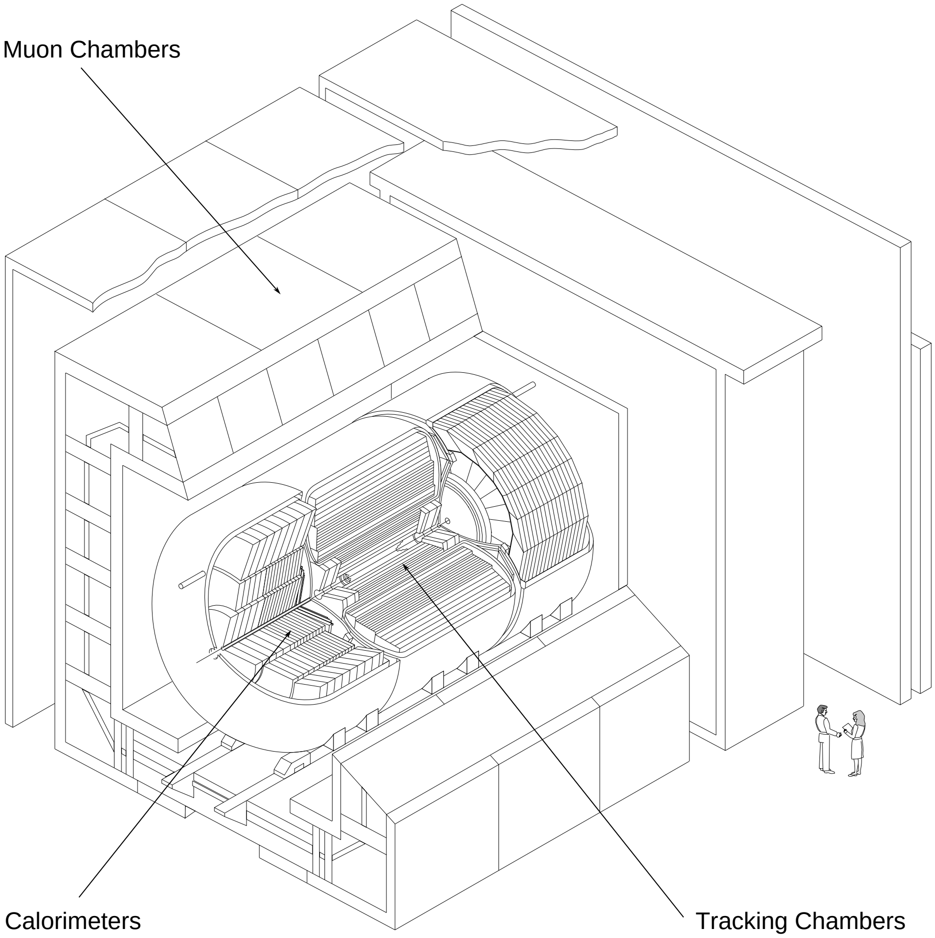

Figure 3.2: The DØ Detector

The azimuthal angle ϕ is measured from the $+x$ direction, toward the $+y$ direction. Particle and jet trajectories are usually given in η-ϕ "coordinates."

3.3.2 Central detector

The Central Detector consists of the Vertex Drift Chamber (VTX), the Transition Radiation Detector (TRD), the Central Drift Chamber (CDC), and two Forward Drift Chambers (FDC). See Fig 3.3. There are a total of 4200 wires and 6080 channels in the central detector. The innermost layer (Central Detector) is used for measurement of the interaction vertex (position in z, along the beamline), charged particle track measurement, and ionization energy measurement to distinguish electrons from photon conversion products ($\gamma \rightarrow e^+e^-$).

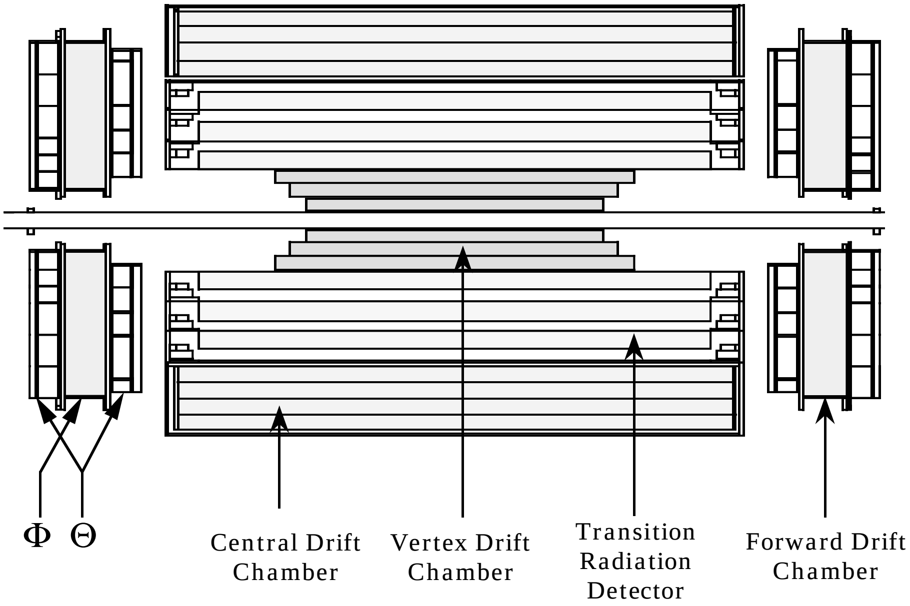

Figure 3.3: The Central Detector elements. Beam goes horizontally in the figure through the center beamline.

The vertex drift chamber (Fig 3.4) consists of three concentric layers of cells with wires running parallel to the beamline. Each cell has eight wires at different radial distances from the beamline and these determine the r-ϕ position of a track. The z-

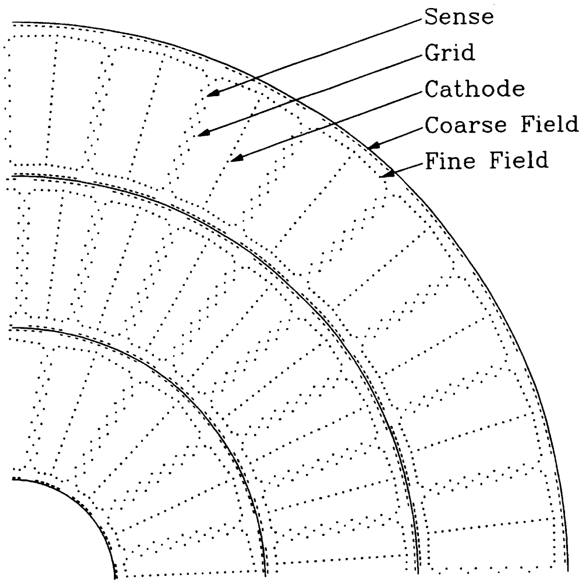

Figure 3.4: The layout of sense and grid wires in the Vertex Drift Chamber. The beam is oriented perpendicular to the page at the center of the arcs.

position is determined by reading the sense wires on both ends. The purpose of the vertex drift chamber is the measurement of the interaction vertex.

The Transition Radiation detector is located just outside the vertex chamber and is used to distinguish between electrons and hadrons. A charged particle traversing a boundary between two dissimilar materials (the "radiator") will emit x-rays (the *transition radiation*). In the TRD, the radiator is in the form of nitrogen gas and the radiation is detected using proportional wire chambers located downstream. The TRD has three sets of radiator and PWC pairs. The x-ray detector is performed in two stages. In the first stage the x-ray converts to an electron-positron pair ($\gamma \rightarrow e^+e^-$). In the second stage the conversion products and other particles are detected in a wire chamber.

The Central Drift Chamber (Figure 3.5) is part of the tracking system for the central region (perpendicular to beamline). The CDC has four layers, each with 32 cells. Each cell has seven sense wires read out at one end. Also there are two "delay lines" read out at both ends. These delay lines propagate signals induced from nearest anode wire. A measurement of differences in arrival times at two ends permit z-coordinate location.

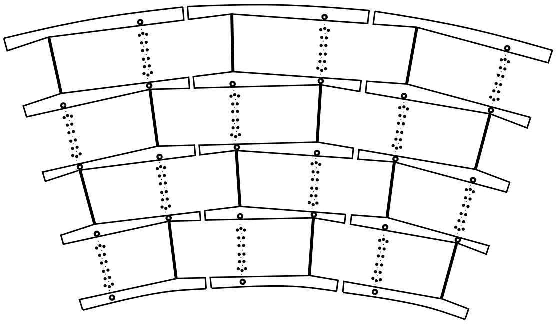

Figure 3.5: A cross-sectional view of the Central Drift Chamber.

Forward drift chambers (Figure 3.6) are used for tracking charged particle trajectories at small polar angles (almost parallel to beamline). The FDC has three layers of drift chambers, one Phi layer with sense wires oriented radially and two Theta layers surrounding the Phi with sense wires approximately in a circular pattern around the beamline. The parameters of the Central Detector elements are shown in Table 3.2.

Table 3.2: Central Detector Parameters

Central Detector				
Subsystem	Resolution	Radius	Height	Purpose
Vertex Drift Chamber VTX	50 μm	4-16 cm	104 cm	Determine interaction vertex
Central Drift Chamber CDC	150-200 μm	50-75 cm	184 cm	Charged particle tracking
Forward Drift Chamber FDC	150-200 μm	10-60 cm	40 cm	Charged particle tracking
Transition Radiation Detector TRD	π-e rejection of 50	16-50 cm	184 cm	Identification of electrons and pions

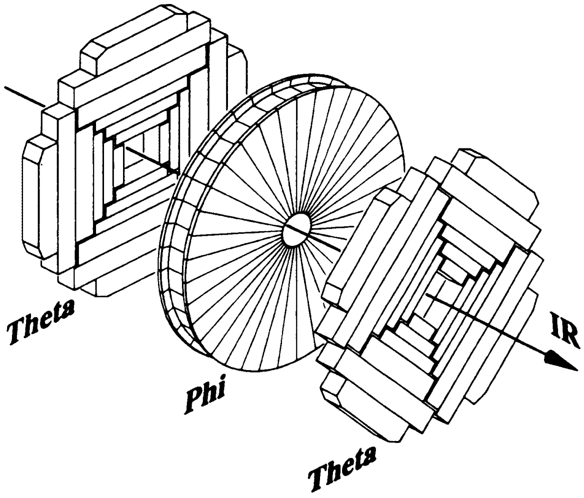

Figure 3.6: An expanded view of the Forward Drift Chambers, showing the three layers of drift chambers. The arrow shows the beam orientation and points to the center of the detector.

3.3.3 Calorimeter

The calorimeter is used to measure the energy of electrons, photons, and hadron jets. It is designed to cover nearly the full solid angle around the interaction region for good measurement of missing E_T and good coverage of the far-forward region (parallel to the beamline). Figure 3.7 shows a cutout view of the calorimeter, showing the three cryostats which contain the Central Calorimeter (CC) and the two End Calorimeter (EC).

As a particle travels through the calorimeter, it interacts with the calorimeter material and deposits its energy into the calorimeter material. A small fraction of this deposited energy is detectable as a signal that is proportional to the incident particle's energy, allowing its measurement.

The D0 calorimeter is made up of uranium and liquid argon layers (see Figure 3.8). The uranium acts as an absorber (inactive layer) which causes the primary particle to interact with it (Bremsstrahlung) and produce daughter particles which then ionize the liquid argon (active layer). A voltage of 2 kV is maintained across the liquid argon, between the uranium plate and an electrode. The negative ions produced drift toward

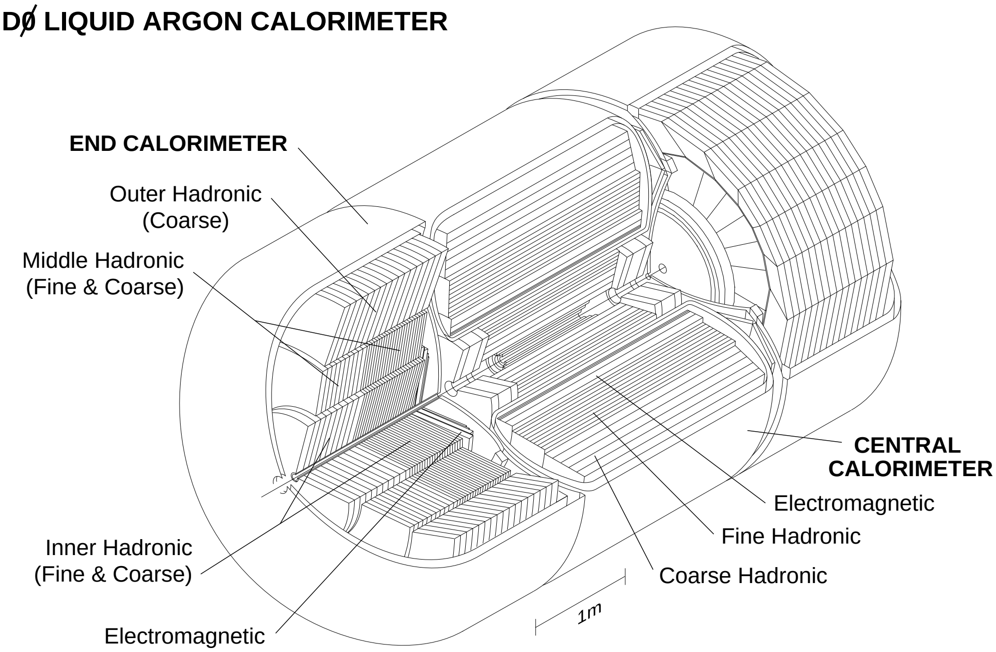

Figure 3.7: The DØ calorimeter showing different segmentation.

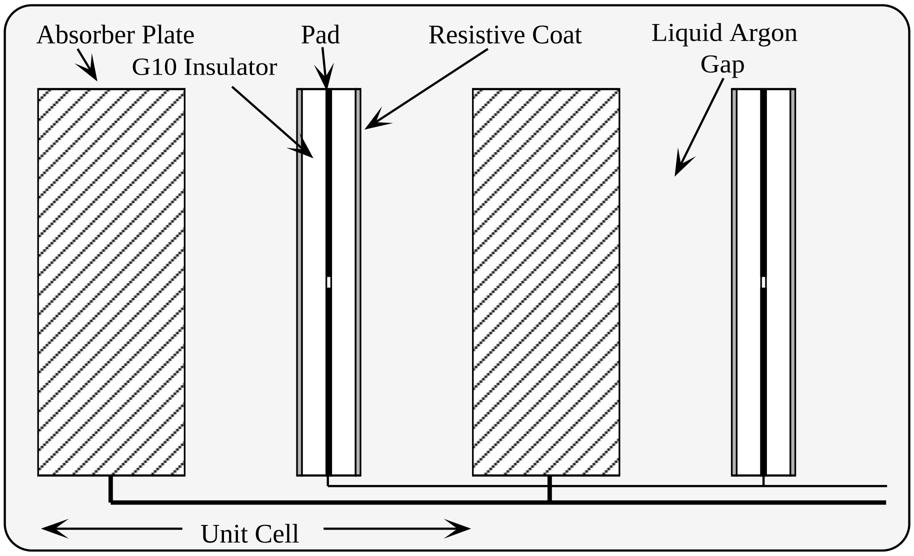

Figure 3.8: A schematic of a calorimeter cell.

the electrode, causing more ionization of the liquid argon. This produces a small current which is amplified and recorded. The collected charge is proportional to the energy of the incident particle.

To measure the position of the showers produced by charged particles, the combination of uranium and liquid argon is divided into segments or "cells", each instrumented independently (Fig. 3.9). The segmentation is done so that the cells are roughly the same size in η and ϕ (but not in x and y). In addition, there is segmentation in the radial direction to determine the "depth" of the shower. This is useful in distinguishing between electromagnetic objects (photons, electrons) and hadronic objects (pion, eta meson, rho meson, etc.) The choice of segmentation results in a natural grouping of cells of the same η and ϕ (*i.e.*, same "direction") but of different layers. This group

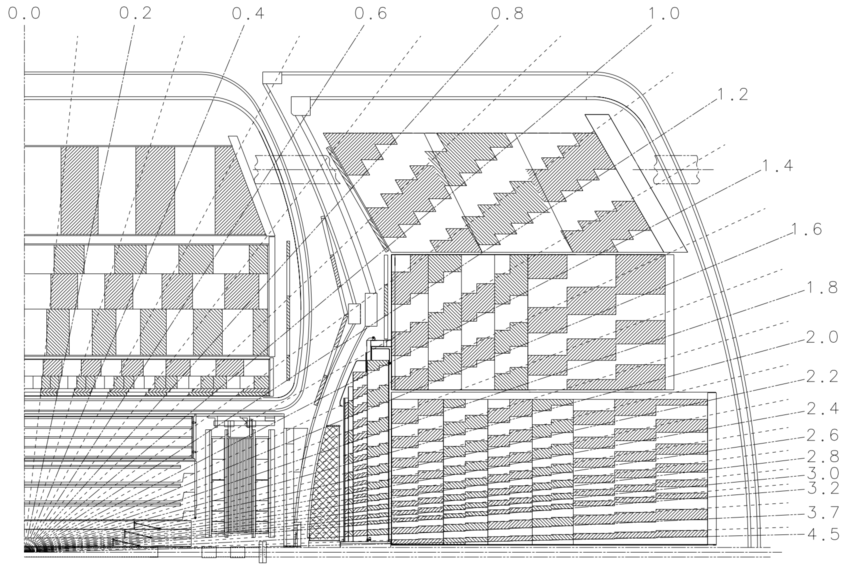

Figure 3.9: A view of a quarter of the calorimeter showing the fine longitudinal and transverse segmentation. The beams travel horizontally through the beam pipe shown at the bottom of the figure and the interaction region is approximately in the lower left corner of the figure.

Table 3.3: Calorimeter Parameters.

	Calorimeter
Spatial resolution	0.8-1.2 mm
Radius	75-500 cm
Height	306 cm (CC) 263 cm (EC)
Energy resolution	$15\%/\sqrt{E}(EM), 50\%/\sqrt{E}(Had), E$ in GeV
No. of channels	50,000

of cells with the same direction from the center of the detector forms what is called a *tower*. This concept of a tower will be used later in triggering and in the jet-finding algorithm. Cells have a size of 0.1 × 0.1 in η-ϕ (about 3 in. × 3 in.) in the central region (perpendicular to beamline at the interaction region) and 1.5 in. × 0.1 in. in the forward region (parallel to beamline).

The calorimeter surrounds the Central Detector on all sides. To allow access to the Central Detector the calorimeter was split into three parts, the central calorimeter (CC) and two end calorimeters (EC). In order to provide good spatial resolution while still keeping the volume (and hence cost) small, both the CC and EC have different modules with increasing distance from the interaction region: an electromagnetic (EM), a fine hadronic (FH) and a course hadronic (CH) section. The EM section uses thin uranium plates. The fine hadronic uses thicker uranium plates and the CH uses copper or stainless steel. The hadronic sections are further away from the interaction region since hadrons typically produce showers later than electromagnetic objects do.

Also, since electromagnetic objects (photons, electrons) produce smaller showers the segmentation in the EM calorimeter is finer than in the hadronic calorimeter. The position resolution of the calorimeter for isolated electrons is between 0.8 and 1.2 mm and varies as $E^{-1/2}$ where E is the particle energy. The calorimeter parameters are summarized in Table 3.3.3.

In order to keep the liquid argon at low temperatures, the calorimeter modules are placed in a double-walled cryostat. The cryostats are sealed, but have ports to exchange liquid helium and to provide a path for the amplifier signals to exit. Additional ports exist to pass high voltage, temperature, and purity monitoring signals. The calibration of liquid-argon response to energy deposition is dependent on the purity of the liquid argon, so a purity monitor is employed.

3.3.4 Muon system

The outermost detector system in DØ is the muon system. It is located outside the calorimeter. It is designed to measure muon momenta and charge. It consists of a toroidal magnet to deflect the muons and proportional drift tube chambers located before and after the magnet to record track coordinates. The track position is measured once before entering the magnetic field and twice afterwards. This is combined with vertex and tracking information from the Central Detector to determine the trajectory.

For a full description of the DØ detector see Reference [22].

Chapter 4

Data Acquisition, Trigger, and Offline Event Reconstruction

4.1 Introduction

The signals that come out of the detector are stored for later analysis. Before they are written to magnetic tape a filtering system is used to remove uninteresting events and reduce the signal rate to a manageable level. This is the purpose of the trigger and data acquisition (DAQ) system. The DAQ system (Figure 4.1) is a filter system in three stages that takes a quick look at each event to decide whether or not to save the information on that event. It has three levels of event characterization, called the Level 0, Level 1

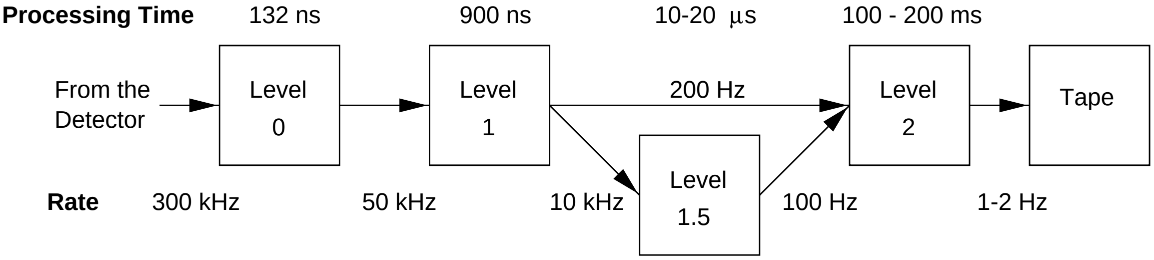

Figure 4.1: DØ trigger

and Level 2 *triggers*. In the next section I will describe in detail the Level 1, 2, and 3 triggers, followed by the offline data reconstruction, and ending with a description of the jet-finding algorithm used in the data reconstruction.

4.1.1 Level 0

The Level 0 trigger (Figure 4.2) uses the Level 0 detector, which is a pair of scintillator hodoscopes surrounding the beampipe and located at the inside face of the end calorimeter. The active elements of the hodoscopes extend radially to 45 cm from the beampipe and give coverage in the region $1.9 < \eta < 4.3$.

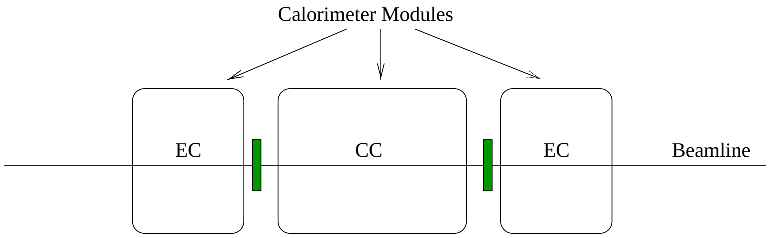

Figure 4.2: Level 0 Detectors. Shaded areas show the scintillator hodoscopes.

In addition to its use in the Level 0 trigger, it is also used to measure the instantaneous *luminosity* (the number of particles in a beam passing a boundary, per unit area, per unit time) that is "seen" by the whole trigger system. This is done by measuring the rate of interactions and using the known cross section for inelastic $p\overline{p}$ collisions. The Level 0 detectors are also used to measure the location of the interaction point along the beamline for use in the Level 1 and Level 2 triggers in calculating transverse energy.

A coincidence between the two Level 0 detectors indicates an inelastic collision and this prompts the next trigger stage to check the event. The efficiency of the Level 0 detector is 99% for non-diffractive inelastic collisions [23].

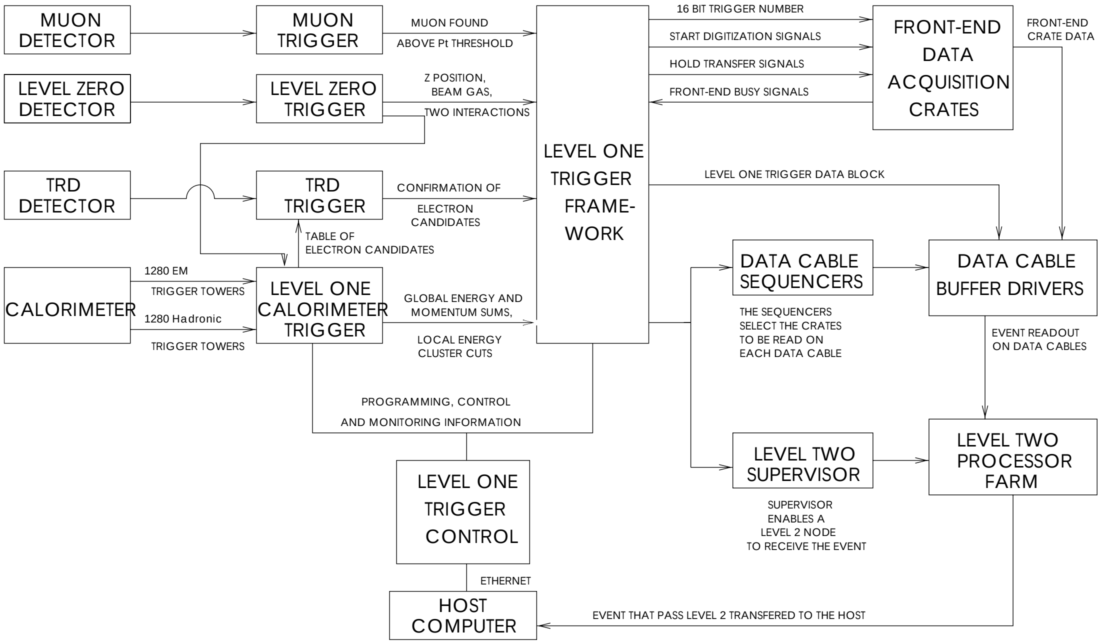

Figure 4.3: The Level 1 Trigger System.

4.1.2 Level 1

If an event passes the Level 0 trigger it is fed to the Level 1 trigger. A schematic of the Level 1 system is in Figure 4.3. The Level 1 trigger uses information from the calorimeter trigger and muon system trigger.

The signals from the different detector elements in the calorimeter are sampled and a quick calculation is made of quantities such as the total energy, missing E_T , and calorimeter trigger tower energies. The calculation of transverse energy uses an estimate of the z-position of the vertex from the Level 0 detector. These quantities are used either alone or in combination to form conditions that are required to be met, or else the event is dropped from further consideration. There are 32 different conditions that can be satisfied by the Level 1 trigger, with each condition being made up of one or more sub-conditions from the calorimeter or the muon system [22].

The decision-making in the combined L0 and L1 trigger has to be done within the 3.5 μs time-between-bunch-crossing in order to incur no deadtime. There is also a Level 1.5

trigger which requires more than one time period between bunch crossing to complete its calculation. The Level 1.5 trigger was not used in this analysis.

4.1.3 Level 2

When an event passes any of the 32 Level 1 conditions it is considered to have passed the Level 1 trigger and is handed off to the Level 2 system. The Level 2 system is a software-based decision making system that applies more sophisticated tests to events.

Because of the longer time scale for calculations in Level 2, an event data buffering and distribution system is used to allow several Level 2 calculations (one for each event) to be performed concurrently. The distribution system sends an event to one of 50 VAX workstations that perform the Level 2 calculations.

In Level 2, there are 128 different criteria (called *filters*) that can be satisfied by an event for that event to be kept and recorded. These criteria are made up of event quantities similar to Level 1 quantities but are more complex. The Level 2 filters also require the passing of a specific Level 1 trigger as part of its requirements list. [22].

For this analysis, the Level 2 filters used are the "single inclusive jet" triggers. These require that the event has one or more jets above a minimum jet E_T . Because the E_T distribution of jets is steeply falling, several inclusive-jet filters with different trigger thresholds are used to sample the entire spectrum with good statistics.

Some Level 2 filters pass events at a rate that is still too high for writing to tape. In these instances a fraction of events are simply thrown away with the assumption that this is done without bias. When calculating the rates for a trigger, the recorded number of events is scaled accordingly. When an event passes the Level 2 filter it is written to 8mm tape. These events constitute the "raw data."

4.2 Offline processing

4.2.1 Farm

A small fraction of events are analyzed immediately in the Online system in order to check that both the detector and the data acquisition systems are working properly. However most of the data is written to tape and its reconstruction done in a separate system called the offline system. The main reconstruction of the raw data is done a Unix "farm."

The Unix farm was a group of networked Silicon Graphics or IBM workstations running the event reconstruction program called RECO. The basic unit of the farm is an "I/O node" which acts as the event server and eight "worker nodes" which run RECO and return the output back to the I/O node. Process control such as tape-to-disk (and vice versa) spooling and file naming are done on the I/O nodes. The input to the farm are raw data tapes and the output is the same data in a different, more manageable format. These formats may go through one or more additional reprocessing steps in order to group together events that are of interest to a given physics analysis subgroup

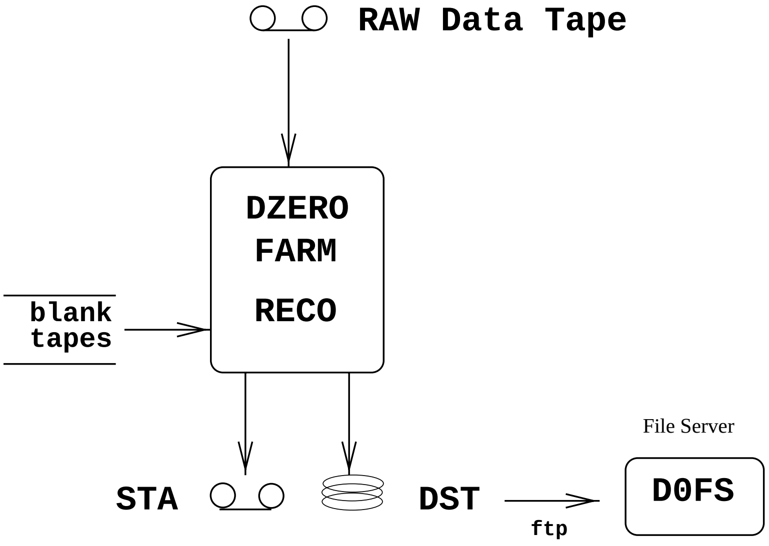

Figure 4.4: Offline Data Processing Farm

or to strip off unneeded information to reduce the final file size. A schematic of the farm is shown in Fig 4.4.

The reconstruction program produces two output files: STandard Output (STA, 600 Kbyte/event) and Data Summary Tape (DST, 20 Kbyte/event). The STA files contain all the information in the RAW data as well as parameters of reconstructed objects (electrons, photon, jets, muons, etc.) The DST files contain a stripped-down version of the STA, with the most important information in an event. Frequently some low-level information is stripped off to produce compressed versions of the above called microSTA and microDST. In this analysis the microDSTs are reduced even further to produce ntuples (Section 4.2.3). [22].

4.2.2 Event reconstruction

The reconstruction program RECO converts the signals from the different detector systems (Central Tracking, Calorimeter, and Muon System) into candidate objects such as electrons, photons, muons, jets, and taus. It also calculates event quantities such as missing E_T and total E_T , interaction vertex location, Central Detector tracking information, and muon tracking.

The z-position of the point where the partons from the proton and antiproton collide is called the interaction vertex. Accurate measurement of this vertex is needed as other measured quantities depend on it. The vertex is measured in several ways for different purposes. A quick determination of the vertex from the Level 0 detectors is used in triggering by the Level 2 trigger. A more precise and accurate vertex measurement is taken using the Central Drift Chamber (CDC). The measured vertex is used to calculate particle transverse energies and directions. A requirement that that the vertex be in the range -100 cm and $+100$ cm is made in the reconstruction process. Events whose measured vertex is beyond this range are not reconstructed. This is to ensure that the hard scatter occurs well within the detector.

Jet algorithm

A key element of RECO is the jet reconstruction algorithm. Interactions which produce final-state jets will deposit energy into the calorimeter. Because the calorimeter is divided into cells, a procedure for choosing which cells will be considered in defining the jet is needed. This is the purpose of the jet algorithm.

In this analysis a *fixed-cone* algorithm is used. (This algorithm is a slight variant of the so-called Snowmass jet algorithm [24].) Here a jet is defined by the total energy deposited within a "cone" in η-ϕ space. The size of the cone is given by its *radius* R:

$$R = \sqrt{\eta^2 + \phi^2}$$

A reconstruction cone radius of 0.7 is used in this analysis because it contains most of the energy of a jet and is a standard size used by the DØ and CDF experiments with well-understood systematics [25]. It is also important for the algorithm to be infrared-safe when used in theoretical calculations, to facilitate comparisons between a measured quantity and a calculated theoretical prediction [6].

The cells in the calorimeter with the same η and ϕ (but different layers) are grouped together into *towers*. The tower structure is shown in Figure 3.9. The jet finding process begins with listing all the calorimeter towers which have energy deposits in them. These are sorted in decreasing E_T . The largest E_T tower is used as a *seed*. Any towers adjacent to it that have an E_T greater than 1 GeV are associated with that seed tower (Figure 4.5). This continues with other adjacent towers up to a maximum 0.3 units in η or ϕ. The product of this step is called a *precluster*. The towers included with the first seed are removed from the tower list and the remaining tower with the highest E_T becomes the next seed. The process of associating adjacent towers is repeated for this and later seeds. This continues until no seed with E_T above 1 GeV remains [23].

Using the list of preclusters from the previous step, the algorithm calculates an E_T -weighted axis for that precluster. A cone in η-ϕ space is "drawn" around that axis and

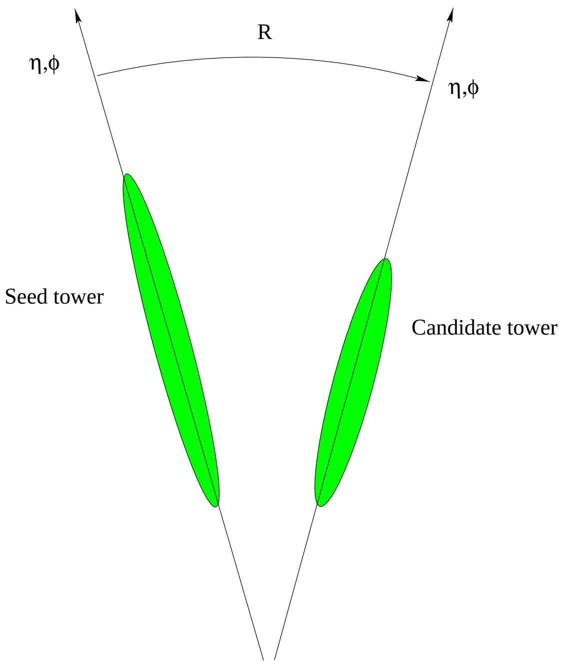

Figure 4.5: Preclustering.

all towers within that cone constitute a jet. A new E_T - weighted axis is calculated from all associated towers, and the process of drawing a cone is repeated until the jet axis changes by less than 0.001 in η-ϕ space or the number of iterations exceeds 50. If the jet has an E_T greater than 8 GeV it is stored and tested for splitting and merging (see below). This process is repeated for all preclusters.

As each jet in the previous step is constructed independent of other jets, it is possible for two jets found above to share one or more calorimeter towers. This is resolved by the *Split/Merge* process. If a jet (starting with the second) shares any towers with a previously found jet, the two jet axes are compared. If they differ by less than 0.01 in η-ϕ space then they are considered the same jet. This may happen due to round-off errors. The second jet is then dropped from the list. If the two jets are not identical, then a decision on whether and how to divide the jets is made using the quantity f

defined as

$$f = \frac{E_{T\ \mathrm{shared}}}{E_{T\ \mathrm{min}}}$$

where $E_{T\ \mathrm{shared}}$ is the transverse energy shared by the two jets, and $E_{T\ \mathrm{min}}$ is the smaller of the two jets' E_T . If $f \leq 0.5$ then the two jets are considered separate and the shared *cells* are assigned to one jet or another depending on which cell in the shared tower is closest to a jet axis. If f is greater than 0.5 then the two jets are combined into one. The towers from both jets are used to calculate an E_T - weighted direction, which becomes the direction of the "merged" jet.

Missing E_T measurement.

The DØ calorimeter is designed to completely surround the interaction region except for the beampipe. For this reason, an imbalance in the momentum measurements is attributed to the presence of very weakly interacting particles (neutrinos and muons). The "missing energy" may be attributed to these particles. It is more common to measure the missing transverse energy ($\not{E}_T$). It is defined as the vector E_T that balances out the sum of all measured vector E_T s. The measurement of missing E_T is used to remove contaminated events (Section 5.3.1).

4.2.3 Data structure

The end product of offline data reconstruction is a series of events, each consisting of a set of quantities that describe the event. The variables that make up the data structure of an event include such quantities as:

- The (serial) run number.
- The (serial) event number for this run.
- The instantaneous luminosity for the event.

- The Level 2 triggers the event passed (can be more than one).
- The z-position (along beamline) of the interaction point, as calculated by both Level 0 and the Central Detector.
- The number of charged-particle tracks seen by the tracking chamber
- The number of jet candidates found by the reconstruction algorithm
- The total energy deposited into the calorimeter.
- The measured missing E_T of the event.

In addition, there are also variables that relate to specific objects within an event. For example, for each *jet* found the following jet information is recorded:

- The energy of the jet
- The transverse energy of the jet
- The direction of the jet (η, ϕ, θ)
- The jet energy before rescaling (Section 6.6)
- The fraction of the jet energy deposited in different calorimeter modules (Electromagnetic, Hadronic)

The final data set takes the form of "n-tuples." An ntuple is a list of identical data structures, one for each event [26]. The flexibility and compactness of the ntuple data structure allows the selection of subsets of the data sample using selection criteria based on one or more variables.

Chapter 5

The Data and Measurement of the Cross Section Ratio

5.1 Introduction

In this chapter I describe in detail the measurement of the cross section ratio. I begin with a description of the data sample, followed by the selection criteria used to clean up the sample. Lastly, I outline the method used to combine the separate data sets (from different triggers) into one.

5.2 Data sample

The data used in the analysis is from the 1992-1993 Collider run. The total data sample, consisting of 40542 events, was recorded using the "single-jet inclusive" triggers. These triggers are designed to collect events that contain at least one hadron jet with transverse energy (E_T) above a particular threshold value. Five different thresholds are used: 20, 30, 50, 85, and 115 GeV. These are named JET_20, JET_30, JET_50, JET_85, JET_115. A distribution of the event jet multiplicity (number of jets in the event) for events from all five triggers is shown in Figure 5.1 and tabulated in Table 5.1.

Table 5.1: Jet multiplicity

No. of jets	Events
2	16,384
3	16,201
4	5,922
5	1,584
6	352
7	84
8	12
9	3

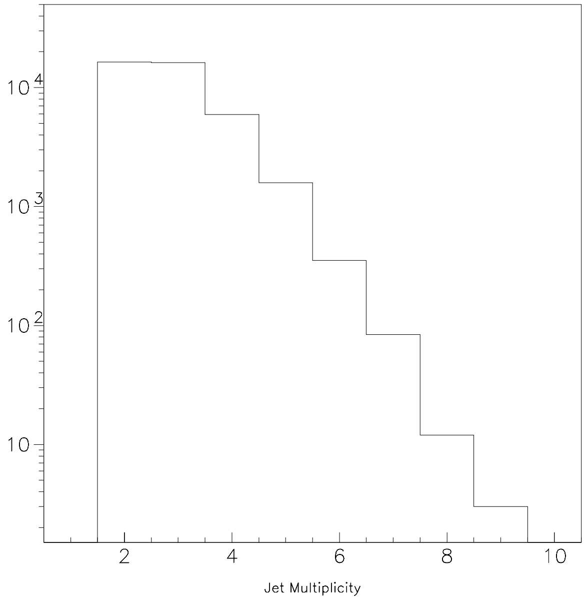

Figure 5.1: The distribution of jet multiplicities.

5.3 Event and jet selection criteria

The output of event reconstruction is a set of candidate events, with each event containing one or more candidate jets. Event and jet selection criteria are applied to "clean up" the data sample. The selection criteria fall into two categories: event selection criteria and jet selection criteria. Event selection criteria are applied to variables that pertain to an event as a whole, such as missing E_T ($\not\!\!E_T$). If an event fails to satisfy the requirements, the event is thrown out. Jet selection criteria are requirements on individual jet candidates which make use of jet variables. These are used to separate true hadronic jets from fake jets caused by instrumentation problems. If a jet fails to satisfy the requirements, that jet is not included in the count of jets in the event. For all remaining good events, the jet multiplicity is the number of jets which pass the jet requirements. Sum of all the "good" jet E_T 's is called H_T :

$$H_T = \sum_{\text{jets}} E_T$$

Studies have been performed to determine the optimal requirements for each event and jet variable. The results of these studies have been documented [27] [28] and are used as a starting point in this analysis.

5.3.1 Criteria for missing E_T

Recall that missing E_T is a measure of "missing energy" in a system that is designed to surround the interaction vertex and detect nearly all the final-state particles produced. The presence of missing E_T ($>$ few GeV) indicates either the production of weakly-interacting particles (such as a neutrino), or a mis-measurement of energy depositions in the detector. For example, a cosmic ray passing through the detector during a collision will deposit energy into the calorimeter. In most cases this results in an imbalance in transverse energy and consequently a large missing E_T relative to the *leading jet*(highest E_T jet) E_T . We require, then, that the ratio of the event missing E_T ($\not\!\!E_T$) to the E_T of

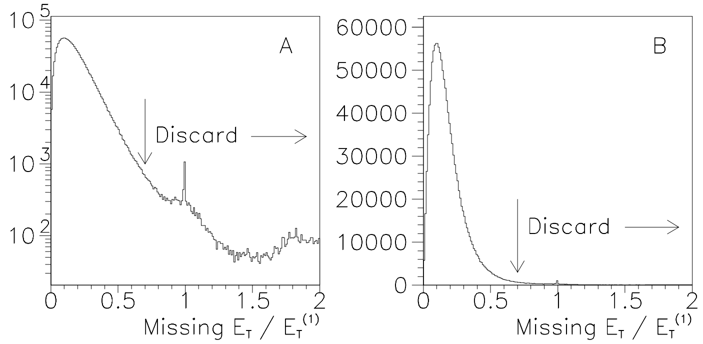

Figure 5.2: Logarithmic and linear plots of missing E_T /$E_T^{(1)}$. We require this ratio to be less than 0.7.

the leading jet be less than 0.7 (Figure 5.2.) This requirement was designed to remove events that coincide with cosmic rays passing through the calorimeter [27] [28].

5.3.2 Jet selection criteria

The following selection criteria are applied to individual jet candidates in an event. If the requirement is met, the jet is retained and counted in the jet multiplicity of that event.

Jet pseudorapidity (η)

An η requirement is applied which removes jets with an η greater than 3.5. The DØ calorimeter is instrumented to $\eta = 4.2$. A jet with its final determined direction very near the boundary of $\eta = 4.2$ would likely have some of its energy in a region beyond $\eta = 4.2$. The measured energy would then be an underestimate of its true energy. Because we are using a cone size R of 0.7 in our jet finding algorithm, we place a limit on jets with a measured $\eta < 3.5$ so that even at that η, the full 0.7 cone is within the instrumented region of the calorimeter.

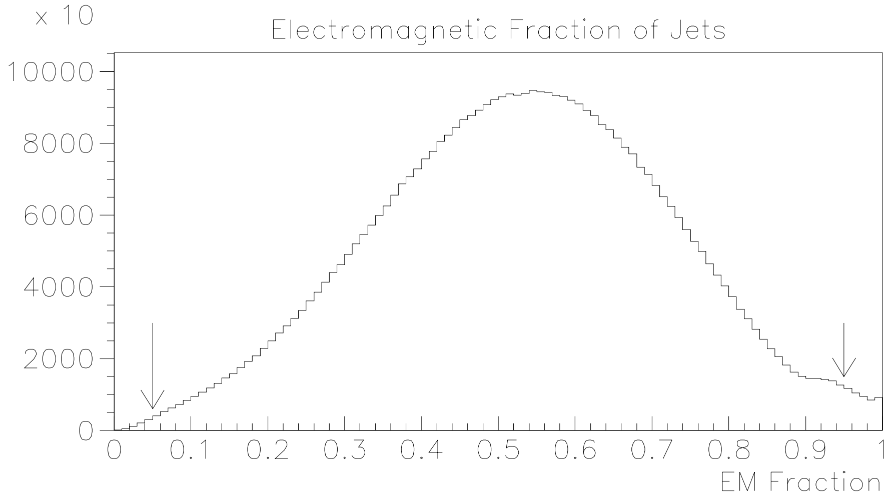

Figure 5.3: Electromagnetic Fraction for all candidate jets. We require jets to have an EM fraction between 5% and 95%.

Electromagnetic fraction (EM)

The jet electromagnetic fraction (EM fraction) is the fraction of a jet's energy that is deposited in the electromagnetic layers of the calorimeter. The requirement is that jets have an EM fraction between 5% and 95% (Figure 5.3.) Very low values of the EM fraction are due to calorimetric noise in the coarse and fine hadronic layers, while very high EM fraction values are due to EM calorimeter noise, electrons, or photons [28].

Table 5.2: Event and jet selection criteria (S.C.)

	Name	Description
Event S.C.	Missing E_T	$E_T{}^{(1)}/\not{E}_T = 0.7$
	N_{jets}	$N_{jets} \geq 2$
Jet S.C.	Jet η	all jets have $-3.5 < \eta < 3.5$
	CH fraction	CHF < 0.4
	EM fraction	$0.05 <$ EMF < 0.95
	Hot Cell ratio	Hottest/2nd hottest$<$ 10.

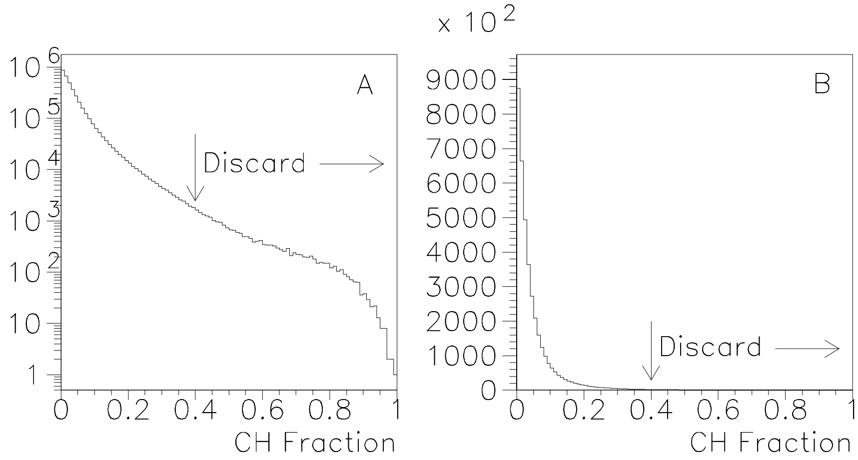

Figure 5.4: Coarse hadronic fraction for all candidate jets. We flag as good all jets with CHF$<$ 0.4.

Coarse hadronic fraction (CH)

This requirement is designed to remove fake jet candidates caused by activity in the Main Ring. The Main Ring is the next-to-the-last stage in acceleration before the protons and antiprotons are transferred to the Tevatron ring. At DØ, the main ring passes through the upper part of the calorimeters (both central and end) in the coarse hadronic section (see Figure 3.9). When protons and antiprotons are accelerated in the main ring at the same time Tevatron collisions are taking place, a collision in the main ring between the proton bunches and gas molecules will result in showers that deposit energy primarily in the hadronic section of the calorimeter. A jet candidate with a high fraction of its energy in the coarse hadronic section is most likely a jet coming from beam-gas interactions in the main ring. The limit placed on the CH fraction is 40%, meaning that if more than 40% of a jet's energy is in the coarse hadronic section of the calorimeter, the jet is rejected as a main-ring effect (Figure 5.4).

Hot cell ratio

The energy of a jet is distributed over many calorimeter cells. When one cell in a cluster has much more energy than the other cells (a "hot cell"), it is likely that the extra energy is due to instrumentation effects. The requirement for a good jet is that the energy in the most energetic cell can be no more than 10 times the energy of the next-most-energetic cell (see Figure 5.5).

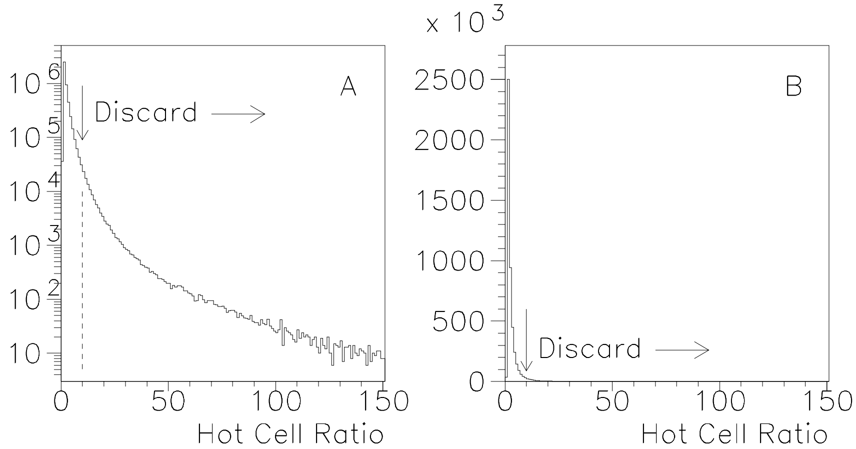

Figure 5.5: Hot cell ratio distribution. This is the ratio of the energy of the most energetic cell to the second most energetic cell. This ratio must be less than 10 to flag the jet as good.

5.4 Efficiencies of the inclusive jet triggers

Triggers used in filtering the data stream from the detector may suffer inefficiencies which can bias the resulting data set. The *efficiency* of a trigger is defined as the probability that an interaction having the required properties actually passes the trigger criteria as implemented. One source of inefficiency is reduced accuracy in the quick measurements of the event's characteristics (like jet E_T). This loss of accuracy can lead to false-positives and false-negatives. The result of these errors in triggering is called *trigger bias.* These errors are more pronounced when the event's characteristics are near the boundaries of the trigger.

Studies have determined the efficiencies of the single-jet triggers used in this analysis [29] [30]. The efficiencies are determined from data taken during collider runs called "Mark-and-Pass" runs. In these runs, all events passing the first level (Level 0) trigger are recorded, regardless of whether they pass the second and third trigger levels. The comparison of events that would have failed to pass the trigger and those that pass characterizes the efficiency of the trigger. This efficiency is measured as a function of event characteristics such as leading jet E_T and leading jet direction (in η). The measured efficiencies are parametrized for use in a FORTRAN subroutine.

The average trigger efficiencies as a function of H_T ($\sum E_T$) of the five triggers used in this study are shown in Figures 5.6, 5.7, and 5.8. The plots show the average

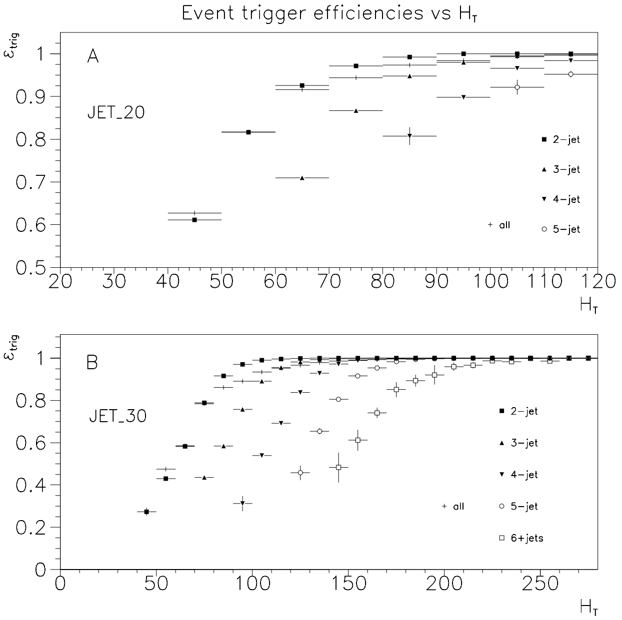

Figure 5.6: Event trigger efficiency vs H_T for different jet multiplicities (20 [A] & 30 [B] GeV triggers).

event trigger efficiency as a function of the H_T of the event for events with 2, 3, 4, or 5

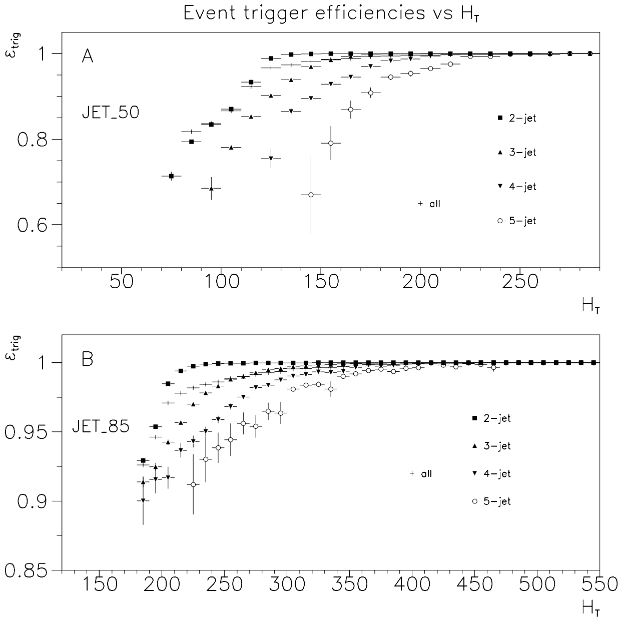

Figure 5.7: Event trigger efficiency vs H_T for different jet multiplicities (50 [A] & 85 [B] GeV triggers).

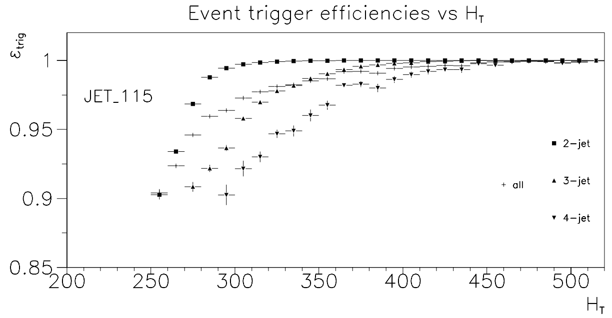

Figure 5.8: Event trigger efficiency vs H_T for different jet multiplicities (115 GeV trigger).

jets. In the low H_T region, high-multiplicity events have lower average trigger efficiency than low-multiplicity events. The differences in efficiency decrease at higher H_T . The reason for this effect is that at a particular H_T , a high-multiplicity event shares its total transverse energy with more jets, reducing the average jet E_T . This results in an overall lower trigger efficiency for high multiplicity events in H_T ranges just above the trigger threshold.

5.5 Measurement of the ratio of cross sections

As seen in Figure 5.1, each event contains anywhere from two to 9 jets. We calculate for each event a quantity called H_T defined as the sum of the jet transverse energies:

$$H_T = \sum_{\text{jet } i} E_T^{(i)}$$

for all jets above a fixed E_T threshold. We produce a distribution of H_T for all events. In each H_T bin we calculate the fraction of events that have three or more jets:

$$\frac{\#\text{ events with 3 or more jets}}{\#\text{ events with 2 or more jets}}$$

This ratio is equivalent to the cross section ratio $\frac{\sigma_{3+}}{\sigma_{2+}}$:

$$\frac{\sigma_{3+}}{\sigma_{2+}} = \frac{\sigma(\ p\overline{p}\ \rightarrow n\text{ jets} + X\ ;\ n \geq 3)}{\sigma(\ p\overline{p}\ \rightarrow m\text{ jets} + X\ ;\ m \geq 2)}$$

since factors relating the number distribution to the differential cross section cancel out in the numerator and denominator. Figure 5.9 shows the measured ratio for all five triggers over the fill range in H_T . The different sets of points have similar characteristics. There is an initial steep increase in the cross section ratio with H_T , which levels off. All five curves from the five triggers level off at roughly the same value (0.7). The sharp increase occurs at different regions of H_T related to the trigger threshold. The reason for this is

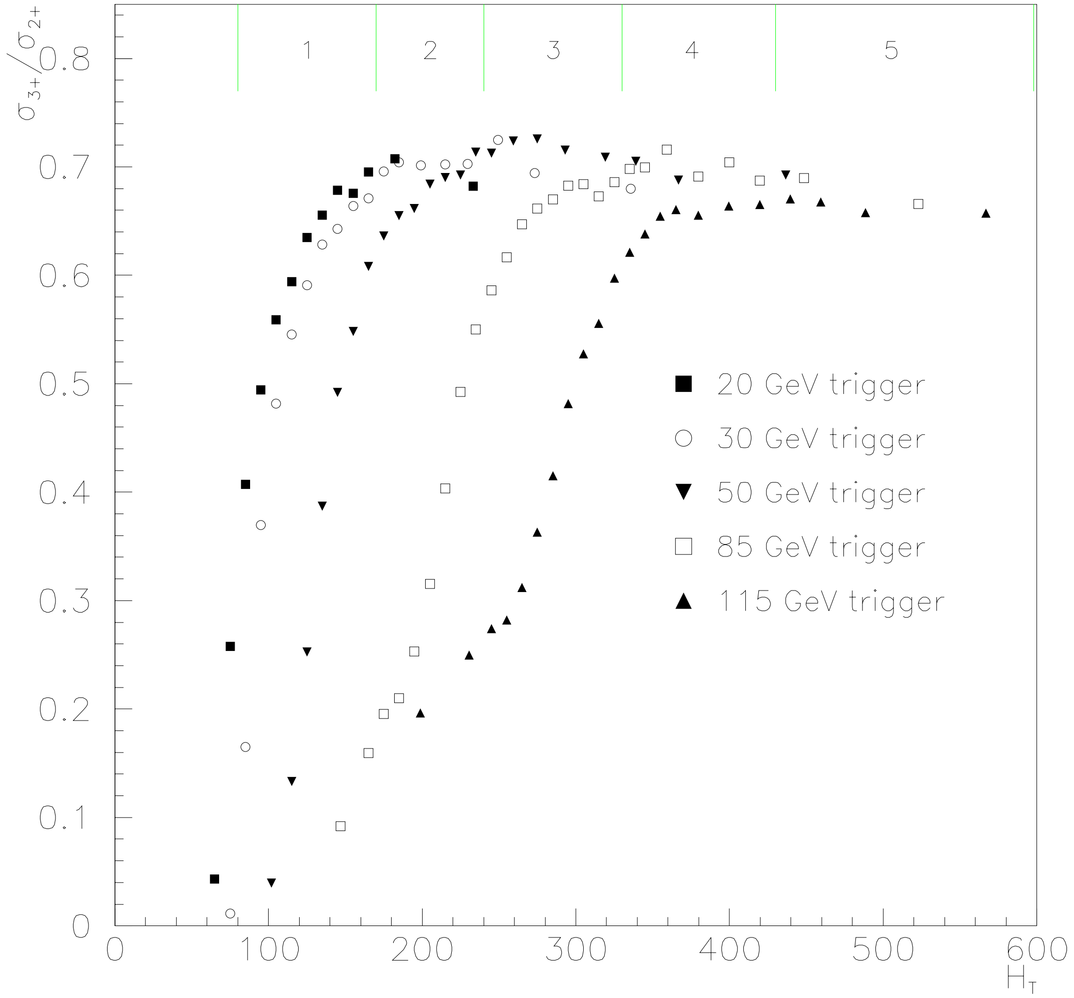

Figure 5.9: $\frac{\sigma_{3+}}{\sigma_{2+}}$ for all five triggers. The larger the trigger threshold, the higher the H_T value at which $\frac{\sigma_{3+}}{\sigma_{2+}}$ "saturates." The vertical lines at the top indicate the trigger used in different H_T ranges.

Table 5.3: H_T range used in each trigger.

Trigger	H_T range (GeV)
JET_20	80-170
JET_30	170-240
JET_50	240-330
JET_85	330-430
JET_115	430-600

primarily kinematic but is also affected by the trigger efficiency. In the case of the 50 GeV trigger (▼), for example, a three-jet event requires at least (50+20+20)=90 GeV to register in the cross section ratio, so the curve for that trigger has a starting point of 90-100 GeV. In order to test this, we compare the results to simulations using the Monte Carlo event generator HERWIG [31] [32]. The event generator is run using five different configurations corresponding to the five data triggers. In each configuration, a jet is required to have an E_T greater than 20, 30, 50, 85, and 115 GeV. The ratio $\frac{\sigma_{3+}}{\sigma_{2+}}$ is calculated for each, and compared to the measurement from the data. As seen in Figure 5.10, the HERWIG result is very similar to the data, with a small difference in overall normalization.

The "changeover" point from one data trigger to the next is chosen as the point where the curves for the two triggers coincide within errors. The changeover points are marked on the plots with vertical lines at the top, and Table 5.3 lists the H_T range used with each trigger. Figure 5.11 shows the cross section ratio using events from each trigger in the optimized H_T ranges of Table 5.3. The measurement begins at an H_T of 80 GeV. This point is chosen to be as low as possible but still have a high trigger efficiency of events in the region. The starting points for each trigger are also checked to ensure that the events are also trigger efficient. A correction for trigger inefficiency is made by scaling the event weights appropriately. In all cases the corrections amount to less than 1%.

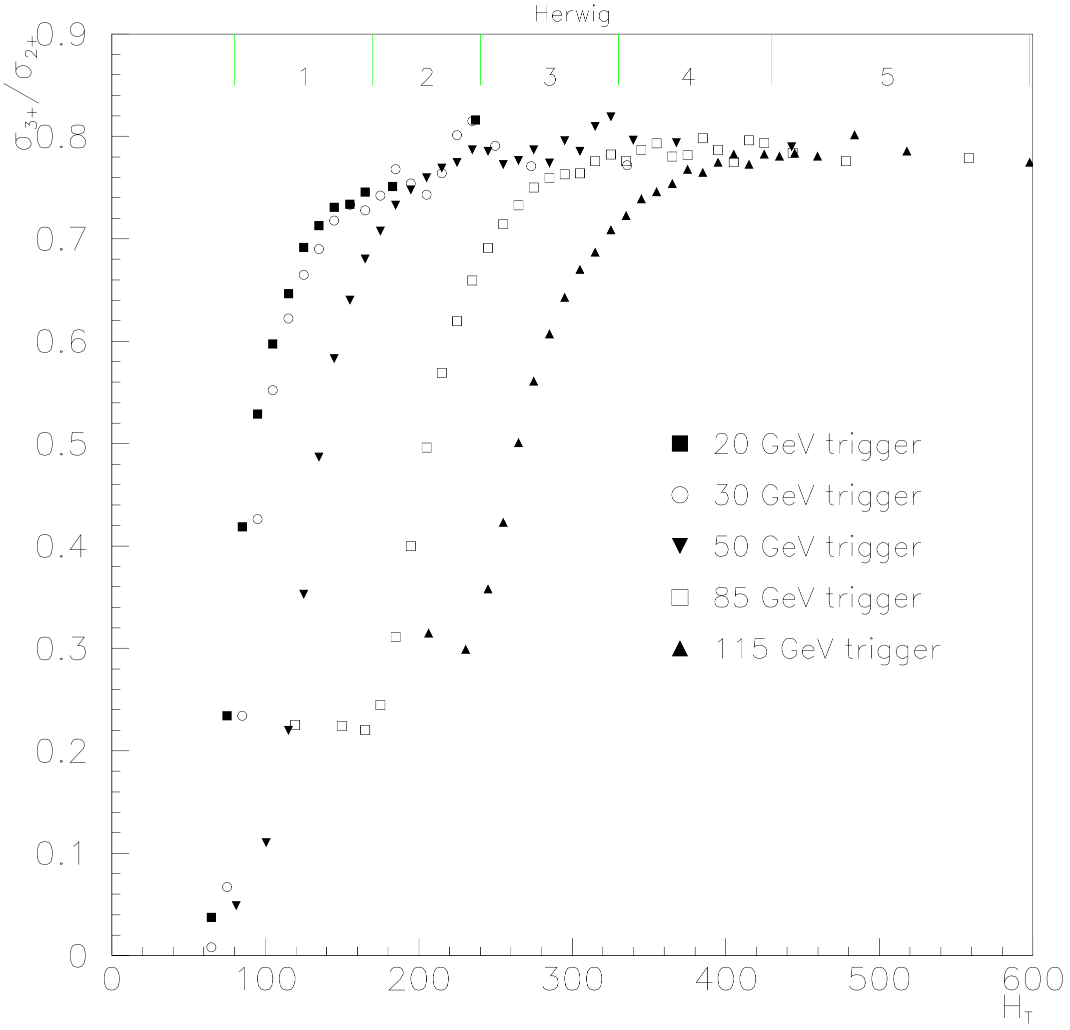

Figure 5.10: $\frac{\sigma_{3+}}{\sigma_{2+}}$ for all five pseudo-triggers, using HERWIGMonte Carlo. The triggering effect was simulated by requiring the highest E_T jet to have an E_T above the chosen thresholds.

5.6 Minimum jet-E_T requirement

The jet multiplicity of an event is the count of good jets above a minimum E_T threshold. Changing this threshold changes the jet multiplicity as well as the H_T of an event. The lower bound of the jet E_T threshold is determined by calorimeter response nonlinearities [43] , uninstrumented regions in the calorimeter, trigger efficiency, and reconstruction jet-finding efficiency. In this analysis we vary the minimum jet E_T from 20 GeV to 40 GeV and analyze the effect of changing the value of this threshold. Figure 5.12 shows $\frac{\sigma_{3+}}{\sigma_{2+}}$ vs H_T for minimum E_T thresholds of 20 and 30 GeV. The shape of the two curves are similar, but, as expected, the ratio decreases with increasing minimum jet E_T over the full range in H_T .

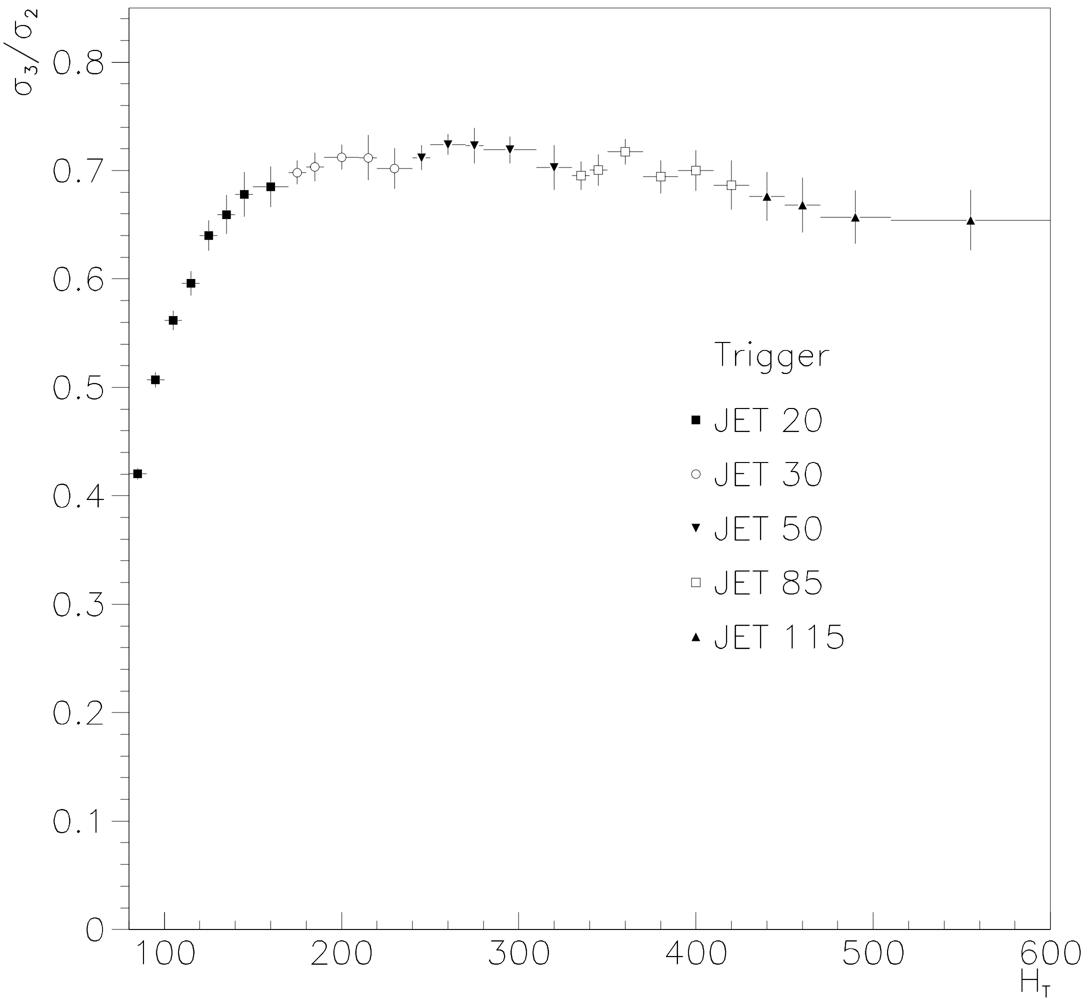

Figure 5.11: $\frac{\sigma_{3+}}{\sigma_{2+}}$ showing the breakdown of data points from different triggers.

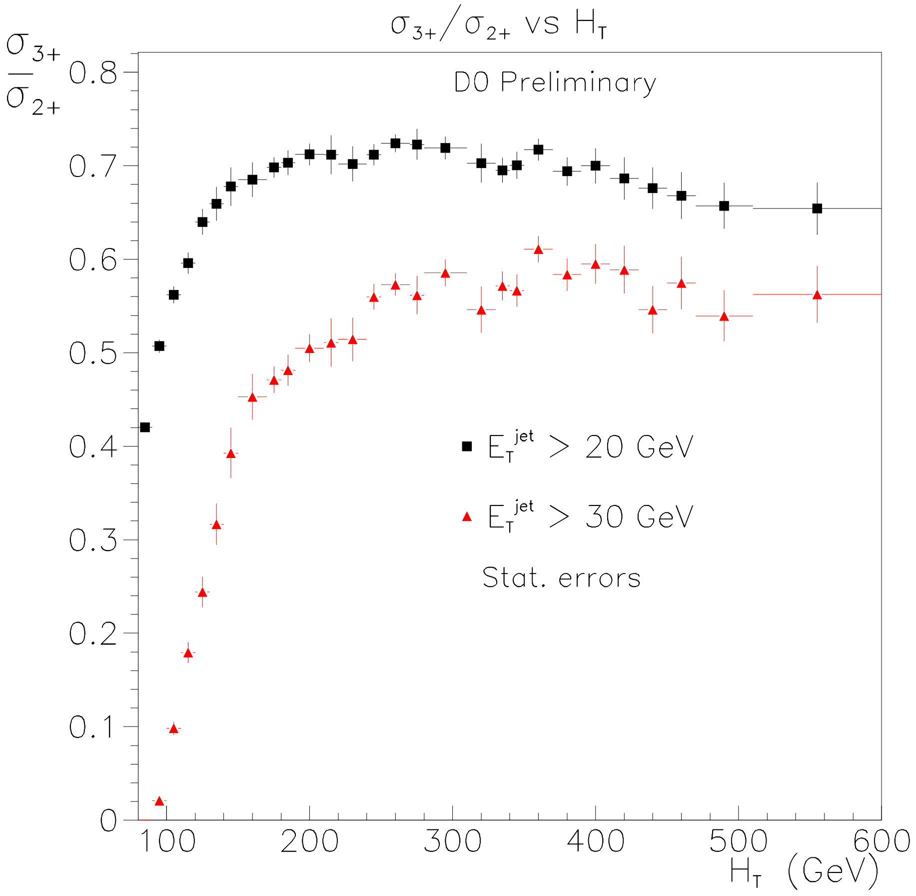

Figure 5.12: $\frac{\sigma_{3+}}{\sigma_{2+}}$ for two values of mininum jet E_T .

Chapter 6

Sources of Measurement Uncertainty

6.1 Introduction

In this chapter, I will list the uncertainties in the measurement of the cross section ratio. The systematic errors are due to the use of jet and event selection criteria, the possible mis-measurement of the interaction vertex, multiple-interaction events at high luminosities, and the jet energy scale correction.

6.2 Trigger efficiency correction

A correction for trigger inefficiency is applied to the data based on the measured event trigger efficiencies. The uncertainty in the ratio $\frac{\sigma_{3+}}{\sigma_{2+}}$ due to the trigger efficiency correction is about 3% at $H_T = 80$ GeV and quickly drops to zero beyond 150 GeV. The magnitude of this error depends on the jet E_T threshold used. The uncertainty is also 1-3% for jet thresholds of 25 GeV, while at 30 and 40 GeV the error is negligible. This trigger uncertainty is uncorrelated from point-to-point and is included in the total systematic error.

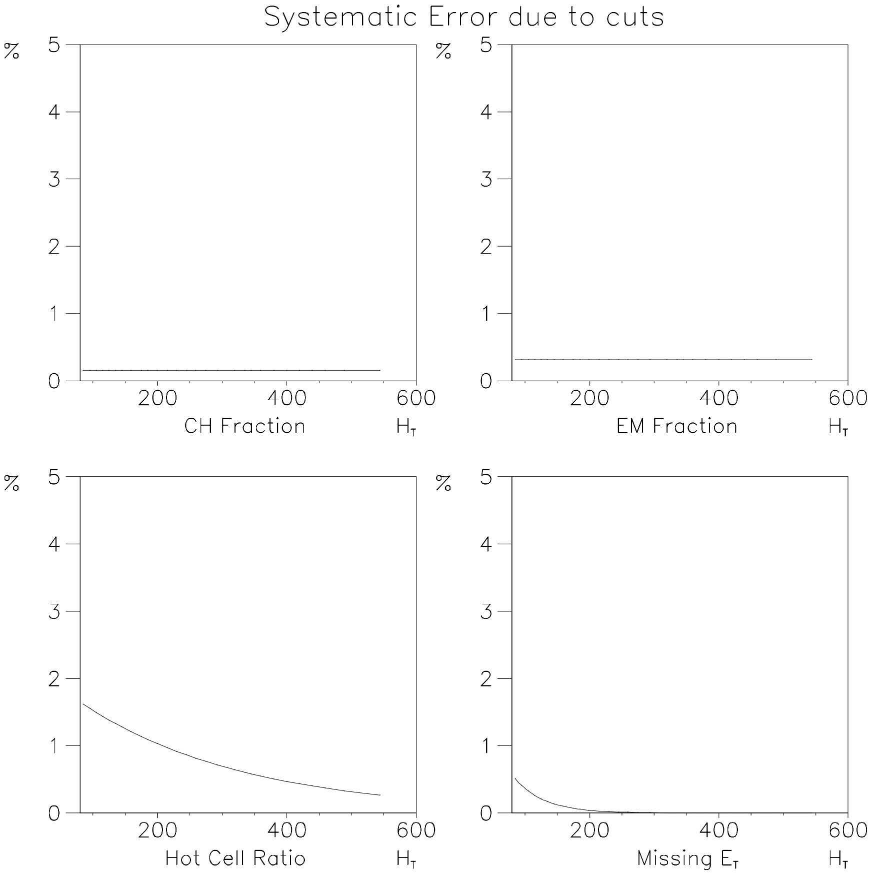

Figure 6.1: Systematic error due to event and jet selection criteria.

6.3 Jet and event selection criteria

The systematic error in the cross section ratio measurement due to event and jet selection criteria is estimated by comparing the measured ratio before and after the individual selection criteria are applied. The difference between the two measurements is a conservative estimate of the error. The percentage change in the ratio as a function of H_T from each of the selection criteria is shown in Figure 6.1 and listed in Table 6.1.

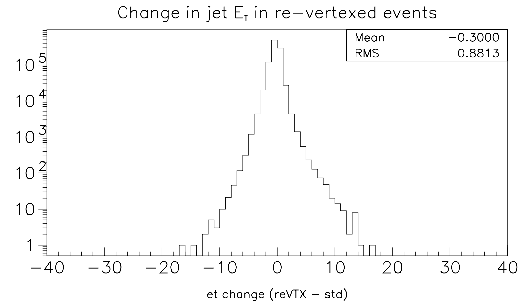

Figure 6.2: Change in jet E_T after re-vertexing. The difference is (re-vertex E_T - regular E_T). A jet's E_T can increase or decrease with re-vertexing, and the small negative mean shows that on average a jet's E_T will decrease with re-vertexing.

6.4 Vertex dependence

The interaction vertex for each event is determined by central drift chamber (CDC). The CDC measures tracks made by charged particles passing through it. The reconstructed tracks are extrapolated to the z-axis, resulting in one, two, or three groups of z-axis intercepts. The intercept value which has the largest number of tracks pointing to it is called the *primary vertex.* The others are called secondary, *etc.* vertices [33]. An accurate measurement of the interaction vertex is important because the transverse energy and pseudorapidity of a jet are calculated using the measured interaction vertex. If the wrong vertex is chosen as the primary vertex then the measurement of jet E_T and η and thereby H_T and $\frac{\sigma_{3+}}{\sigma_{2+}}$ are affected.

To estimate the effect of choosing the wrong vertex we calculate the vertex based on an estimate of the missing E_T ($\not{E}_T$). The $\not{E}_T$is calculated using both the primary and secondary vertices. The vertex which produces a smaller $\not{E}_T$is presumed to be the correct one. Using this new vertex, the jet E_T and pseudorapidities are recalculated. About 16% of events are "re-vertexed" in this manner. A characteristic of this re-vertexing is that jet E_T s are reduced a little on average. The distribution of jet E_T s in those events that were re-vertexed is shown in Figure 6.2. The change in the inclusive-two-jet and inclusive-three-jet H_T distribution is shown in Figure 6.3. The changes in the two-jet

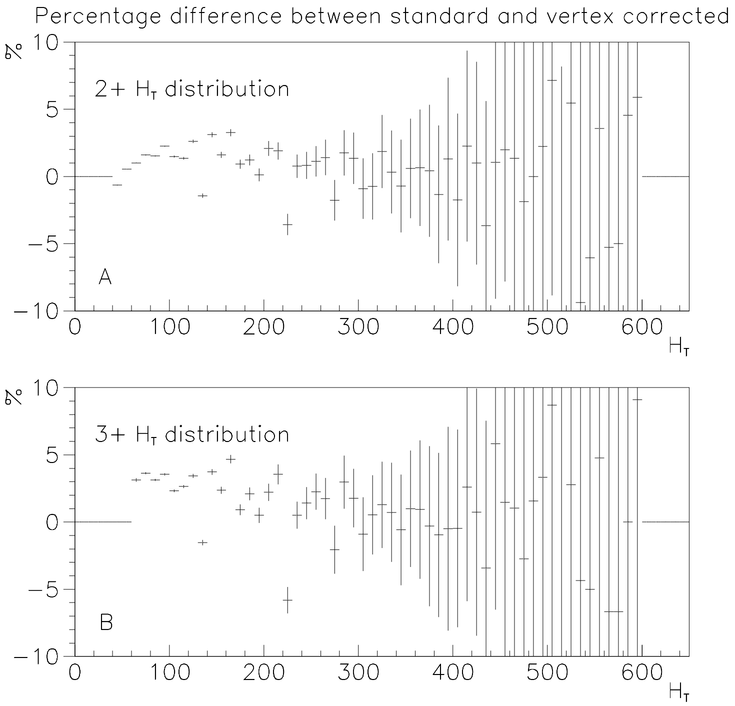

Figure 6.3: Change in two-jet inclusive (A) and three-jet inclusive (B) H_T from re-vertexing.

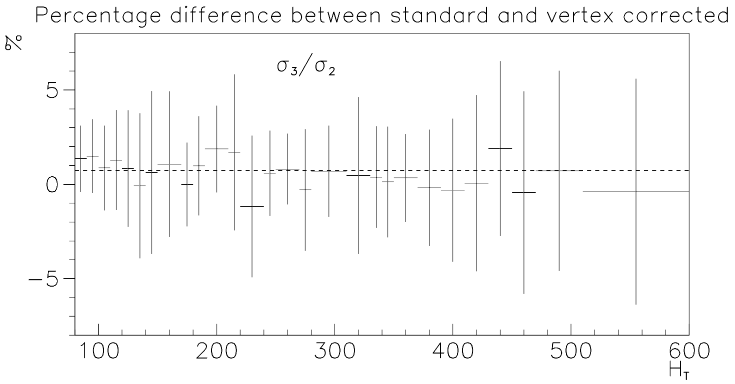

Figure 6.4: Change in $\frac{\sigma_{3+}}{\sigma_{2+}}$ from re-vertexing.

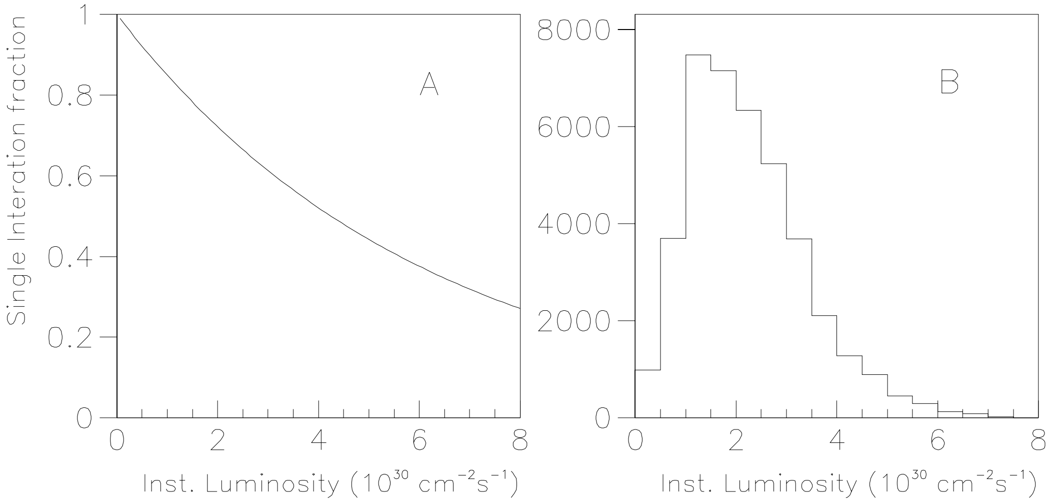

Figure 6.5: A. Single interaction fraction vs instantaneous luminosity. B. Instantaneous luminosity distribution.

inclusive H_T distribution and three-jet-inclusive H_T distribution cancel when the ratio is taken. Figure 6.4 shows the change in the cross section ratio following the re-vertexing correction. The error in the ratio $\frac{\sigma_{3+}}{\sigma_{2+}}$ is correlated from point to point and we therefore do not include it in the total systematic error.

6.5 Luminosity dependence

Events were recorded during widely-ranging luminosity conditions. The higher the luminosity the greater the average number of $p\overline{p}$ interactions per bunch crossing. That is, for any $p\overline{p}$ interaction (event) that triggers the first-level (Level 0) detectors, the chance of a second $p\overline{p}$ interaction in the same bunch crossing increases with the luminosity of the beam (Figure 6.5). The second interaction is typically a diffractive (glancing) interaction which results in the production of particles that deposit energy into the forward calorimeters (at large $|\eta|$) close to the beamline. These energy deposits typically do not cluster together and mimic jets, but the measurement of a jet from the primary hard interaction is contaminated by this energy deposited from the second interaction. This is partially corrected for in the latest version (V5.1) of the jet energy scale, described in Section 6.6 [34].

The result of mis-measured energy due to multiple interactions is a jet E_T (and hence event H_T) that is higher than the true E_T or H_T . This causes the $\frac{\sigma_{3+}}{\sigma_{2+}}$ vs H_T curve to fluctuate downward. Another effect of jet E_T s fluctuating upward is that jets that in reality have less than the 20 GeV minimum E_T requirement will then have a measured E_T greater than 20 GeV and will thus be counted as a jet. The result of this *threshold effect* is a change in the jet multiplicity which may change the cross section ratio measurement when the jet count change is from 2 to 3 jets.

To measure the luminosity dependence, we measured the cross section ratio as a function of instantaneous luminosity for several ranges in H_T . This range has to be chosen carefully because the cross section ratio increases rapidly with H_T at low H_T . Figure 6.6 shows the measurement of $\frac{\sigma_{3+}}{\sigma_{2+}}$ as a function of instantaneous luminosity for a number of bins in H_T . There is no consistent pattern of increase or decrease in the cross section ratio with the luminosity. To estimate an error, we fit a straight line through points and extrapolate the line to zero-luminosity. The difference between the zero luminosity value of $\frac{\sigma_{3+}}{\sigma_{2+}}$ and its value for all the luminosities is our estimate of the uncertainty due to luminosity, about 1%.

6.6 Jet energy scale

The DØ calorimeter is calibrated by measuring the response of calorimeter test modules to pion beams of known energy ("test beam data"). The gives us a set of calibration constants (relative sampling weights, conversion factors for ADC counts to GeV) that are used to convert the instrument signals to a value with dimensions of energy. The raw energy value is then further corrected for response, uranium noise, energy not coming from the hard interaction, and algorithm and calorimeter resolution effects [35].

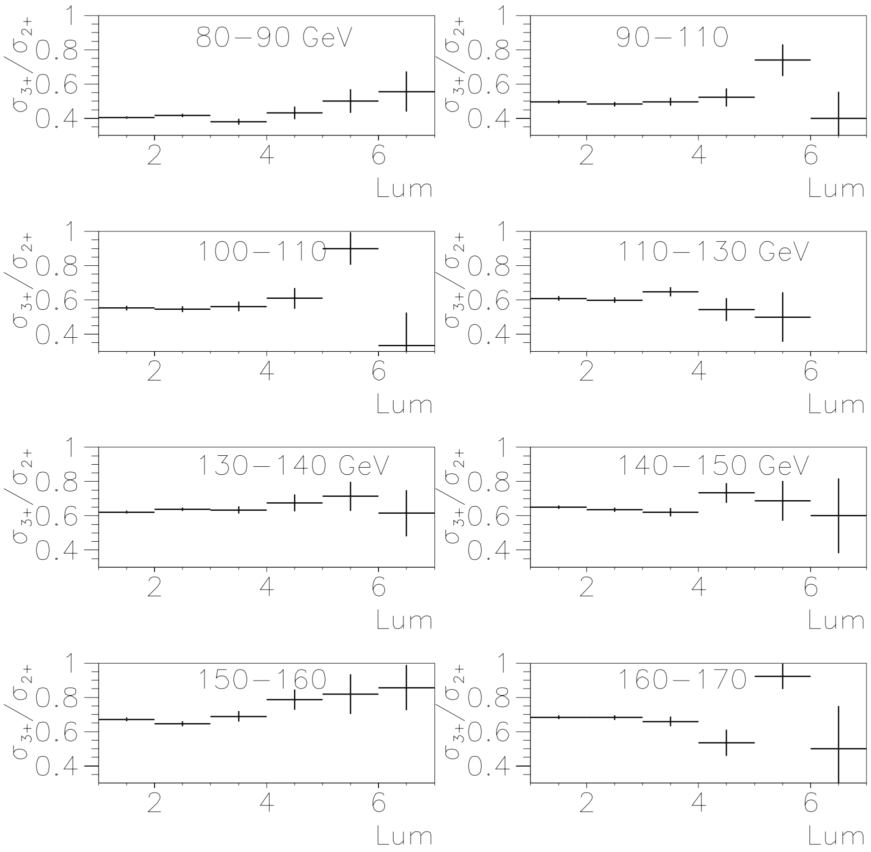

Figure 6.6: $\frac{\sigma_{3+}}{\sigma_{2+}}$ vs Instantaneous luminosity (in $10^{30}\mathrm{s}^{-1}\mathrm{cm}^{-2}$) for different H_T ranges.

The relation between the measured raw jet energy and the jet energy is given by the relation

$$E^{jet}_{particle} = \frac{E^{jet}_{meas} - O(\Delta R, \eta, \mathcal{L})}{R(\Delta R, \eta, E)\,[\,1 - S(\Delta R, \eta, E)\,]}$$

where O is an offset function of the cone size ΔR, the pseudorapidity η of the jet, and the instantaneous luminosity $\mathcal{L}$. This function accounts for uranium noise, “pileup” (distortion of calorimeter signal due to “out-of-time” signals caused by the memory of the electronics [36]) , and multiple interactions. It also takes into account energy

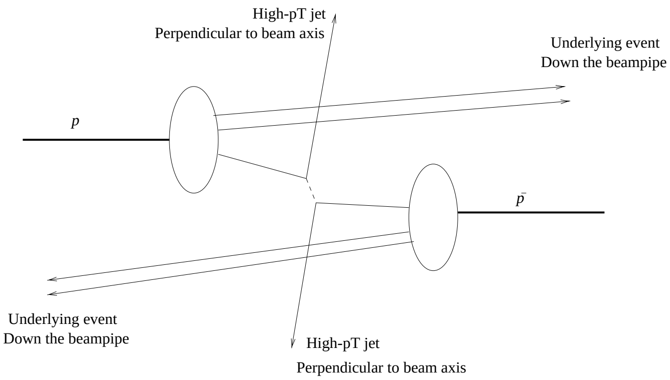

Figure 6.7: Underlying event

deposition from the *underlying event*, *i.e.,* interactions involving quarks from the proton and antiproton that do not undergo hard scattering (Figure 6.7).

R is the response function of the calorimeter to incident particles as a function of the particle energy. (Figure 6.8). This removes effects from jets that deposit energy into uninstrumented regions between calorimeter modules. It also corrects for an e/π ratio (a measure of the relative response of the detector to electrons and hadrons) which deviates from the ideal of unity. An e/π ratio of 1 is needed for a particle-independent correction. [37]. A flat response means that a calorimeter cell's output signal scales linearly with the energy of the incident particle. In Figure 6.8 this would correspond to a horizontal line. Response is determined by first measuring the electromagnetic (EM) scale using dielectron and diphoton decays of known particle resonances (Z, J/ψ, neutral pions). Then direct photon + jet events are used to relate the EM scale to the hadronic scale.

S is a measure of how much energy is "lost" and unmeasured due to being beyond the calorimeter jet algorithm cone ("out-of-cone showering"). In order for its energy to be measured, a jet has to interact with and deposit energy into the detector. In the process of interaction the particles that form a jet will produce a shower which may extend outside the jet algorithm cone of $R = \sqrt{\Delta\eta^2 + \Delta\phi^2} = 0.7$. This will result in an underestimate of the jet's energy. One method used to estimate the showering correction is to compare jets from a Monte Carlo event generator with test-beam data of jets.

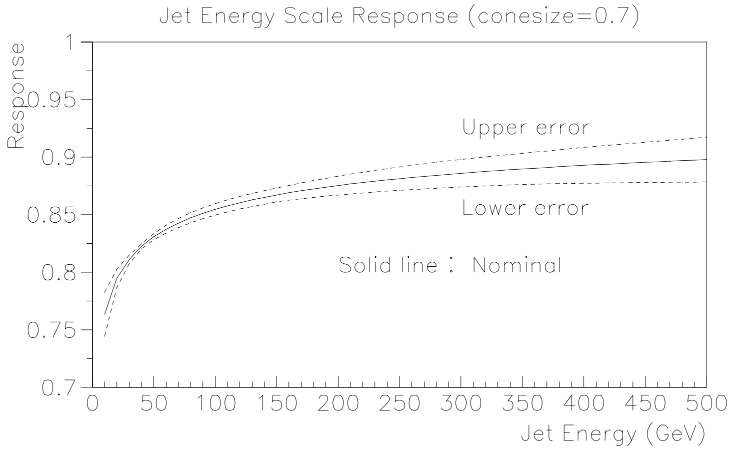

Figure 6.8: Jet energy scale response as a function of jet energy.

Our study of the energy scale error will concentrate on the response function R, the uncertainty of which reflects the combination of all these effects. The nominal response (solid curve) shown in Figure 6.8 is a fit to the "calorimeter response vs incident particle energy" measurements, while the upper and lower envelope is the maximum and minimum of all other possible fits. These upper and lower response curves are extremes of the energy scale. In addition, two alternate response curves (Figure 6.9) are also used which intersect each other. The curve labelled '1' has a lower-than-nominal response at low jet energy and a higher-than-nominal response at high jet energy. The second curve has the opposite behavior: high response at low energy and low response at high energy. Using these response curves we can check the effect of extreme variations in the energy scale on the measurement of $\frac{\sigma_{3+}}{\sigma_{2+}}$ vs H_T .

These response curves are used to scale the jet energy. The different measures of the cross section ratio from these five curves are used to estimate the overall energy scale error in $\frac{\sigma_{3+}}{\sigma_{2+}}$ as shown in Figure 6.11d. The decreasing error from 80-300 GeV is due to the upper and lower response curves, while the flat region above 300 GeV is due to the crossed response curves. The plot in Figure 6.10 shows $\frac{\sigma_{3+}}{\sigma_{2+}}$ vs H_T for the nominal, high, and low values of the energy scale correction and the percentage error determined by the

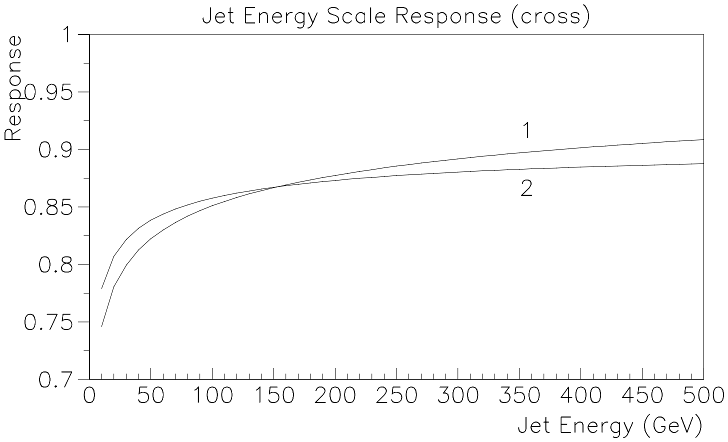

Figure 6.9: Jet energy scale response (crossed) as a function of jet energy.

fractional difference between nominal and high, and low and nominal. The uncertainty in the ratio $\frac{\sigma_{3+}}{\sigma_{2+}}$ due to the energy scale correction is estimated by comparing the ratio calculated from data corrected with the upper and lower response curves, as well as the crossed response curves, and comparing to a calculation using the nominal response curve. The error is set at 3%, correlated from one H_T bin to the next.

6.7 Error summary

6.7.1 Statistical errors

The measurement of the ratio $\frac{\sigma_{3+}}{\sigma_{2+}}$ involves a requirement on the jet multiplicity and a count of the number of events passing the multiplicity requirement. Thus, the statistical error on the ratio is given by the binomial formula. If the original sample has B events and the multiplicity requirement reduces that number to A then the statistical error is:

$$\text{error} = \frac{\sqrt{\mathrm{A}(1-\frac{\mathrm{A}}{\mathrm{B}})}}{\mathrm{B}} \quad \mathrm{A} < \mathrm{B}, \quad \mathrm{B} \neq 0$$

The H_T range is binned so that the statistical error is less than 10%.

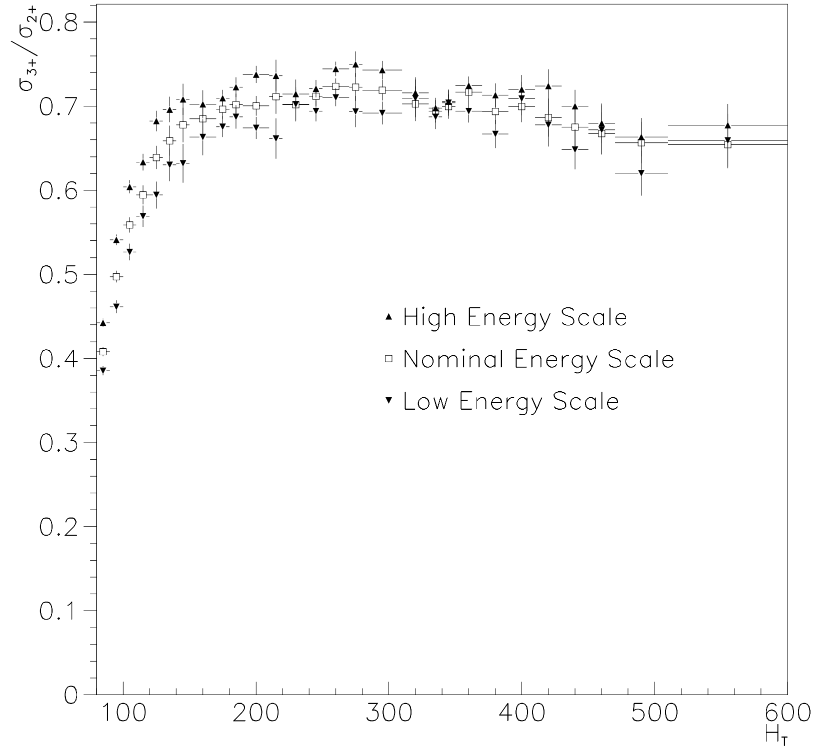

Figure 6.10: $\frac{\sigma_{3+}}{\sigma_{2+}}$ vs H_T for different energy scale choices.

Table 6.1: Errors due to different sources

Source	Error (percent)
Trigger	1-3 % H_T < 150 GeV
CH Fraction	0.2 %
EM Fraction	0.3 %
Hot Cell Ratio	1-1.5 %
Missing E_T	0.5 %
Mis-vertexing	0.7%
Luminosity	1%
Jet Energy Scale	3%
Total Systematic Error	3-4 %

6.7.2 Total systematic error

Uncertainty due to trigger, jet selection, and the statistical error are all point-to-point uncorrelated and added in quadrature. The energy scale error is correlated and is handled using a covariance matrix method (see Appendix B). The luminosity and mis-vertexing error are negligible and are not included. The uncertainties as a function of H_T are shown in Figure 6.11. The sum of all uncorrelated errors is shown in the lower right plot. The errors are listed in Table 6.1.

6.7.3 Correlated errors

In comparing our measured cross section ratio with theoretical predictions we wish to correctly include systematic errors that are point-to-point correlated, that is, the errors that shift all points in the same direction (up or down). Including these errors as uncorrelated would overestimate the agreement between data and theory. Figure 6.12 shows the cross section ratio with statistical and uncorrelated systematic errors (added in quadrature) on the points, while the magnitude of the correlated systematic errors is represented by a shaded band at the bottom of the plot.

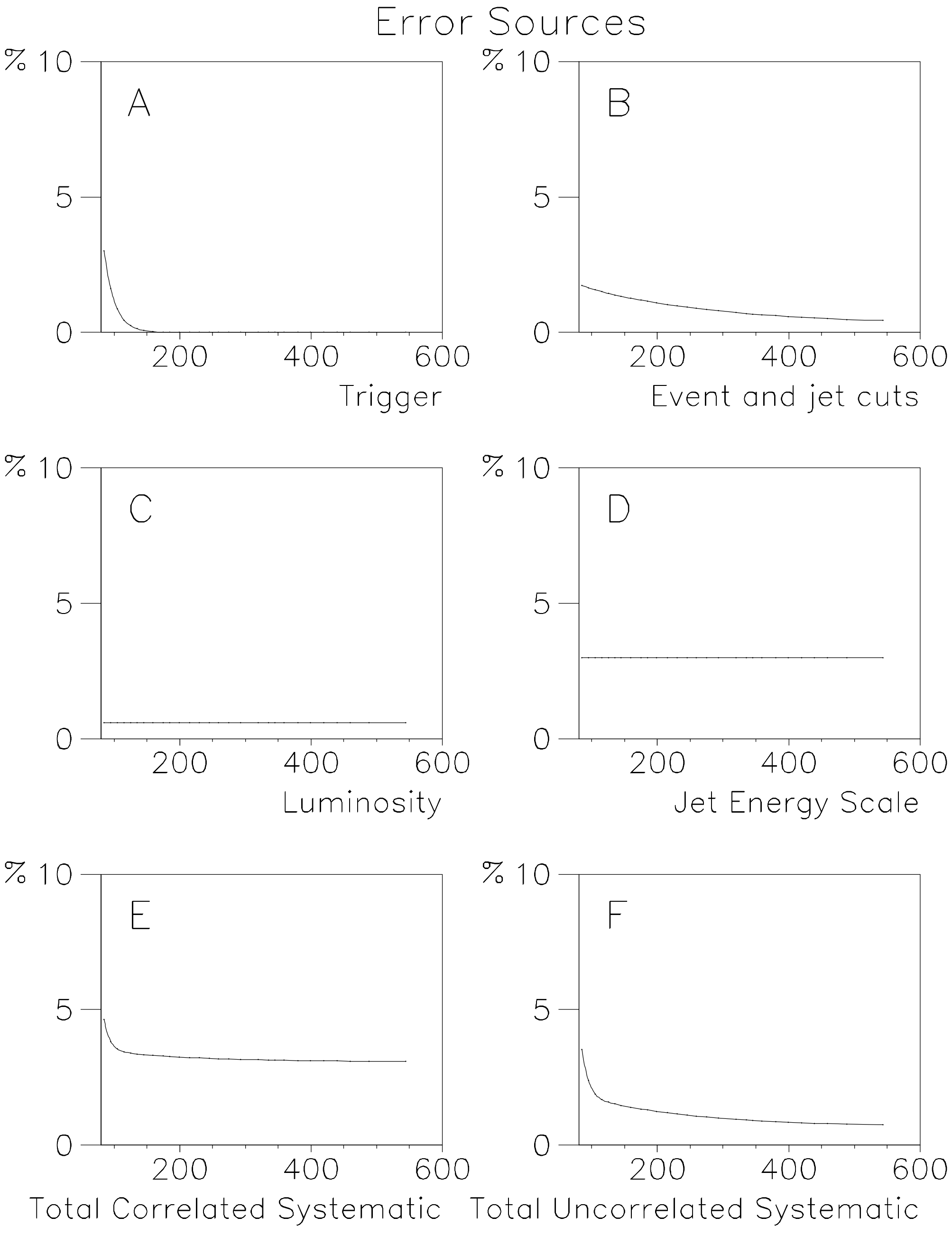

Figure 6.11: Systematic errors. The bottom two plots show the total correlated and uncorrelated errors.

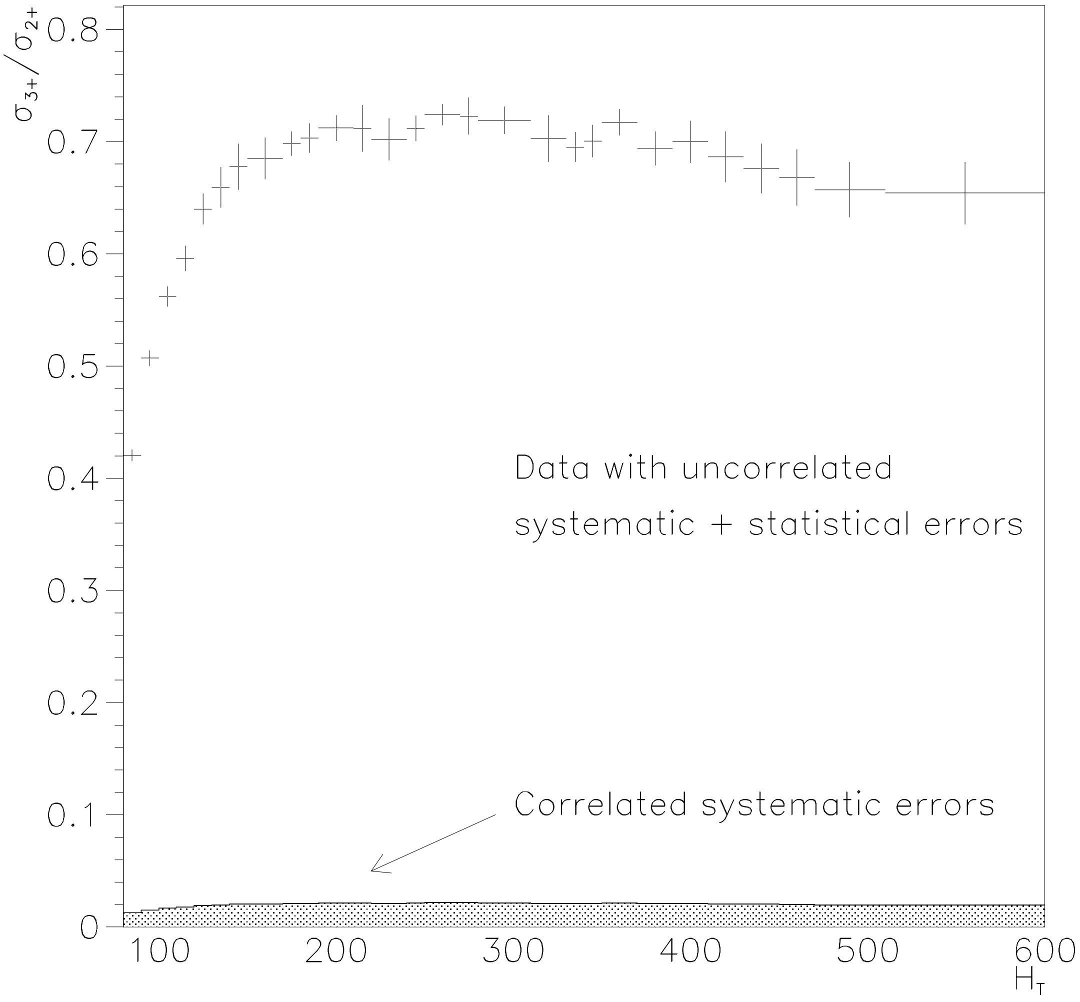

Figure 6.12: Cross section ratio showing statistical and systematic errors.

Chapter 7

Monte Carlo Simulations of QCD Processes

7.1 Introduction

The measurements of the ratio $\frac{\sigma_{3+}}{\sigma_{2+}}$ can be compared to theoretical calculations in the form of a Monte Carlo event generator. An event generator is a program that simulates a physical process . In our case, the process is the $p\bar{p}$ collision at Fermilab. The "inputs" to the event generator are the operating parameters such as total center-of-mass energy. The output is a set of events that are representative of events taken with a detector. This chapter will briefly discuss the Monte Carlo method as applied to a matrix-element cross section calculation program (JETRAD) and the modifications implemented to test the soft-jet renormalization scale prescription. We then present the results of the comparisons between the data and theory.

7.2 Monte Carlo prescription

A Monte Carlo method is a method for evaluating difficult integrals or of sampling probability distributions. The basic theorem of Monte Carlo integration is that the integral of a function f over a multidimensional volume V can be estimated by taking the arithmetic mean of the function f over many points N sampled from the volume V.

$$\int f dV \approx V\langle f\rangle \quad \text{with } \langle f\rangle \equiv \frac{1}{N}\sum_{i=1}^{N} f(x_i)$$

The points x_i are sampled from the volume V using a pseudo-random number generator.

7.3 JETRAD

JETRAD [38] is a next to leading order Monte Carlo event generator for inclusive 1 or 2-jet production for pp or $p\overline{p}$ collisions. One chooses the type of collision (here $p\overline{p}$), the center of mass energy, the number of jets to produce, the order in α_S of the perturbative calculation, the pseudorapidity range for final state partons, and the renormalization and factorization scale. In addition to calculating the total cross section for the interaction specified, it can also produce distributions of event variables. While the program only generates two- and three-jet events, the two-jet and three-jet cross sections are inclusive quantities, i.e., they are the cross section for two-or-more and three-or-more jets [39].

7.3.1 General approach

We begin with the factorization theorem of perturbative QCD

$$\sigma = \int dx_1 dx_2 d\Phi \frac{1}{2\hat{s}} f_{h\to i}(x_1) f_{h\to j}(x_2) \overline{\sum} |\mathcal{M}|^2$$

where dx_1 and dx_2 are the momentum fractions of the partons from the proton and antiproton, $d\Phi$ is the Lorentz-invariant phase space element, $\hat{s}$ is the flux factor for the partonic cross section, $f(x)$ are the parton distribution functions, and $\overline{\sum}|\mathcal{M}|^2$ is the squared matrix element for the partonic cross section, summed over final state colors and polarizations, averaged over initial colors and polarizations.

For n particles in the final state, the integration above is $(3n-2)$-dimensional. It is this integration that will be done via Monte Carlo. We first rewrite the differential element as

$$\frac{1}{2\hat{s}} dx_1 dx_2 d\Phi_n = J \prod_{i=1}^{3n-2} dr_i$$

where J is the Jacobian of the transformation. The Monte Carlo prescription then approximates the integral

$$\sigma = \int dr_1 \cdots dr_{3n-2} \; J \; f(x_1) f(x_2) \overline{\sum} |\mathcal{M}|^2$$

with the sum

$$\sigma \approx \frac{1}{N} \sum_{\{r_i\}} J f(x_1) f(x_2) \overline{\sum} |\mathcal{M}|^2$$

where $\{r_i\}$ are N sets of $3n-2$ random numbers [40]. In the case of the JETRAD event generator, the numerical integration routine used is VEGAS [41]. It supplies the $\{r_i\}$ random numbers and the "weight factor" $w = 1/N$. Once can produce arbitrary distributions $d\sigma/dz$ by filling a histogram of z with the weight

$$\frac{J f(x_1) f(x_2) \overline{\sum} |\mathcal{M}|^2}{N \Delta z}$$

where Δz is the width of the bins in z.

To produce a calculation of $\frac{\sigma_{3+}}{\sigma_{2+}}$ vs H_T , one produces two distributions $d\sigma_{3+}/dH_T$ and $d\sigma_{2+}/dH_T$ and divides the first by the second. A plot of this is shown in Figure 7.1.

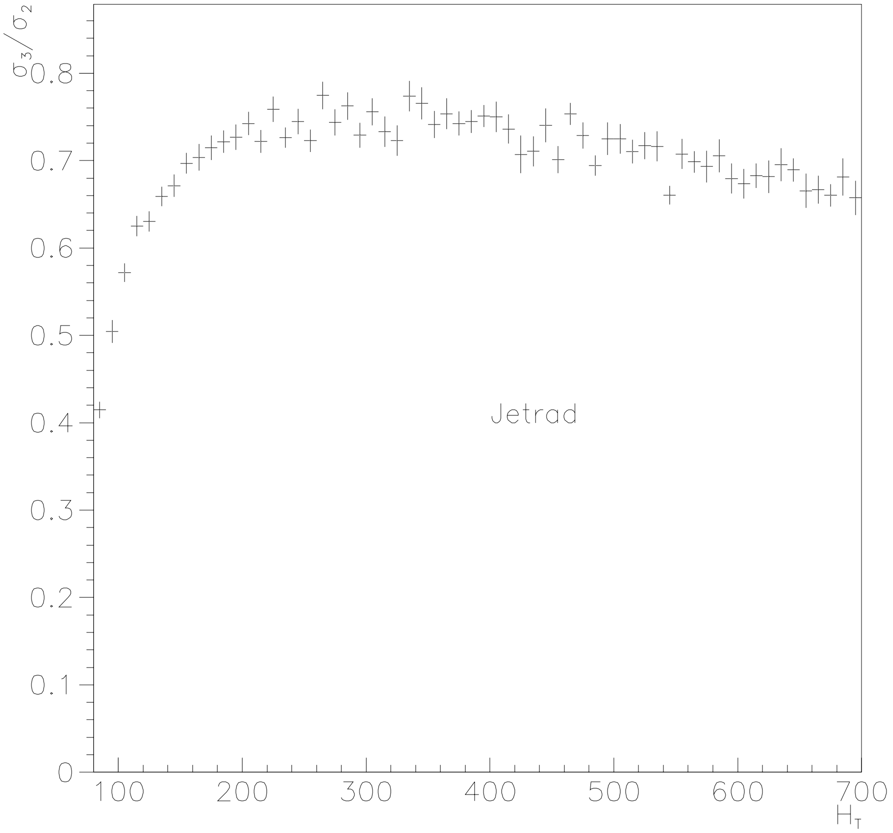

Figure 7.1: JETRAD calculation of $\frac{\sigma_{3+}}{\sigma_{2+}}$ vs H_T .

7.3.2 Input parameters and selection criteria

Introduction

The input parameters in JETRAD include the kinds of particles to be scattered (proton or antiproton), the center-of-mass energy of the collision, the number of loops in the calculation, the number of jets to produce (one, two, or three), the minimum and maximum E_T of the jets, the η ranges available for the jets, the "cone size" of the jet cone used in the jet-finding algorithm, the parton distribution function set to use, the renormalization scale (maximum jet E_T in the event or the sum of all jet E_T s in the event), and the number of events to generate. The factorization scale is set equal to the renormalization scale.

Cone size and R_{sep}

The jet-finding algorithm used in the Monte Carlo event generator approximates the algorithm used in the data reconstruction. The data jet algorithm searches for a jet by looking at the way energy is deposited into calorimeter cell towers. In JETRAD, the products of the interaction are two or three partons. In the data, reconstructed jets that are very close or overlapping are either combined or separated. A similar mechanism is used for the Monte Carlo jets, using the R_{sep} parameter. The R_{sep} is defined as the maximum angular distance, divided by the cone size, allowed between two partons to be merged into a single jet. R_{sep} is used to approximate the split-merge decision in the data version of the jet-finding algorithm. See Figure 7.2. To determine the proper value of R_{sep} for the data, the following method was used: Take a single jet from one event and place it (cell-by-cell) into an independent event. The second event was then re-reconstructed and the number of jets found is counted. Also, the distance (D) from the inserted jet to the closest jet in the independent event was calculated. The change in the number of jets found with D was then plotted (Figure 7.3) [25]. In the figure, the value of D where half of the events have two reconstructed jets is 0.85. This translates

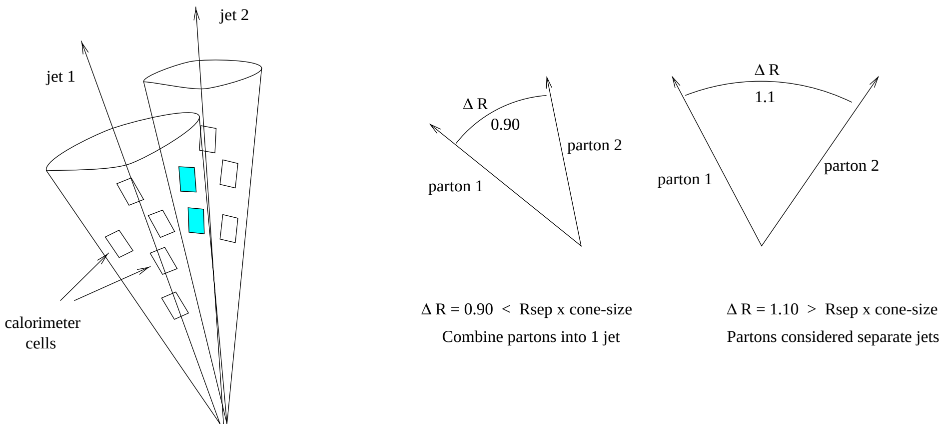

Figure 7.2: A. Splitting and merging of jets in the jet reconstruction algorithm. The shaded rectangles represent calorimeter cells that are shared by two jets before the split-merge criteria is applied. B. Use of R_{sep} in Monte Carlo jets. For a cone-size of 0.7 and an R_{sep} of 1.3, the critical distance for merging two partons into a jet is 0.91.

to a value of R_{sep} of $DR/\text{conesize} = 0.85/0.7 = 1.2$. An alternate method of measuring R_{sep} based on jet shape variables (e.g. the average fraction of calorimeter cell E_T in a subcone of a jet) gives a range for R_{sep} of 1.2 to 1.4. From these two methods an R_{sep} value of 1.3 was chosen. This value is used in the jet finding algorithm that is implemented in JETRAD. When two partons have an angular distance of $R_{sep}\times$cone-size $= 1.3\times 0.7 = 0.91$ the two partons are merged into one jet. The choice of R_{sep} affects the fraction of jets merged for certain critical values of D. To estimate the uncertainty due to the choice of R_{sep}, we take the width of the transition region in Figure 7.3 and use that as the range over which we vary R_{sep}. The D range is 0.8 to 0.933, which translates to 0.2 units in R_{sep}. Thus we vary our chosen R_{sep} of 1.3 by ±0.1 units. The change in the three-jet H_T distribution and in $\frac{\sigma_{3+}}{\sigma_{2+}}$ is the estimate of the uncertainty.

The value chosen for R_{sep} can affect the number of jets reconstructed in the Monte Carlo and hence the value of $\frac{\sigma_{3+}}{\sigma_{2+}}$. We compare the choice of $R_{sep} = 1.3$ (standard) to R_{sep} values of 1.2 and 1.4. This range corresponds to the region in Figure 7.3 where the number of jets is between one and two. We then compare the change in the three-jet H_T distribution and also in $\frac{\sigma_{3+}}{\sigma_{2+}}$ for both regular and smeared (Section 7.3.3) jets using

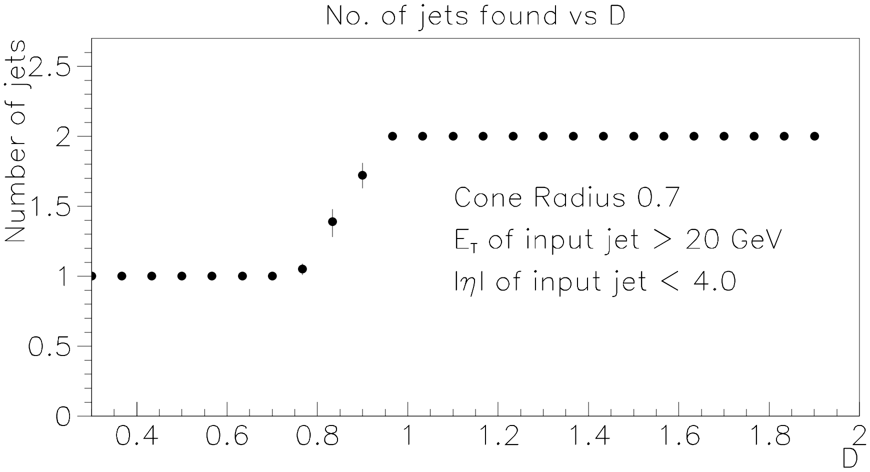

Figure 7.3: Difference in the number of reconstructed jets vs D for a cone of radius 0.7 The input jet has $E_T \geq 20$ GeV and $|\eta| \leq 4.0$.

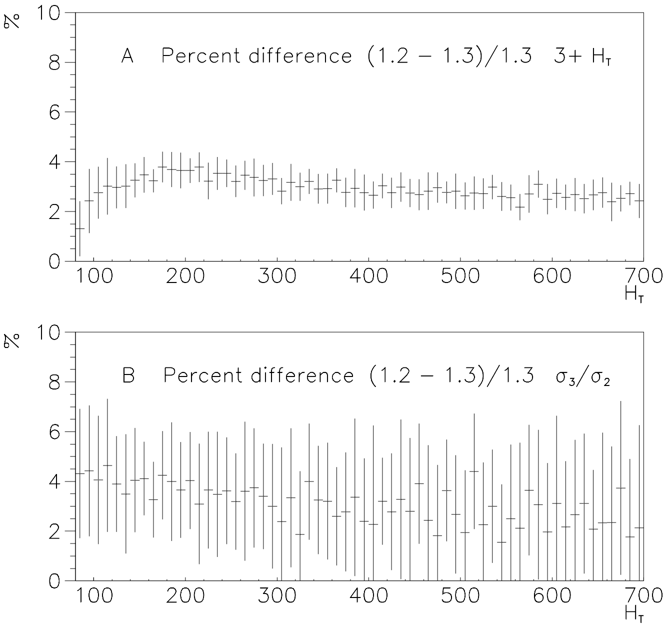

Figure 7.4: The fractional difference between R_{sep} =1.3 and 1.2 for the three-jet H_T distribution (A) and the ratio $\frac{\sigma_{3+}}{\sigma_{2+}}$ (B).

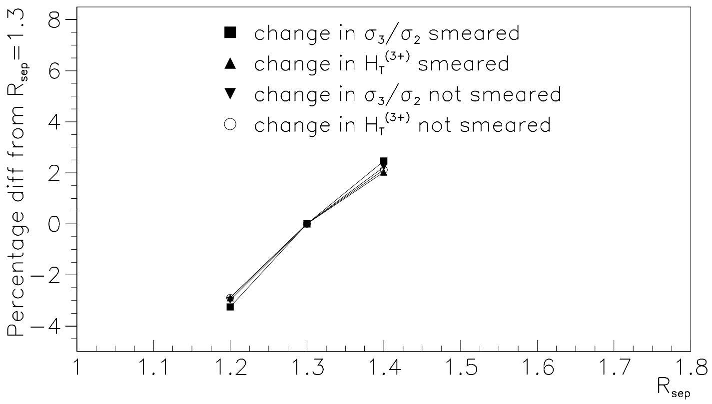

Figure 7.5: The percentage change in H_T and $\frac{\sigma_{3+}}{\sigma_{2+}}$ as we increase or decrease R_{sep} . A smaller R_{sep} will cause less merging of partons and thus more jets. A larger R_{sep} will produce more merging and less jets.

all three values of R_{sep} . Figure 7.4 shows the change in the 3-jet H_T distribution and the cross section ratio between an R_{sep} of 1.3 and 1.2. (The difference with R_{sep} =1.4 is similar in shape and magnitude.)

The percentage difference varies slightly with H_T but is more or less constant at around 3%. The plot in Figure 7.5 shows the percentage change in three-jet H_T and $\frac{\sigma_{3+}}{\sigma_{2+}}$ as we move away from an R_{sep} of 1.3 in either direction. By definition the change at 1.3

is zero. Both the three-jet H_T distribution change and the cross section ratio change have the same R_{sep} sensitivity. The sensitivity of the theoretical cross section ratio to the choice of R_{sep} is around 3%.

Parton distribution

It is predicted that since we are measuring a ratio of cross sections, the effect of using different parton distribution functions is minimal. This was studied empirically using two different parton distribution sets CTEQ4M and MRSD0′. The cross section ratio

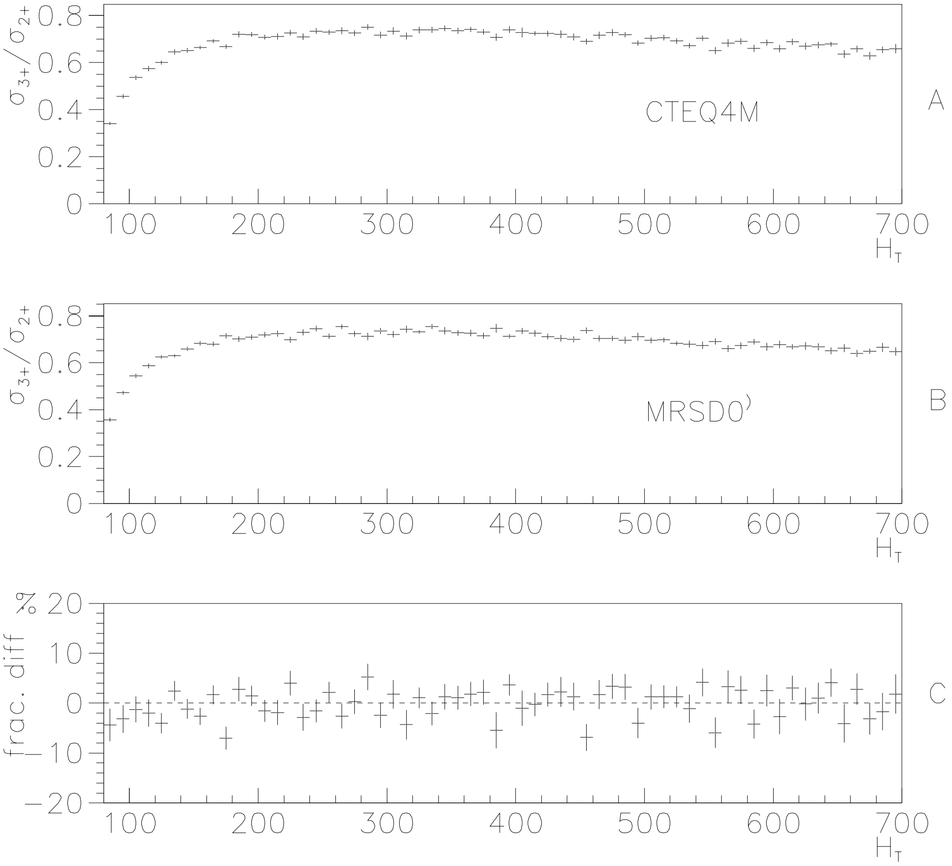

Figure 7.6: $\frac{\sigma_{3+}}{\sigma_{2+}}$ from JETRAD using *A*) CTEQ4M and *B*) MRSD0′ parton distribution functions. *C*) shows the percentage difference, which fluctuates about zero.

$\frac{\sigma_{3+}}{\sigma_{2+}}$ calculated with each of these parton distribution sets is shown in Figure 7.6. The difference between the two parton distributions sets is negligible.

7.3.3 Sources of theoretical uncertainty

Jet E_T resolution

The jet E_T resolution was studied with events containing two back-to-back jets, using momentum conservation in the transverse plane defined by the two jets [42] [43]. The calorimeter resolution for measuring jets was modeled after the *single particle* resolution, *i.e.*, the calorimeter resolution for measuring single incident particles. The single particle calorimeter resolution is parametrized as

$$\left(\frac{\sigma_{E_T}}{E_T}\right)^2 = C^2 + S^2/E_T + N^2/{E_T}^2$$

The C is an constant offset, the S^2/E_T term is from contributions from sampling fluctuations and the nature of the incident particle, and lastly the $N^2/{E_T}^2$ term is due to noise fluctuations affecting the high energy regime [43].

The measured resolutions are shown in Figure 7.7 for various jet η regions. The measurement of jet E_T generally improves as both E_T and η increases. In order to compare the data to the Monte Carlo prediction, Monte Carlo jets are "smeared" using the measured jet resolutions. The smearing involves adding or subtracting a random fraction of the jet's resolution uncertainty to the Monte Carlo jet E_T using the resolution parametrizations. This changes the characteristic of the sample of Monte Carlo jets to model the jets measured by the calorimeter.

The result of smearing the Monte Carlo jet E_T s should not change the shape of the jet pseudorapidity distribution (Figure 7.8). We compare the jet η distribution with and without smearing, and find that the fractional percentage difference between the smeared and raw η distribution fluctuates about zero in the central region (η between -1 and $+1$) and increases to about 10% at η of 3.5 as shown in Figure 7.9.

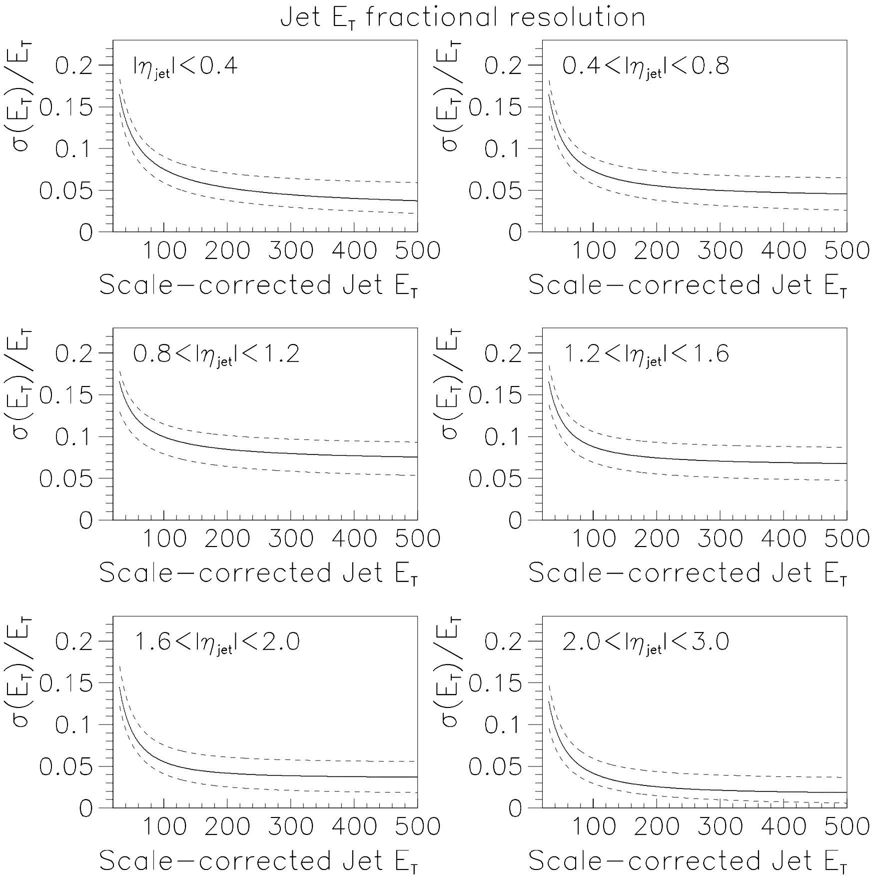

Figure 7.7: Run 1a jet E_T fractional resolution. Dashed lines represent the upper and lower error estimates on the fractional resolution.

The change in shape at high η is accounted for by the tendency of high-η jets to have a lower average jet E_T , as shown in Figure 7.10. The curved line shows the limit for jets produced from 1800 GeV proton-antiproton collisions. There can be no jet with an E_T above the curve for such large jet η s. The low-E_T , high-η jets are then smeared with a larger uncertainty value than central ($0.8 < |\eta| < 1.6$) jets.

We apply the smearing to the Monte Carlo jets, measure the ratio $\frac{\sigma_{3+}}{\sigma_{2+}}$ and compare to a sample that was not smeared. Figure 7.11 shows the change in the ratio when the smearing is applied. The smearing is found to affect the shape of the ratio mostly

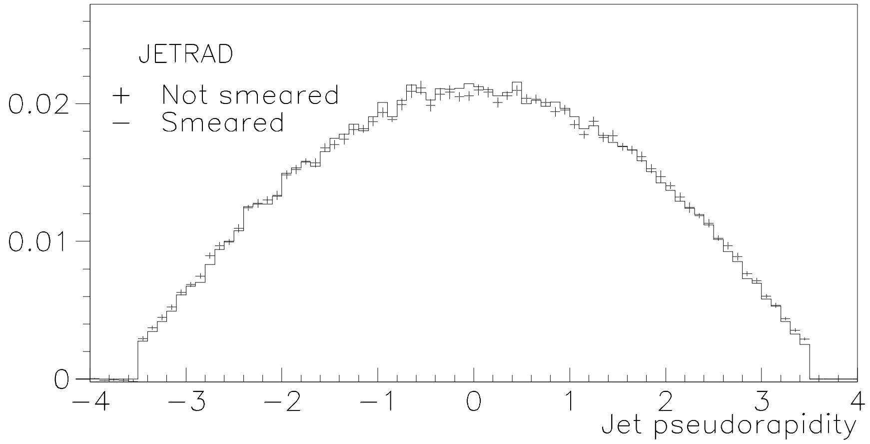

Figure 7.8: Jet pseudorapidity (η) distribution for JETRAD Monte Carlo jets. The histograms are normalized to the same area.

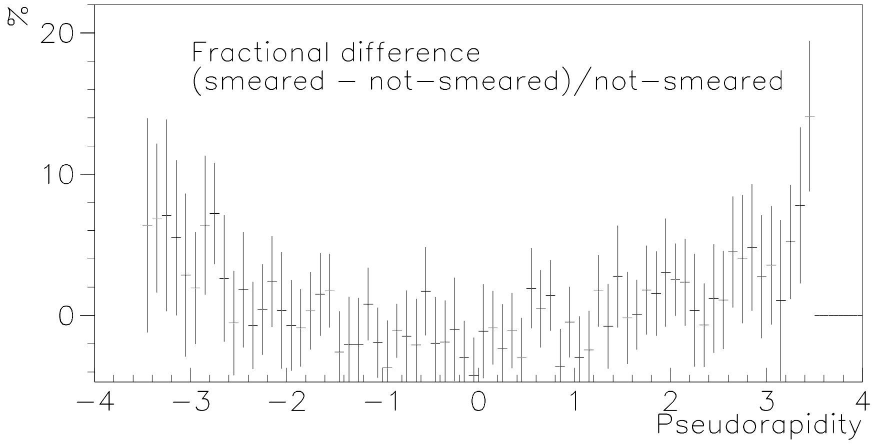

Figure 7.9: Fractional percentage difference between smeared and raw jet pseudorapidity distributions.

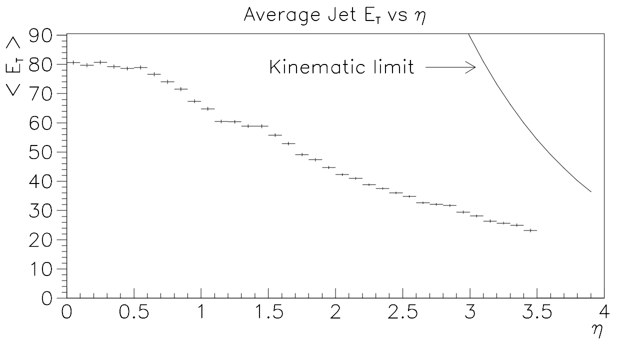

Figure 7.10: Average jet E_T vs jet pseudorapidity (η). The curve shows the kinematic limit for jets from 1800 GeV collisions. The small rise in the average E_T in the $\eta = 1.4$ region is due to different calorimeter sampling weights in that pseudorapidity region.

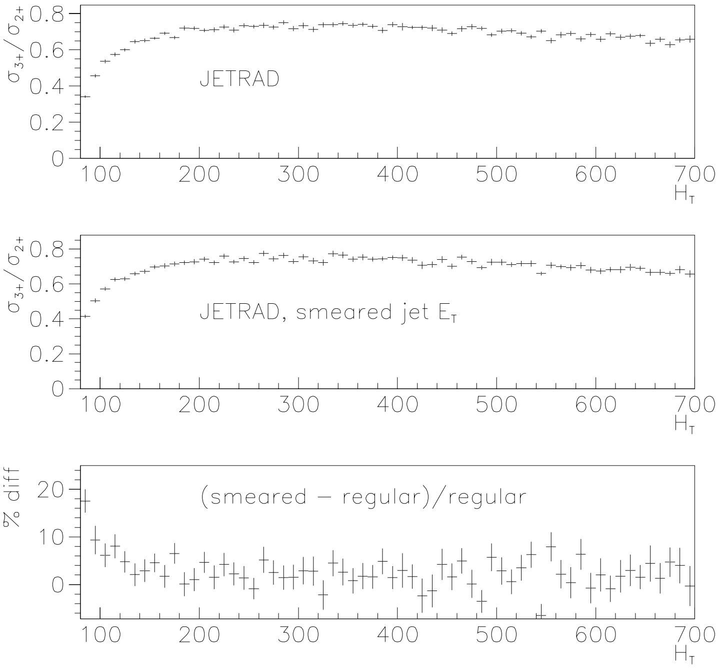

Figure 7.11: Comparison of the ratio $\frac{\sigma_{3+}}{\sigma_{2+}}$ calculated with JETRAD, with and without the smearing of jet E_T. The bottom plot shows the percentage difference between the two.

at the low-H_T region. The smeared-jet $\frac{\sigma_{3+}}{\sigma_{2+}}$ has a higher value than the measurement without smearing. This is due to the nature of the jet E_T spectrum: the steeply falling distribution causes jets to "smear high" (smeared E_T larger than original E_T) more often than it "smears low". This promotes jets whose E_T is just below the threshold to above the threshold, thus increasing the jet multiplicity. This results in a higher measured cross section ratio.

The measured resolutions shown in Figure 7.7 include an uncertainty envelope indicated by the dotted lines. We use this resolution uncertainty to estimate the uncertainty in $\frac{\sigma_{3+}}{\sigma_{2+}}$ due to the application of the smearing procedure. The method is as follows: each fractional resolution σ_{E_T}/E_T vs E_T is accompanied by two other curves (dashed). We call these the "Hi-smear" and "Lo-smear" resolution curves. We use each of the Hi- and Lo-smear curves to smear the Monte Carlo jets and compare to the smearing with the nominal curve. The fractional difference in the ratio $\frac{\sigma_{3+}}{\sigma_{2+}}$ between the nominal, Hi and Lo smear is shown in Figure 7.12. We estimate the uncertainty in the ratio $\frac{\sigma_{3+}}{\sigma_{2+}}$ due to

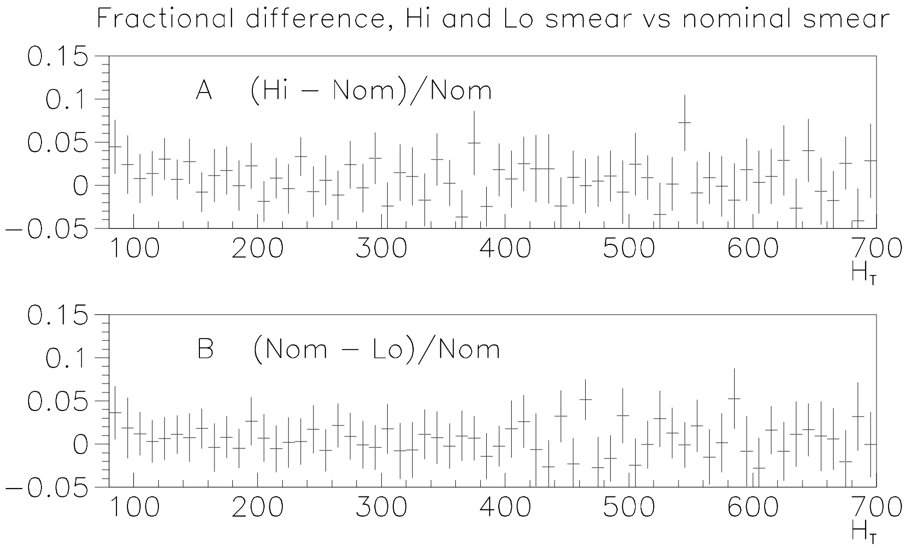

Figure 7.12: The fractional difference between the nominal smear and the Hi and Lo smearing.

the smearing procedure to be 2% constant in H_T . This is taken to be correlated from one H_T bin to the next.

Jet-finding efficiency

The jet reconstruction algorithm in RECO has an efficiency for finding jets as well as an efficiency for reconstructing the jet's correct energy. Any inefficiency which results in RECO calculating the wrong energy of a jet is corrected for in the jet energy scale. There is, however, the possibility of RECO not reconstructing a jet at all (missing a jet altogether). This has been studied [44] [45] using photon+jet events. The data set used consists of single-photon events where a balancing jet is presumed to have been missed by the jet reconstruction algorithm. The result of the study is a set of efficiency curves for different η regions. In each η region, the efficiency for RECO to find (or not miss) a jet is given as a function of jet E_T , as shown in Figure 7.13. Jet-finding efficiency is always greater than 95% for E_T above 20 GeV and rises quickly to 100% above 25 GeV.

Using this information, we can either correct the data and scale up the jet count for some events, or correct the Monte Carlo and scale down the jet count appropriately. We choose the latter method, randomly dropping jets in the Monte Carlo based on the jet-finding efficiency of Figure 7.13 to simulate the mis-reconstruction of jets in the data. The change in the cross section ratio as a result of applying this efficiency is shown in Figure 7.14. Since this correction is so small it is not included in the final results.

Total error

The systematic error due to jets not reconstructed and jet resolution is added to the statistical error in quadrature. This is shown in Figure 7.15. The total error is between 2 and 2.5% .

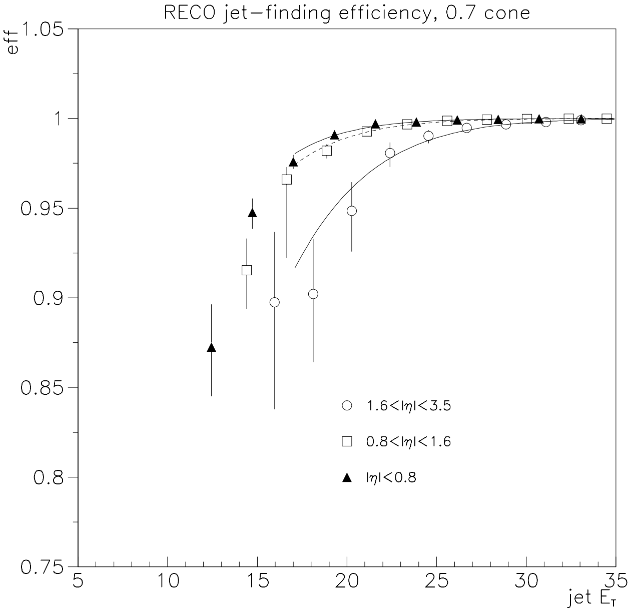

Figure 7.13: Jet-finding efficiency in different pseudorapidity regions as a function of jet E_T .

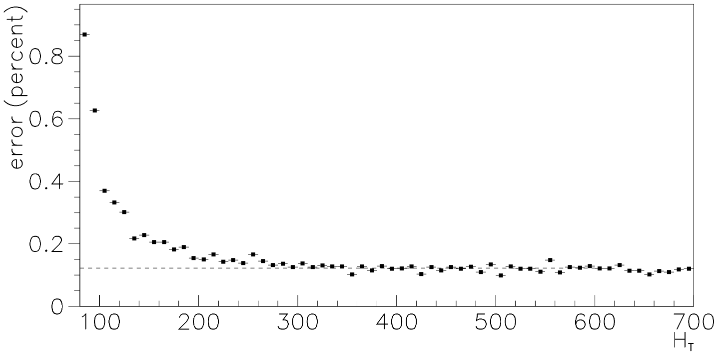

Figure 7.14: Percentage error in $\frac{\sigma_{3+}}{\sigma_{2+}}$ as a function of H_T due to jets not reconstructed.

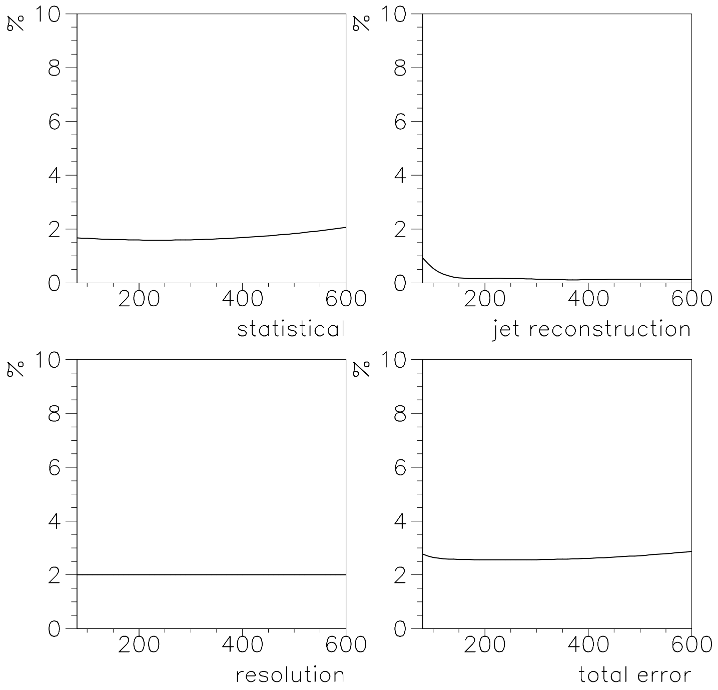

Figure 7.15: Errors in the theoretical prediction. The horizontal axis is H_T .

7.3.4 Renormalization scale of third-jet production

In calculating a cross section for a process, one first chooses a renormalization scale μ_R. The Standard Model does not give a prescription for choosing this scale. It is typically chosen to be of the order of the transverse energies of the jets produced. The renormalization scale μ_R is a parameter in the approximation of α_S .

$$\alpha_S = \frac{\alpha_S(\mu_0^2)}{1 + (\beta_1/4\pi)\alpha_S(\mu_0^2)\ln(\mu^2/\mu_0^2)} \qquad \text{(lowest order)}$$

where $\alpha_S(\mu_0^2)$ is a boundary condition for the differential equation whose solution is α_S above. β_1 is $11 - 2n_f/3$ with n_f quark flavors.

In the current version of JETRAD the same renormalization scale is used in evaluating α_S for both the hard scatter and also the gluon emission leading to a third jet.

The choice for this scale is typically a factor times H_T ($= \sum E_T$). We are interested in testing whether a different renormalization scale for the third jet production is more consistent with experimental findings than is the use of one renormalization scale for all instances of α_S .

The two different theoretical parametrizations are shown in Table 7.3.4. In the first instance $\mu_R^{(3)} \approx H_T$, *i.e.* the renormalization scale for both the hard scatter and third-jet emission is the same. This is the standard JETRAD prescription. In the second case $\mu_R^{(3)} \approx E_T^{(3)}$, *i.e.* the third-jet scale is effectively changed to the value of the E_T of the third jet (when there is a third jet). This is done by scaling the cross section by a factor

$$\frac{\alpha_S(\mu_R = E_T^{(3)})}{\alpha_S(\mu_R = \frac{1}{4}H_T\ )}$$

where $\mu_R = E_T^{(3)}$ is a renormalization scale on the order of the transverse energy of the third jet [46]. The difference between the two theories above is in the third jet. We calculate $\frac{\sigma_{3+}}{\sigma_{2+}}$ *vs.*H_T with both choices of soft-jet renormalization scales and compare to data. Figure 7.16 shows the theory calculation using two different renormalization scales for the third jet emission. In order to compare the relative magnitudes of the third jet E_T with H_T the average E_T of the third jet is plotted as a function of H_T (Figure 7.17).

Table 7.1: The scales for the hard scatter and third jet emission for two JETRAD settings.

Theory	Hard Scatter Scale	Third jet scale
$\mu_R^{(3)} \approx H_T$	$\mu_R = \frac{1}{4}H_T$	$\mu_R^{(3)} = \frac{1}{4}H_T$
$\mu_R^{(3)} \approx E_T^{(3)}$	$\mu_R = \frac{1}{4}H_T$	$\mu_R^{(3)} = E_T^{(3)}$

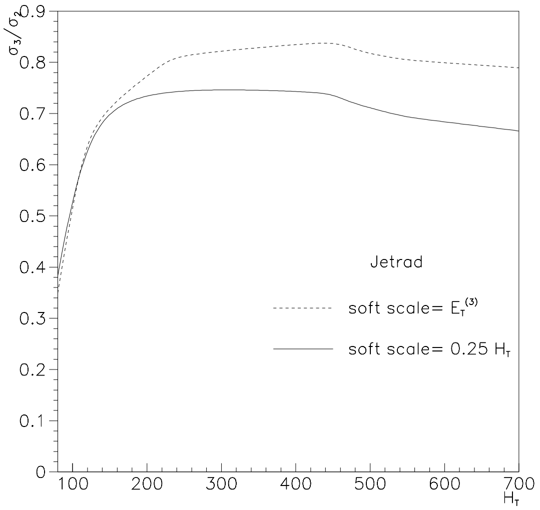

Figure 7.16: JETRAD calculation of $\frac{\sigma_{3+}}{\sigma_{2+}}$ using two different renormalization scales for soft jet emission.

7.4 Comparison of data with QCD

7.4.1 Introduction

In the next sections we compare the two renormalization scale prescriptions to the data to determine whether one offers a more consistent description of the measurement than the other. The two theory candidates being compared differ only in the choice of the

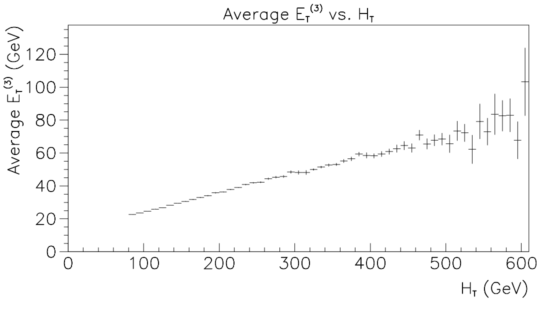

Figure 7.17: The average value of the third jet E_T as a function of the H_T of an event.

renormalization scale for the third jet ($\mu_R^{(3)}$). The choices are $\mu_R^{(3)} = \frac{1}{4}H_T$ and $\mu_R^{(3)} = E_T^{(3)}$. In order to compare the data to the theory, the latter is rebinned to match the binning of the data. The χ^2 for the data-theory comparison is given by:

$$\chi^2 = \sum_{H_T \text{ bins } i\ j} (D_i - T_i)\frac{1}{C_{ij}}(D_j - T_j)$$

where D_i is the value of $\frac{\sigma_{3+}}{\sigma_{2+}}$ in the ith H_T bin for data and T_i is for the JETRAD (Theory), and C_{ij} is the *covariance matrix* containing all the data and theory uncertainties as well as correlations between one H_T bin and another. (See Appendix B for an example.) A χ^2 per degree of freedom (or *reduced* χ^2, $\tilde{\chi}^2$) of about 1 indicates good agreement between the data and theory. Comparing the $\mu_R^{(3)} \approx H_T$ case and $\mu_R^{(3)} \approx E_T^{(3)}$ theory curves to the data we have the result shown in Figure 7.18. Between the two theories, the $\mu_R^{(3)} \approx H_T$ set is a better fit to the data, with a $\tilde{\chi}^2$ of 1.02 vs 6.8 for $\mu_R^{(3)} \approx E_T^{(3)}$.

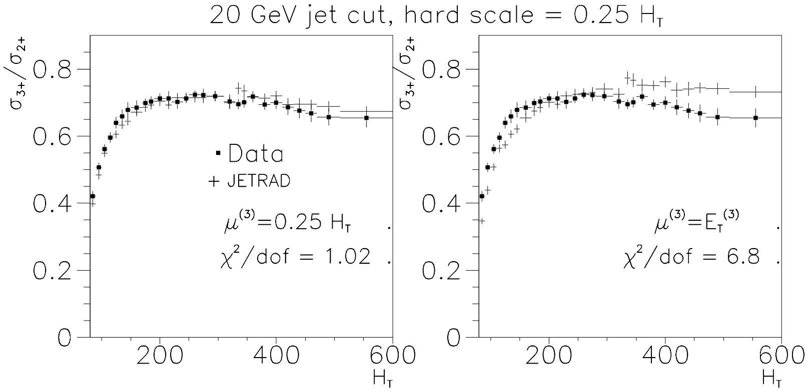

Figure 7.18: A χ^2 comparison of data with two theory prescriptions.

Variation with the hard scale

The hard scale chosen in the comparisons of the previous section was $\mu = \frac{1}{4}H_T$. The $\frac{1}{4}$ factor is an arbitrary value but has shown to be in agreement with other DØ

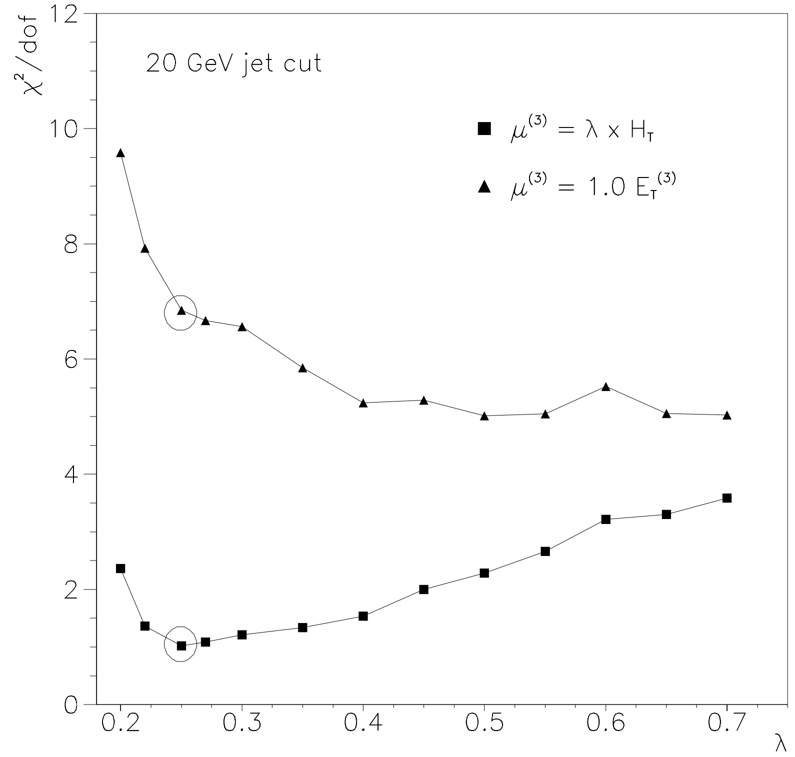

Figure 7.19: χ^2 difference between data and theory for different hard scales. The points from the initial $\mu = \frac{1}{4}H_T$ comparison are circled.

analyses which use JETRAD as the theory prediction, such as the single-inclusive jet E_T measurement. We have looked at the χ^2 difference between data and theory for hard scales other than $\frac{1}{4}H_T$. Other factors we investigated are 0.2, 0.27, 0.3, 0.35, 0.4, 0.45, and 0.5. We will use the variable λ to denote the factor of H_T used as the scale for the hard scatter. The change in $\tilde{\chi}^2$ as we increase and decrease λ from 0.25 is shown in Figure 7.19. The initial $\frac{1}{4}$ factor result is marked with a circle in the plot. As seen in the figure, when varying λ up and down the initial $\frac{1}{4}$ value, the $\tilde{\chi}^2$ for $\mu_R^{(3)} \approx E_T^{(3)}$ decreases with λ while for $\mu_R^{(3)} \approx H_T$ the trend is a slow rise with λ. The $\tilde{\chi}^2$ has a minimum at $\lambda = 0.25$.

Variation with the soft scale

The choice of $E_T^{(3)}$ as the soft scale is also somewhat arbitrary. To examine the other possibilities we tried $1.5 \times E_T^{(3)}$ and $2.0 \times E_T^{(3)}$. Changing the coefficient of the third-jet E_T from 1.0 to 2.0 changes mostly the normalization of the cross section ratio, with a small change in the shape, as shown in Figure 7.20. We compare each of the three soft scale choices with the data and calculate a $\tilde{\chi}^2$ as before. The results are shown in Figure 7.21. Varying the factor of $E_T^{(3)}$ for the third jet scale does not appreciably change

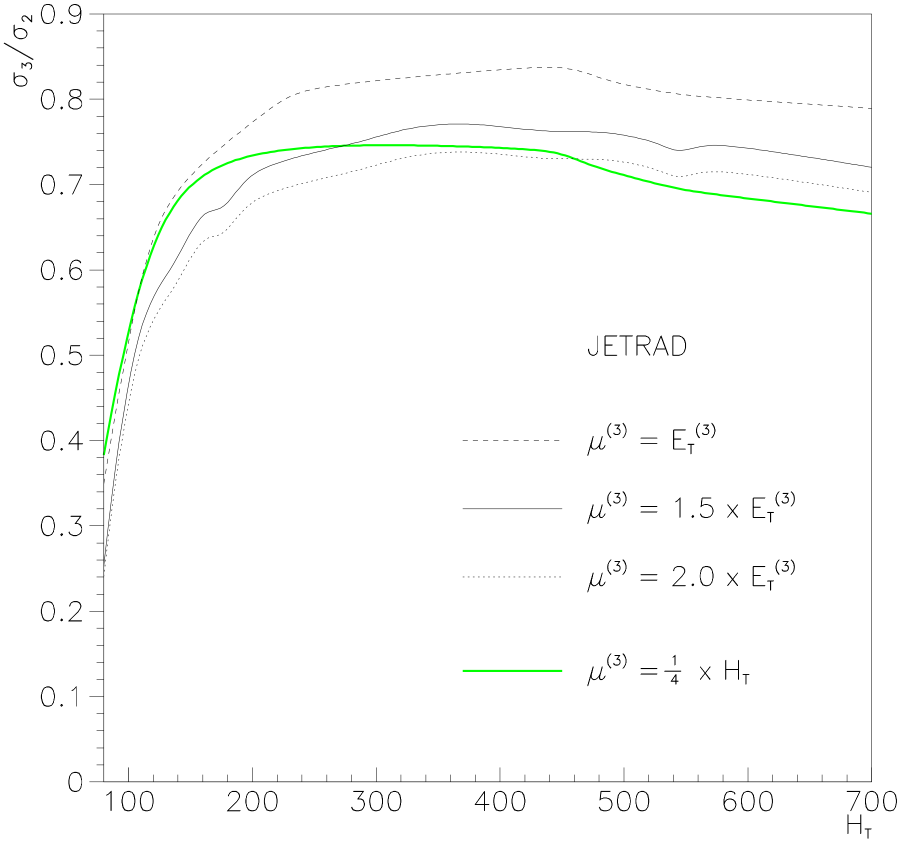

Figure 7.20: The cross section ratio for three different soft-scale choices. The thick shaded line is the cross section ratio using H_T as the soft scale.

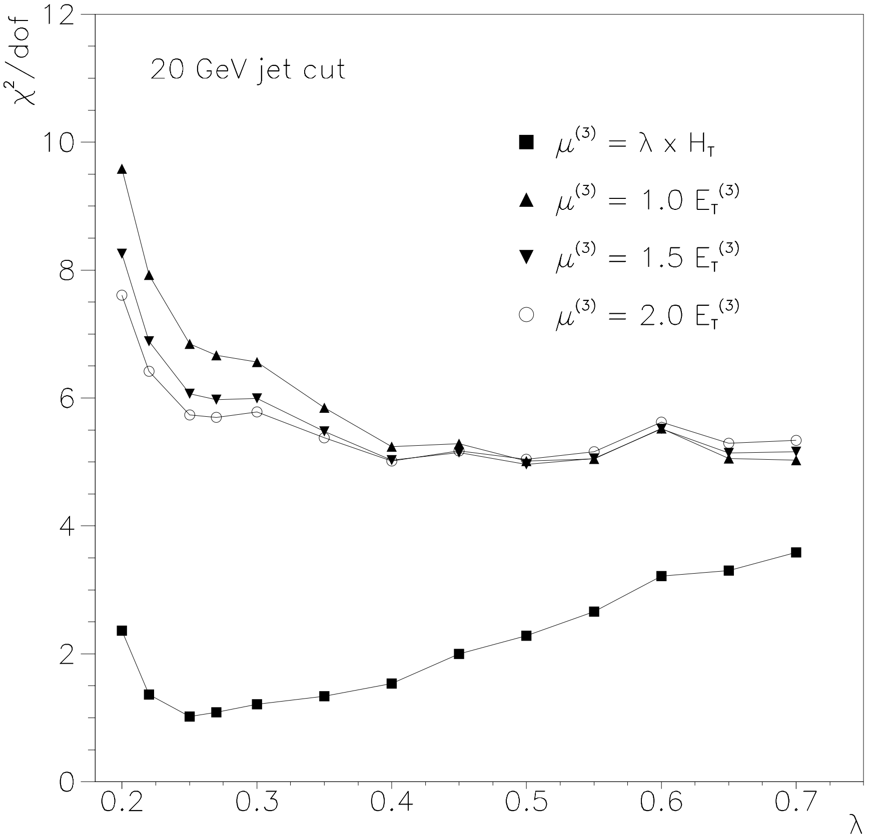

Figure 7.21: χ^2 difference between data and theory as a function of the coefficient of the hard scale.

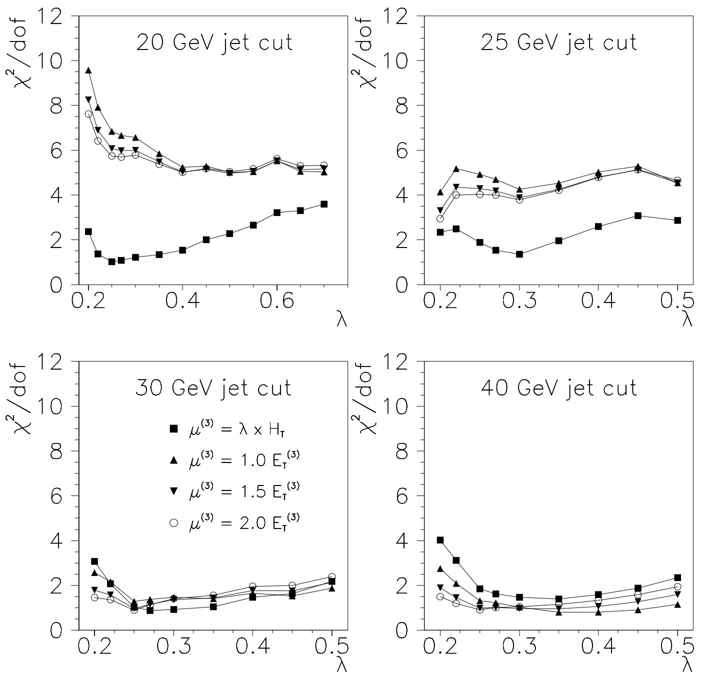

Figure 7.22: χ^2 difference between data and theory as a function of the coefficient of the hard scale (λ), for jet E_T thresholds of 20 (a), 25 (b), 30 (c), and 40 GeV (d).

the agreement between data and theory, and all $\mu_R^{(3)} \approx E_T^{(3)}$ scales are an unlikely fit to the data.

Jet threshold

In the previous section, a jet E_T threshold of 20 GeV was used in the data and theory. We have studied how the results depend on this minimum jet E_T threshold. We reanalyze the data using minimum jet E_T s of 25, 30, and 40 GeV and repeat the χ^2 comparisons with theory.

Figure 7.22 shows the $\tilde{\chi}^2$ vs λ plot for jet E_T thresholds of 20, 25, 30, and 40 GeV. At a jet E_T threshold of 25 GeV, the $\mu_R^{(3)} \approx E_T^{(3)}$ curves improve their agreement with data, with the greatest change occurring at $\lambda < 0.4$. The $\mu_R^{(3)} \approx H_T$ theory still give better agreement with the data, with perhaps a shift in the λ value for the minimum $\tilde{\chi}^2$. As we increase the threshold to 30 GeV, the four curves remain close together and their $\tilde{\chi}^2$ decrease to about 1 for all values of λ. There is no preferred scale in this comparison. The result is the same when we require all jets to have an E_T above 40 GeV. The $\tilde{\chi}^2$ vs λ curves all converge to about 1 for most values of λ. The greatest sensitivity in distinguishing between a $\mu_R^{(3)} \approx H_T$ theory and a $\mu_R^{(3)} \approx E_T^{(3)}$ theory is then found when using a jet E_T threshold of 20 GeV or at most 25 GeV.

7.4.2 Restricted range of jet pseudorapidity

We investigated the applicability of the previous findings as we restrict the pseudorapidity of the jets to 2.0 instead of 3.5 as before. We are interested in how our finding change when we explore a narrower region of the η phase space. We repeat this using only 20 GeV as our jet E_T threshold since this is the E_T threshold where we are most sensitive. Figure 7.23 shows the change in $\tilde{\chi}^2$ as a function of λ. Agreement is poor for all $\mu_R^{(3)} \approx E_T^{(3)}$, with weaker dependence on λ. For $\mu_R^{(3)} \approx H_T$, the agreement between data and theory is very good, with a minimum $\tilde{\chi}^2$ at $\lambda = 0.35$. As with the full $\eta < 3.5$ case, the $\mu_R^{(3)} \approx H_T$ theory is a better fit to the data.

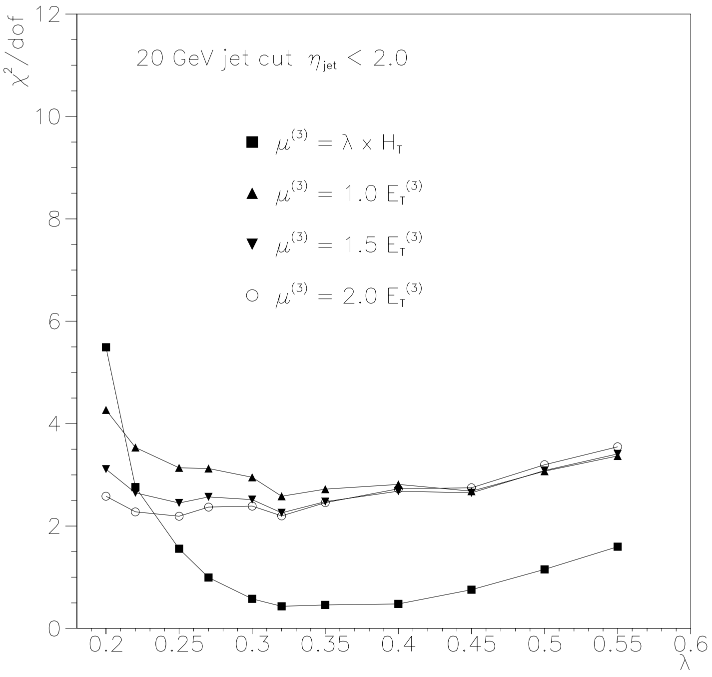

Figure 7.23: χ^2 difference between data and theory, vs the hard scale, $\eta < 2.0$

Chapter 8

Conclusion

We measured the cross section ratio $\frac{\sigma_{3+}}{\sigma_{2+}}$ as a function of the summed transverse energies of all jets in an event. The analysis was based on single-jet inclusive triggers. The uncertainties in the result were due to the jet energy scale, background from multiple-interaction, and general event and jet selection criteria. Our measurement provides an estimate of the rate of soft jet production at different parton-parton center-of-mass energies. We find that, above 200 GeV in H_T , the probability for emitting a third jet is around 70%. This result will help in the design of triggers for detecting the Higgs particle at the Large Hadron Collider, especially in high-luminosity environments.

Our measurement is compared to theoretical predictions from a Next-to-Leading Order QCD Monte Carlo event generator (JETRAD). Uncertainties in the theoretical predictions are mainly due to the flexibility in the parameters used for jet reconstruction. Comparisons of data to theory lead to the conclusion that

1. The ratio $\frac{\sigma_{3+}}{\sigma_{2+}}$ is in good agreement with perturbative QCD predictions for multijet production above an E_T threshold of 30 GeV.

2. The renormalization scale for the creation of soft jets is better modeled using a scale of the order of the hard-scattering scale (H_T) rather than the transverse energy of the third jet.

3. This finding also holds when we restrict the pseudorapidity of jets from $|\eta| < 3.5$ to $|\eta| < 2.0$

4. As we increase the jet E_T threshold, the discrimination between the scales $\mu_R^{(3)} \approx H_T$ and $\mu_R^{(3)} \approx E_T^{(3)}$ is decreased, notably for $E_T^{\min} > 30$ GeV.

The model that best describes the data is one that uses only a single scale for both the hard scatter and for the emission of soft jets. This simplifies theoretical calculations since the additional scale does not improve the prediction. Although the single scale, in particular a value of about $0.25 H_T$, has been shown to hold for only this process (three-jet events), the present technique can be tested on other topologies.

Calculations of the matrix elements for purely gluonic three-jet processes at Next-to-Leading Order ($\mathcal{O}(\alpha_S^3)$) are already available. When the full NLO calculations are completed, a measurement of α_S can be extracted from the measured ratio $\frac{\sigma_{3+}}{\sigma_{2+}}$ of cross sections.

Bibliography

[1] H. Frauenfelder and E. M. Henley, Subatomic Physics, New Jersey: Prentice-Hall, 1974, p. 323.

[2] D. Griffiths, *Introduction to Elementary Particles*, New York: John Wiley & Sons, 1987, p. 33.

[3] G. Sterman *et al.*, Rev. Mod. Phys. 67, 157 (1995).

[4] F. Halzen and A.D. Martin, *Quarks and Leptons: An Introductory Course in Modern Physics*, New York, John Wiley & Sons, 1984, p. 326.

[5] B. Abbott *et al.* (DØ Collaboration), *Direct Measurement of the Top Quark Mass at D0*, FERMILAB-PUB-98/031-E, hep-ex/9801025.

[6] D. Soper, e-Print Archive hep-ph/9702203.

[7] F. Halzen and A.D. Martin, *Quarks and Leptons: An Introductory Course in Modern Physics*, New York, John Wiley & Sons, 1984, p. 171.

[8] D. Soper, e-Print Archive hep-lat/9609018.

[9] A.D. Martin, R.G. Roberts, W.J. Stirling, *MRS Parton Distributions*, RAL-93-077, DTP/93/86 (1993).

[10] M. Gluck, E. Reya, A. Vogt, Z.Phys.**C67**:433-448,1995.

[11] H.L. Lai *et al.*, Phys.Rev. **D51** (1995) 4763, hep-ph/9410404.

[12] R.K. Ellis, W.J. Stirling, and B.R. Webber, *QCD and Collider Physics*, Cambridge: Cambridge University Press, 1996, p. 108.

[13] J.F. Owens, "Applications of QCD to Hard Hadronic Processes" in *Quantum Chromodynamics: Theory and Experiment, Proceedings of the Third Lake Louise Winter Institute: Chateau Lake Louise, Canada, 6-12 March 1988*, B.A. Campbell *et al.*, ed, Singapore: World Scientific, 1988.

[14] F. Halzen and A.D. Martin, *Quarks and Leptons: An Introductory Course in Modern Physics*, New York, John Wiley & Sons, 1984, p. 213.

[15] R.K. Ellis, W.J. Stirling, and B.R. Webber, *QCD and Collider Physics*, Cambridge: Cambridge University Press, 1996, p. 247.

[16] R.K. Ellis, W.J. Stirling, and B.R. Webber, *QCD and Collider Physics*, Cambridge: Cambridge University Press, 1996, p. 256.

[17] R.K. Ellis, W.J. Stirling, and B.R. Webber, *QCD and Collider Physics*, Cambridge: Cambridge University Press, 1996, p. 185.

[18] D. Zeppenfeld, "Gluon Radiation Patterns in Hard Scattering Events," University of DØ lecture, April 3, 1997 (Unpublished).

[19] D. Rainwater, D. Summers, D. Zeppenfeld, Phys.Rev. **D55**(1997) 5681, hep-ph/9612320.

[20] D. Summers, D. Zeppenfeld, Phys.Lett.**B380** (1996) 426, hep-ph/9509206.

[21] J. Thompson, *Introduction to Colliding Beams at Fermilab*, FERMILAB-TM-1909 (1994).

[22] DØ Collaboration, Nucl. Inst. and Meth. **A338**, 185 (1994).

[23] M.F. Paterno, *A Search for Squarks and Gluinos in $p\overline{p}$ Collisions at $\sqrt{s} = 1.8$ TeV with the DØ Detector*, Ph.D. Thesis, State University of New York at Stony Brook, May 1994 (Unpublished).

[24] J. Huth *et al.*, *Research directions for the decade,* Proceedings of the 1990 DPF summer study on High Energy Physics, Snowmass, Colorado, World Scientific (1990).

[25] B. Abbott *et al.*, "Fixed Cone Jet Definitions in DØ and R_{sep}", DØ Internal Note # 2885, March 21, 1996 (Unpublished).

[26] *PAW: Physics Analysis Workstation, The Complete Reference*, CERN Program Library Long Writeup **Q121** (1993).

[27] M. Bhattacharjee *et al.*, "Efficiencies of the Standard Jet Cuts For Cone Sizes: 0.3, 0.5, 0.7", DØ Internal Note # 2197, July 15, 1994 (Unpublished).

[28] V. D. Elvira *et al.*, "A Study of Standard Jet Cuts and their Efficiencies Using DØ Collider Data", DØ Internal Note # 1763, June 21, 1993 (Unpublished).

[29] T. Geld, "Trigger Efficiencies for Run 1a Inclusive Jet Triggers", DØ Internal Note # 2474, February 9, 1995 (Unpublished).

[30] R. Astur, A. Milder, "Jet Trigger Efficiency in the DØ Detector, DØ Internal Note # 1663, March 8, 1993 (Unpublished).

[31] I.G. Knowles *et al.*, e-Print Archive hep-ph/9601212.

[32] G. Marchesini *et al.*, Comp. Phys. Comm. **67** (1992) 465.

[33] T. Fahland, "Vertex Finding in Level 2: Description of L2_Vert function and studies of comparisons and resolution for L2 CDC vertex finding and Level0", DØ Internal Note # 2028, January 27, 1994 (Unpublished).

[34] Previous versions of the jet energy scale (V5.0) did not use a luminosity-dependent correction and the dependence of $\frac{\sigma_{3+}}{\sigma_{2+}}$ on luminosity was larger than with the current (V5.1) version of the energy scale.

[35] B. Abbott *et al.*, "Jet Energy Scale at DØ", DØ Internal Note # 3287, Aug. 28, 1997 (Unpublished).

[36] A. Kotwal, "Effects of Multiple Interactions and Pileup on the W Mass Measurement in the Electron Channel at DØ in Run II and TeV33" , DØ Internal Note # 3226, May 31, 1997 (Unpublished).

[37] R. Wigmans, "High Resolution Hadron Calorimetry," in *Experimental Techniques in High Energy Nuclear and Particle Physics* 2nd Ed., T. Ferbel, ed., Singapore: World Scientific, 1991.

[38] W.T. Giele, E.W.N. Glover, David A. Kosower, Nucl. Phys. **B403**:633-670, 1993, hep-ph/9302225.

[39] D. Summers, *private e-mail communication.*

[40] D. Zeppenfeld, e-Print Archive hep-ph/9603315, MADPH-95-9330.

[41] G. Peter Lepage, J. Comput. Phys. **27**, 192 (1978).

[42] M. Bhattacharjee *et al.*, "Jet Energy Resolutions", DØ Internal Note # 2557, July 6, 1995 (Unpublished).

[43] M. Bhattacharjee *et al.*, "Jet Energy Resolutions", DØ Internal Note # 2887, May 22, 1996 (Unpublished).

[44] B. Hirosky, "A Data-based Estimate of Jet Reconstruction Efficiencies", DØ Internal Note # 2369, Nov 1, 1994 (Unpublished).

[45] B. Hirosky and Z. Casilum "Jet Reconstruction Efficiencies", DØ Internal Note # 3324, in preparation (Unpublished).

[46] W. Giele, *private communication.*

Appendix A

Matrix Elements for 2-to-3 Parton Scattering

In Chapter 2 I listed the matrix elements for 2-to-2 scattering and also one of the formulas for 2-to-2 scattering. Here I list the remainder of the formulas. The four general kinds of processes are:

$$\begin{array}{lrcl}
(A) & q(p_1) + q'(p_2) & \rightarrow & q(p_3) + q'(p_4) + g(k) \\
(B) & q(p_1) + q(p_2) & \rightarrow & q(p_3) + q(p_4) + g(k) \\
(C) & q(p_1) + \overline{q}(p_2) & \rightarrow & g(p_3) + g(p_4) + g(p_5) \\
(D) & g(p_1) + g(p_2) & \rightarrow & g(p_3) + g(p_4) + g(p_5)
\end{array}$$

The matrix element for process A is given in Chapter 2. For process B, the equation is

$$\begin{aligned}
\overline{\sum} \left| \mathcal{M}^{(B)} \right|^2 &= \frac{4g^6}{9} \left[\left(\frac{s^2 + s'^2 + u^2 + u'^2}{2tt'} \right) \left(\frac{8}{3} \left([14] + [23] \right) + \frac{1}{3} [12;34] \right) \right. \\
&+ \left(\frac{s^2 + s'^2 + u^2 + u'^2}{2uu'} \right) \left(\frac{8}{3} \left([13] + [24] \right) + \frac{1}{3} [12;34] \right) \\
&- \left. \frac{2}{3} \frac{(s^2 + s'^2)(ss' - tt' - uu')}{4tt'uu'} \left(\frac{8}{3} \left([12] + [34] \right) + \frac{1}{3} [12;34] \right) \right]
\end{aligned}$$

For Processes C and D we introduce the notation

$$\{ij\} \equiv p_i\dot{p}_j$$

The matrix element for process C is

$$\begin{aligned}
\overline{\sum}\left|\mathcal{M}^{(C)}\right|^2 &= \frac{2g^6}{81}\sum_{i=1}^{3}\frac{\{1i\}\{2i\}(\{1i\}^2+\{2i\}^2)}{\{13\}\{14\}\{15\}\{23\}\{24\}\{25\}} \\
&\times \left[10\{12\} - 9\sum_P \frac{\{13\}\{24\}+\{14\}\{23\}}{\{34\}}\right. \\
&+ \left.\frac{81}{\{12\}}\sum_P \frac{\{15\}\{25\}(\{13\}\{24\}+\{14\}\{23\})}{\{45\}\{53\}}\right]
\end{aligned}$$

The sums over P are over cyclic permutations of the momentum labels (3,4,5) of the final state gluons. And finally, for process D we have

$$\begin{aligned}
\overline{\sum}\left|\mathcal{M}^{(D)}\right|^2 &= \frac{9g^6}{640}\left[\sum_P \{12\}^4\right]\left[\sum_P \{12\}\{23\}\{34\}\{45\}\{51\}\right] \\
&\times \left(\prod_{i<j}\{ij\}\right)^{-1}
\end{aligned}$$

where the sums are over the permutations of the five gluon labels.

Appendix B

Calculation of χ^2 Using a Covariance Matrix

Here we give an example of calculating χ^2 using a covariance matrix. This method was used in Chapter 7 to compare data to Monte Carlo theoretical predictions. For simplicity we have three data points compared to three theory points. Figure B.1 shows the data points and theory curve. The error bars shown on the data points are the statistical (inner) and systematic error (outer). The data and theory numbers with errors are given in Table B. The error matrix for the data errors is constructed as follows: The uncorrelated data statistical errors $(0.16, 0.18, 0.21)$ are squared and form the diagonal

Table B.1: Data for sample χ^2 calculation.

X-value	Data			Theory	
	Value (D)	Stat. error σ_{stat} (uncorrelated)	Syst. error σ_{syst} (correlated)	Value (T)	Error (uncorrelated)
1	5.20	0.16	0.26	5.00	0.10
2	5.90	0.18	0.30	6.00	0.12
2	7.10	0.21	0.35	7.00	0.14

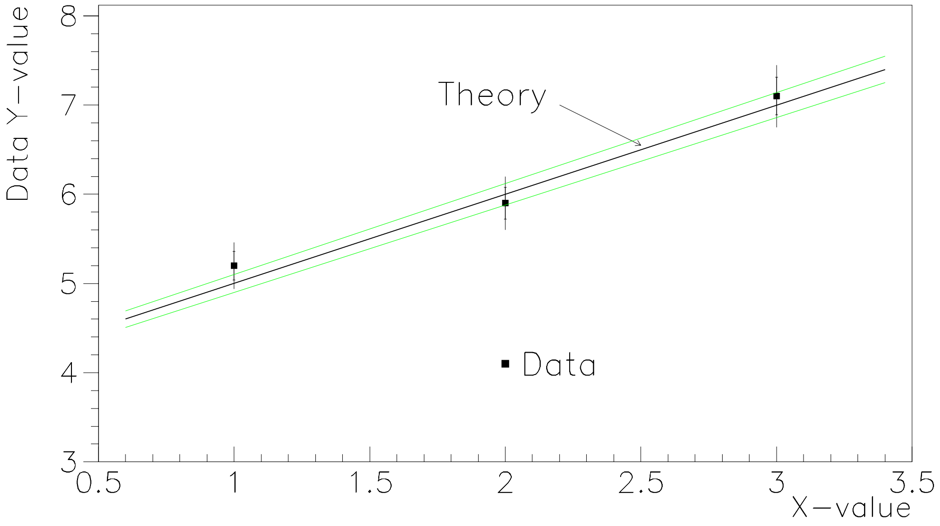

Figure B.1: Sample data and theory values to describe the covariance matrix χ^2 calculation. The gray lines above and below the theory line represent the error on the theory.

elements of the error matrix $E^{\text{data}}_{\text{uncorr}}$:

$$E^{\text{data}}_{\text{uncorr}} = \begin{pmatrix} \sigma^2_{\text{stat},1} & 0 & 0 \\ 0 & \sigma^2_{\text{stat},2} & 0 \\ 0 & 0 & \sigma^2_{\text{stat},3} \end{pmatrix} = \begin{pmatrix} 0.025 & 0 & 0 \\ 0 & 0.031 & 0 \\ 0 & 0 & 0.045 \end{pmatrix}$$

The correlated data systematic errors are put into a matrix which includes correlations from one data point to another:

$$E^{\text{data}}_{\text{corr}} = \begin{pmatrix} \sigma^2_{\text{syst},1} & \sigma_{\text{syst},1}\sigma_{\text{syst},2} & \sigma_{\text{syst},1}\sigma_{\text{syst},3} \\ \sigma_{\text{syst},2}\sigma_{\text{syst},1} & \sigma^2_{\text{syst},2} & \sigma_{\text{syst},2}\sigma_{\text{syst},3} \\ \sigma_{\text{syst},3}\sigma_{\text{syst},1} & \sigma_{\text{syst},3}\sigma_{\text{syst},2} & \sigma^2_{\text{syst},3} \end{pmatrix} = \begin{pmatrix} 0.068 & 0.078 & 0.901 \\ 0.078 & 0.090 & 0.105 \\ 0.091 & 0.105 & 0.123 \end{pmatrix}$$

The uncorrelated theory error is also diagonal:

$$E^{\text{theory}}_{\text{uncorr}} \begin{pmatrix} 0.010 & 0 & 0 \\ 0 & 0.014 & 0 \\ 0 & 0 & 0.020 \end{pmatrix}$$

The sum of all three matrices is the covariance matrix C:

$$C = E^{\text{data}}_{\text{uncorr}} + E^{\text{data}}_{\text{corr}} + E^{\text{theory}}_{\text{uncorr}} = \begin{pmatrix} 0.103 & 0.078 & 0.091 \\ 0.078 & 0.137 & 0.105 \\ 0.091 & 0.105 & 0.186 \end{pmatrix}$$

The formula for the χ^2 between the data and theory is

$$\chi^2 = \sum_{i\ j}^{3} (D_i - T_i) \frac{1}{C_{ij}} (D_j - T_j)$$

To calculate the term in the sum we need the inverse of C:

$$C^{-1} = \begin{pmatrix} 20.18 & -6.94 & -5.95 \\ -6.94 & 15.28 & -5.22 \\ -5.95 & -5.22 & 11.22 \end{pmatrix}$$

The (row=1,column=2) term is

$$\begin{aligned} \text{term}_{1,2} &= (D_1 - T_1) \times C^{-1}_{12} \times (D_2 - T_2) \\ &= (5.20 - 5.00) \times -6.94 \times (5.9 - 6) \\ &= 0.139 \end{aligned}$$

This is repeated for all other terms in the 3 × 3 matrix. The number of calculations can be reduced to almost half by using the fact that the inverse covariance matrix is symmetric about the diagonal. The sum of all nine terms in this example is 1.216, so the reduced χ^2 is $1.216/3 = 0.41$. The size of the covariance matrix is equal to the number of data points in the Data-Theory comparison. For the comparison of the cross section ratio to theory the covariance matrix is 28×28.